PUBLICATION NO. U-4038

SAN-595-4

FINAL REPORT

ALKALI METAL TWO-PHASE FLOW INVESTIGATION

Prepared Under
Contract AT(04-3)-595
for the
Engineering Development Branch
Division of Reactor Development
and Technology
U.S. Atomic Energy Commission

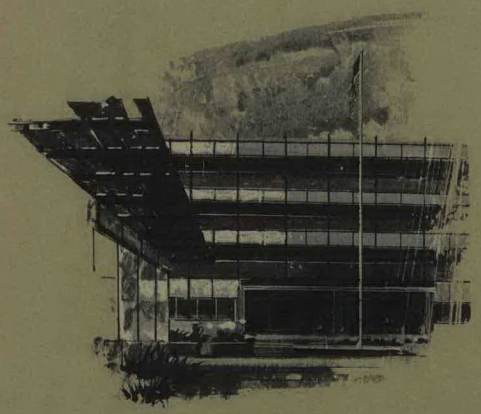

PHILCO Ford
PHILCO-FORD CORPORATION
Aeronutronic Division
Newport Beach, California

DISCLAIMER

Publication No. U-4038
SAN-595-4

Final Report

ALKALI METAL TWO-PHASE FLOW INVESTIGATION

May 17, 1967

by

Hans D. Linhardt

Aeronutronic Division

Philco-Ford Corporation

Prepared Under
Contract AT(04-3)-595
for the
Engineering Development Branch
Division of Reactor Development
and Technology
U.S. Atomic Energy Commission

PHILCO-FORD CORPORATION
Aeronutronic Division
Newport Beach, California

PROPRIETARY NOTICE

FOREWORD

This report was prepared by Aeronutronic Division of Philco-Ford Corporation under Contract AT(04-3)-595. Mr. Nicholas Grossman, Engineering Development Branch Chief, Division of Reactor Development, U. S. Atomic Energy Commission administered the program. The author served as project manager under the program direction of Mr. G. P. Carver and is indebted to Messrs. N. Grossman and F. Hunton, the latter from the AEC San Francisco office, for the continuous encouragement and assistance in carrying the present program to its successful completion. In addition, the contribution and support of the following workers in the field is appreciated: Dr. G. Gyarmathy, ARL, for many fruitful discussions on turbine condensation phenomena; Dr. A. P. Fraas and Mr. L. Fuller, ORNL, for the valuable assistance and suggestions during the construction phase of Aeronutronic's liquid metal loop; Mr. A. Glassman, NASA Lewis Laboratory, for valuable discussions dealing with liquid metal condensation, and in particular Dr. F. E. Marble, Professor of Jet Propulsion and Mechanical Engineering at the California Institute of Technology and consultant to Aeronutronic, who first suggested the nozzle-wedge technique, and provided continuous assistance in solving many of the two-phase flow problems associated with the present program.

The valuable support and contributions of the following and Aeronutronic personnel are acknowledged: Mr. F. R. Cheslak and Mr. R. F. Smisek for assistance in the analysis effort and proof reading of the manuscript, Mr. G. Baenteli and his technicians Mr. D. Doak and Mr. N. Black for the excellent performance of the test program, and Mr. N. Bellino for the design of the test equipment.

ABSTRACT

This report summarizes the final results of the potassium turbine erosion investigation performed under Contract AT(04-3)-595. The program consisted of three tasks: Task I, droplet size determination, Task II, potassium turbine erosion test, and Task III, potassium turbine two-phase flow analysis.

Under Task I the potassium condensate droplet sizes were experimentally determined for typical thermodynamic expansion processes in the $1000^{\circ}F < T < 1500^{\circ}F$ temperature range and theoretical quality condition $0.80 < X < 0.95$. For this purpose, a forced convection, boiling-condensing, closed loop potassium facility was developed. The potassium loop provided the specified potassium vapor conditions to the test section which consisted of various expansion nozzles and nickel plated wedge specimens placed downstream of the nozzle. After performance of seven (four to five hours) short duration tests, the wedge erosion damage lengths were measured and correlated with two-phase flow theory.

The analysis of the test data provided internally consistent, accurate, and reproducible information on free stream droplet sizes. The significant result of Task I is that the measured average free stream droplet size is an order of magnitude larger than the average droplet size predicted by present condensation theories. In addition, the exploratory program has proven that the selected nozzle-wedge erosion method works and, therefore, should be utilized for future more detailed two phase flow investigations.

Under Task II a supersonic potassium turbine was designed, fabricated and tested within the closed loop potassium test facility. The test turbine, which was made of TZM molybdenum material with four different blade geometries, was run for 96 hours at an average shaft speed of 17,800 rpm, the average turbine stagnation condition was $1250^{\circ}F$ and 5.6 psig and theoretical nozzle exit vapor quality of $x = 0.85$.

The most prominent feature evident on inspection of the turbine wheel was an erosion groove starting at the leading edge near the root of each blade

and then continuing in a radial direction to the blade tip immediately behind the leading edge on the convex side of the blade. In addition, two of the three partial admission turbine nozzles experienced a large amount of what appeared to be corrosion with large deposits visible on the nozzle walls. Due to flow separation, it is believed that a puddle of liquid potassium accumulated downstream of the corroded nozzle area, from which large liquid potassium droplets were shed. The impingement of these secondary droplets upon the turbine wheel would explain the erosion groove on each blade. The small amount of erosion visible on the concave and convex side of the blades near the leading edge is attributed to the impingement of primary or free stream potassium droplets.

In case the nozzle corrosion could have been avoided, there should not have been any significant blade damage due to the micron size of the primary droplets and the absence of secondary or large droplets as indicated by the Task I analysis. It is recommended to eliminate the corrosion by redesign of the nozzles and a more stringent control of the oxygen level during loop operation.

The objective of Task III was to derive an engineering estimate of the limiting tip speed of supersonic potassium turbines operating within the temperature range from 1000° to 1500°F and with nozzle vapor exhaust qualities ranging from 80 to 95 percent. For this purpose, the experimental results of Task I and Task II have been considered in conjunction with a novel theoretical treatment of the wet vapor dynamics. The latter treatment includes analysis of the gas dynamic shock zone, the relaxation zone, and the velocity and thermal equilibration zone. In addition, the processes of fluid collection on blades and droplet shedding from liquid layers formed on stationary blades have been explored analytically prior to the discussion of the wet vapor turbine performance trends.

The experimental and theoretical results indicate that a properly designed supersonic single-stage potassium turbine should not have a vapor quality type of tip-speed limit for the quality range of interest. However, further experimental work is required to substantiate the analysis and, subsequently, to provide a solution for a two-stage supersonic, erosion-free, potassium turbine design.

CONTENTS

CONTENTS (Continued)

ILLUSTRATIONS

ILLUSTRATIONS (Continued)

ILLUSTRATIONS (Continued)

TABLES

SECTION 1

INTRODUCTION

The development of liquid metal, Rankine cycle nuclear power systems depends upon detailed understanding of the engineering problems that affect the choice of working medium, temperature level, etc., for the cycle. One of these problems is the fluid mechanics of wet liquid metal vapors and, in particular, turbine erosion due to impingement of droplets. It is interesting to note that, although this information is available in empirical form for steam, the phenomena are insufficiently understood to permit application of these results to media other than steam. Because the time and expense for accumulating extensive empirical information on each of the liquid metal vapors are prohibitive, it is necessary to gain the fundamental understanding of the physical mechanisms involved so that results from any liquid metal experiment may be interpreted in terms of other liquid metals. The liquid droplet impingement on turbine blades and subsequent erosion is one of these basic problems.

Depending upon such basic parameters as droplet size, orientation and absolute value of the impingement vector with respect to the turbine blading, thermodynamic cycle state point conditions, impingement and condensation rate, and the turbine materials, applicable turbine performance losses or progressive blade erosion due to droplet impingement might limit the application of the liquid metal dynamic power plant. The present exploratory program is directed toward identification and better engineering understanding of the interaction of the erosion parameters.

The analysis of alkali metal turbine erosion limits is very difficult because it requires detailed knowledge of the two phase flow field throughout the multistage turbine. For this purpose, basic two phase flow parameters, such as free stream droplet sizes as a function of thermodynamic state points must be determined for subsonic and supersonic turbine conditions. For the latter case, the possibility of droplet growth or dispersion due to interaction with weak and strong shock waves must be investigated. In addition, the mechanism of trailing edge droplet shedding and its resulting droplet sizes must be determined for stator and rotor blade annular cascades. This information is not available for potassium and requires even further experimental verification for steam. For example, an excellent summary of the condensation and two phase flow theory as applied to steam turbines has been presented by Gyarmathy[1]; however, the verification and extension of

this work depends upon detailed experiments. Considering also informative efforts to correlate observed steam turbine erosion processes with theory by assuming various condensate droplet sizes,[2] it becomes clear that one of the first tasks of any program of this sort should be the experimental determination of the order of magnitude of the free stream droplet sizes. For this purpose, various thermodynamic expansion processes and nozzle configurations must be examined experimentally.

It is tempting to ask whether one might achieve the necessary understanding through careful analysis of experiments in wet steam. However, the physical properties of liquid metals and water (e.g., thermal conductivity, electrical properties, etc.) differ so markedly that it is highly improbable that their behaviors are at all similar. Consequently, any conclusions derived from experiments in steam would require extensive verification with liquid metals. On the other hand, work with potassium has direct empirical value for the alkali metals even if the search for the understanding of physical phenomena falls short of its mark. While the work of Reference (3) falls in the steam category, the potassium turbine test program of Reference (4) is limited to one particular reaction turbine configuration. To provide more general design information, the present exploratory program attempts to measure the free stream droplet size as a function of significant power cycle parameters. For this purpose, Aeronutronic has conceived the unique supersonic nozzle-wedge damage length method. This method is derived from the fact that when a two-dimensional wedge is placed downstream of a supersonic nozzle, the vapor stream will experience an oblique shock and then turn parallel to the wedge surface while the free stream condensate droplets pass straight through the shock wave zones and, depending on droplet size and interaction with gas flow, may or may not impinge on the wedge. If the wedge surface is plated with an appropriate material, the free stream droplet size can be deduced from the damage resulting from droplet impingement on the wedge.

In Sections 2, 3 and 4, a review is presented of an extensive theoretical investigation directed toward examination of the two-phase flow problem in general and the relaxation processes in particular. The results are also directly applicable to the interpretation of wedge erosion experiments and blade impact phenomena. The test facility is described in Section 5 while Section 6.1 provides the theoretical background justifying the damage length technique and Section 6.2 explains the selection of the test configurations and thermodynamic processes. Sections 6.3 and 6.4 provide an outline of this portion of the test program and present the analysis of the test results.

In Section 7 of the report, the program and results of the Potassium Turbine Investigation are described in detail. Section 7.1 and 7.2 provide the theoretical foundations for the collection of liquid potassium on blades and the nature of droplets shed from the trailing edges of

stationary and rotating blades. Section 7.3 describes the test program, test turbine, and test operations. Section 7.4 describes the test results on the turbine blades and nozzles and Section 7.5 related these results to analytical considerations and adds some qualitative observations. The results are summarized and organized in Section 8 and recommendations based upon these results are presented.

SECTION 2

GENERAL ASPECTS OF WET VAPOR DYNAMICS

The fluid dynamics of wet vapors contain elements of principle and detail that differentiate its study from that of an ideal gas. The consequences of the unusual equations of state are perhaps of less interest than the nonequilibrium and relaxation processes that arise from the two-phase character of the flow and the phase transition. Under easily attainable circumstances, the equilibration or relaxation processes associated with exchange of mass, momentum, and energy between phases will dominate a flow field, and consequently merit understanding. The importance of relaxation processes cannot be overemphasized in the flow of wet vapors through high-speed turbine stages.

The structure of the normal shock is not only important in its own right, but it is a convenient vehicle for isolating a wide variety of relaxation processes to permit their investigation. Over the last few years, Carrier,[5] Marble,[6] and Rudinger[7] are among those who have used this means to examine the equilibration processes in mixtures of perfect gas and inert solid particles. More recently, there has been interest in vaporization of liquid fuel droplets[8] and the ablation of plastic solids behind shocks. Although the present work, restricted to the phases of a pure substance, is related in principle to these problems, the physics differ in an essential way. Molecular diffusion may control the rate of phase change in a mixture of vapor and inert gas; it is not the rate-controlling step for the pure substance. It is the fluid dynamics of wet vapors of a pure substance that is of interest in vapor power cycles. The flow of a wet vapor in mechanical and thermodynamic equilibrium[9] and the mechanism of nucleation and condensation in supersaturated vapors[10] present their own peculiar difficulties. By a wet vapor, it is implied that the vapor exists in intimate conjunction with droplets of the condensed phase and, consequently, the problem of nucleation need not arise. In fact, it will be assumed that the existing liquid droplets retain their identity during the flow process.

The structure of the normal shock may be divided into three zones, each dominated by different physical processes and, in most cases, each being geometrically distinct from the others.

The first of these zones is designated the "gasdynamic shock" and takes place in the vapor phase without change in phase or in the mechanical or thermodynamic state of the liquid. Even for a very wet vapor, one consisting of equal weight fractions of liquid and vapor, the gasdynamic shock is "perforated" by droplets over less than 10^{-3} of its area and, consequently, may be considered independent of the liquid phase.

If it is assumed that the two phases are in equilibrium far upstream and that the change of liquid state is negligible across the gasdynamic shock, then the two phases are not in equilibrium behind the gasdynamic shock. The pressure of the vapor has increased to a value in excess of that corresponding to the droplet temperature. This condition of thermodynamic nonequilibrium is adjusted in a pure substance by the condensation of molecules of the vapor upon the droplet surface at a rate greatly in excess of the vaporization of molecules from the liquid droplet. The characteristic rate with which this exchange proceeds is of the order of the sonic velocity in the vapor phase, and one may think of the vapor "collapsing" upon the liquid at this rate. The process continues until the enthalpy, including latent heat, carried by the condensing vapor raises the droplet to the saturation temperature corresponding to the existing pressure of the vapor. It is interesting to note that, in spite of the fact that the liquid droplets will eventually disappear or be greatly decreased in size, their first change is to increase in size in response to the increase in pressure of the vapor across the gasdynamic shock. This increase in particle mass may reach a value of 20 percent of the original mass. The order of magnitude of the thickness of this "vapor relaxation" zone may be estimated by noting that if the droplet of radius σ doubled its mass, the condensate would originate in a layer of thickness $\sigma(\rho_\ell/\rho)^{1/3}$, where ρ and ρ_ℓ are the mass density of the vapor and the liquid, respectively. If this vapor sphere collapses at roughly the sound speed, the liquid droplets will travel a distance $\sim M_o(\rho_\ell/\rho)^{1/3}\sigma$ during this process. Since $M_o > 1$, $\rho_\ell/\rho \sim 10^3$, and σ are generally greatly in excess of the mean free path in the vapor phase, the thickness of the vapor relaxation zone exceeds the thickness of the gasdynamic shock by a factor of 10^2. Therefore, it is reasonable to treat them as distince processes in the analysis.

In spite of the fact that the pressure of the vapor and the temperature of the droplets correspond to the thermodynamic saturation state, the vapor temperature and velocity do not correspond to the droplet temperature and velocity. The third and final zone of the shock structure, therefore, consists of a relatively slow exchange of mass, momentum, and energy between phases at a rate corresponding to the characteristic diffusion time σ^2/ν, where ν is the kinematic viscosity of the vapor phase. The distance, λ_V, required to dissipate the momentum of the droplet traveling at the initial

Mach number, M_o, is of the order $M_o(\rho_\ell/\rho)\,\sigma \cdot \sigma/\ell$, where ℓ is the mean free path in the vapor phase. This is at least $(\rho_\ell/\rho)^{2/3}$ as large as the vapor relaxation zone and, hence, exceeds all other dimensions of the shock thickness by a factor greater than 10^2. This large and distinct region constitutes the velocity and thermal equilibration zone. Its structure has been discussed previously (e.g., Reference 5) for inert particles.

SECTION 3

STATE CHANGES ACROSS DISCRETE STRUCTURAL ZONES

Because the gasdynamic shock, vapor relaxation, and thermal and velocity equilibration zones within the shock wave possess thicknesses of different orders of magnitude, it is possible to calculate gross changes across each of them in the same sense that one calculates gross changes across a conventional shock wave. This provides a crude but useful determination of the shock structure and a guide to subsequent detailed analysis of the thermal and velocity relaxation zone. For each zone, gross conservation relations may be written which include the constraints appropriate to the changes that are permitted across each zone. For example, across the gasdynamic shock, no change in droplet state is permitted by definition; across the vapor relaxation zone, no diffusive transfer of heat or momentum between phases is allowed. These constrained conservation relations will be discussed in detail as they arise. Consider the shock to be subdivided into the regions 0 to 1, the gasdynamic shock; 1 to 2, the vapor relaxation zone; and 2 to 3, the thermal and velocity relaxation zone, as indicated in Figure 3-1.

3.1 GASDYNAMIC SHOCK

The region of the gasdynamic shock is characterized by transport and thermodynamic processes within the vapor phase and no change in the state of the droplets. The mechanical and thermal effects of the droplets on the vapor are negligibly slow within this region so that even the drag of the droplets may be disregarded in comparison with the internal viscous stresses within

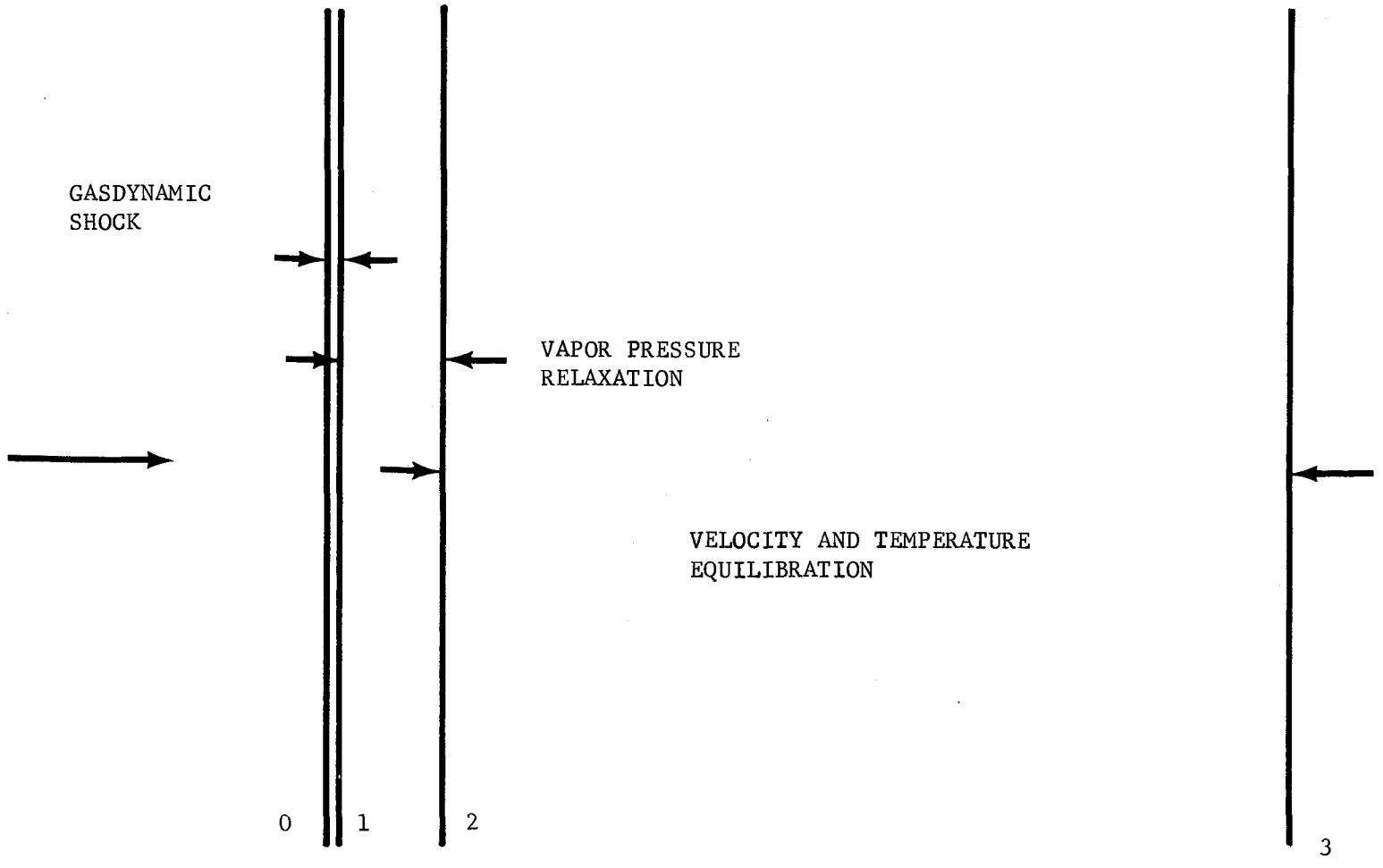

FIGURE 3-1. ZONES COMPRISING THE SHOCK STRUCTURE

the vapor. Then, the states ahead of and behind the gasdynamic shock are related through the familiar conservation relations for a perfect gas

$$\rho_o u_o = \rho_1 u_1 \tag{1}$$

$$\rho_o u_o^2 + p_o = \rho_1 u_1^2 + p_1 \tag{2}$$

$$h_o + \frac{1}{2} u_o^2 = h_1 + \frac{1}{2} u_1^2 \tag{3}$$

$$p = \rho RT; \quad h_1 - h_2 = c_p (T_1 - T_2) \tag{4}$$

and the state of the particle is unchanged across the same region

$$\rho_{po} = \rho_{p1} \tag{5}$$

$$u_{po} = u_{p1} \tag{6}$$

$$T_{po} = T_{p1} \tag{7}$$

Moreover, the droplet radius remains constant so that

$$\sigma_o = \sigma_1 \tag{8}$$

Equations (1) through (4) lead to the conventional shock relations between planes 0 and 1, and they need not be repeated here.

3.2 RELAXATION ZONE

The second region, in which the saturation relation is established at the vapor-liquid interface, is characterized by the fact that the rapid phase transition controls the momentum and energy exchange between phases and contributes the dominant terms to the momentum and energy equations for each phase. Here, both the internal viscous stresses within the vapor and the viscous interaction of droplets and vapor contribute forces that are small in comparison with the momentum carried by the condensing mass. Similarly, the heat flux associated with thermal conductivity is unimportant in comparison with the latent heat released by the condensing mass. If we denote, by $\mu_v(x)$, the local mass rate at which vapor is being produced by the droplets contained in a unit volume of space, then the equation of continuity for the vapor phase is

$$\rho_2 u_2 = \rho_1 u_1 + \int_1^2 \mu_v(x)\, dx \tag{9}$$

where Subscripts 1 and 2 denote conditions at the beginning and end, respectively, of the saturation relaxation zone. The integral extends across the entire zone and its value represents the total mass of vapor produced in this zone. We shall write

$$\int_1^2 \mu_v(x)\, dx = \rho_o\, u_o\, \phi_2 \tag{10}$$

where ϕ_2 is the mass of vapor produced in this zone, expressed as a fraction of the original vapor flow rate.

Similarly, the momentum equation for the vapor phase is

$$\rho_2\, u_2^2 + p_2 = \rho_1\, u_1^2 + p_1 + \int_1^2 \mu_v\, u\, dx \tag{11}$$

where the integral is the momentum gained by the vapor phase as a result of the production of vapor throughout the zone. Keeping in mind the fact that the actual phase transition in this zone will be from the vapor-to-liquid phase, the control surface separating phases has been drawn so that the mass leaves the vapor phase at the local vapor velocity. Likewise, it must be assumed that the mass enters the condensed phase at the same speed. This exchange is essentially Newtonian in nature and is correct (for condensation processes) within the accuracy of neglecting viscous stresses on the droplets. Now the ratio of mass transfer to viscous stresses is of the order

$$\left(\frac{a\sigma}{\nu}\right)\left(\frac{\rho_\ell}{\rho}\right)^{2/3} \cdot \phi \tag{12}$$

which greatly exceeds unity for droplets of radius 0.1 micron and ϕ of the order of a few percent. Thus, for droplets of this radius or larger and sufficiently strong shock waves, the deletion of viscous stresses on the droplets is completely satisfactory.

In the same general degree of approximation, it will be assumed that the vapor leaves the vapor system at bulk vapor state and, hence, the energy relation for the vapor phase is

$$\rho_2\, u_2 \left(h_2 + \frac{1}{2} u_2^2\right) = \rho_1\, u_1 \left(h_1 + \frac{1}{2} u_1^2\right) + \int_1^2 \mu_v \left(h + \frac{1}{2} u^2\right) dx \tag{13}$$

where h is the vapor phase enthalpy at any position within the saturation relaxation zone.

In the same manner and to the same consistent approximation, the relations expressing conservation of mass, momentum, and energy for the liquid phase may be written

$$\rho_{p2}\, u_{p2} = \rho_{p1}\, u_{p1} - \int_1^2 \mu_v \, dx \tag{14}$$

$$\rho_{p2}\, u_{p2}^2 = \rho_{p1}\, u_{p1}^2 - \int_1^2 \mu_v \, u dx \tag{15}$$

$$\rho_{p2}\, u_{p2} \left(h_{p2} + \frac{1}{2} u_{p2}^2\right) = \rho_{p1}\, u_{p1} \left(h_{p1} + \frac{1}{2} u_{p1}^2\right) - \int_1^2 \mu_v \left(h + \frac{1}{2} u^2\right) dx \tag{16}$$

In addition to these relations, the vapor phase satisfies the equation of state

$$p = \rho RT \tag{17}$$

the enthalpy changes for vapor and liquid phases are defined

$$h_2 - h_1 = c_p (T_2 - T_1) \tag{18}$$

$$h_{p2} - h_{p1} = c_\ell (T_{p2} - T_{p1}) \tag{19}$$

where c_p and c_ℓ are constant. Further, the difference between enthalpies of vapor and liquid phase at the same temperature is the latent heat of vaporization

$$h(T) - h_p(T) = h_\ell \tag{20}$$

and since the latent heat h_ℓ will be assumed constant, it follows for thermodynamic consistency that

$$c_p = c_\ell \tag{21}$$

Finally, the State 2 at the end of the saturation relaxation zone must be such that the pressure, p_2, of the vapor and the temperature, T_{p2}, of the liquid droplets satisfy the thermodynamic saturation condition. For the present purposes, this may be taken as the familiar Clausius-Clapeyron relationship and, assuming the initial state before the gasdynamic shock was one of complete thermodynamic equilibrium, this relationship may be written

$$\frac{p_2}{p_o} = e^{\frac{h_\ell}{RT_o}\left(1 - \frac{T_o}{T_{p2}}\right)} \tag{22}$$

Strictly speaking, the change across the saturation relaxation zone is still not completely determined because the integrals contain distributions of velocity, temperature, etc., which are unknown. It will transpire, however, that the changes from State 1 to State 2 are sufficiently small, in most cases of interest, that the distributions may be approximated well by linear interpolation between the end points. Therefore, the momentum exchange integral, Equations (11) and (15), will be approximated

$$\int_1^2 \mu_v \, u dx \cong \rho_o \, u_o \, \phi_2 \cdot \frac{1}{2}(u_1 + u_2) \tag{23}$$

and the energy exchange integral, Equations (13) and (16)

$$\int_1^2 \mu_v \left(h + \frac{1}{2}u^2\right) dx \cong \rho_o \, u_o \, \phi_2 \left\{\frac{1}{2}(h_1 + h_2) + \frac{1}{2}\left(\frac{u_1^2}{2} + \frac{u_2^2}{2}\right)\right\} \tag{24}$$

Under this approximation, the change of state between Stations 1 and 2 is well determined and may be computed so long as the properties γ, R, and h_ℓ, together with the initial state of the flow, are known. The solution is algebraically complicated, however, and it is more convenient and much more informative physically to take advantage of the fact that $\phi << 1$ for usual cases of interest. The conditions at State 2 may then be written in the following good approximation, where $\eta \equiv \rho_{po}/\rho_o$ is the ratio of the mass flow of liquid to the mass flow of vapor ahead of the shock.

$$\phi_2 \cong - \frac{\eta \log (p_1/p_o)}{\frac{\gamma - 1}{\gamma} \frac{h_\ell}{RT_o}\left(\frac{h_\ell}{RT_o} + \gamma M_o^2\right)} \tag{25}$$

$$\frac{u_2}{u_1} = 1 + \frac{\phi_2}{1 - M_1^2} \tag{26}$$

$$\frac{p_2}{p_1} = 1 - \frac{\gamma M_1^2}{1 - M_1^2} \phi_2 \tag{27}$$

$$\frac{\rho_1}{\rho_2} = 1 + \frac{\phi_2 M_1^2}{1 - M_1^2} \tag{28}$$

$$\frac{u_{p2}}{u_o} = 1 + \frac{\phi_2}{\eta} \tag{29}$$

$$\frac{\rho_{p2}}{\rho_{po}} = 1 - 2 \frac{\phi_2}{\eta} \tag{30}$$

$$\frac{T_{p2}}{T_o} = \frac{1}{1 - \frac{RT_o}{h_\ell} \log \frac{p_1}{p_o}} \tag{31}$$

and finally, the new droplet radius is

$$\frac{\sigma_2}{\sigma_o} = 1 - \frac{\phi_2}{3\eta} \tag{32}$$

where it must be remembered that the value of ϕ_2 is negative. It should also be re-emphasized that the condition under which Equations (25) through (32) are valid is that ϕ_2 is small. In general, this condition is satisfied because h_ℓ / RT_o is large, usually of the order of 10. The change in droplet temperature across the saturation relaxation zone, however, is not small, as may be seen from Equation (31). This relation follows directly from the Clausius-Clapeyron relation, the only approximation being that $p_2/p_o \cong p_1/p_o$ in the denominator.

3.3 VELOCITY AND THERMAL EQUILIBRATION ZONE

In this final and most extensive zone, the velocities and temperatures of the vapor and liquid phases reach thermodynamic equilibrium, and the mass transfer from the liquid-to-vapor phase takes place at a rate so as to maintain the saturation condition between the liquid temperature and the vapor pressure. The equilibrium State 3 is characterized by the conditions

$$T_3 = T_{p3} \tag{33}$$

$$u_3 = u_{p3} \tag{34}$$

in addition to the conservation relations across an appropriate part of the shock. It will prove simpler to compute the changes across the final zone, from a computation of the changes across the complete shock and the known changes across the first two zones, than to develop a separate analysis for the final zone. The continuity equation for the complete system is then

$$(\rho_3 + \rho_{p3})u_3 = (1 + \eta)\rho_o u_o \tag{35}$$

and if we extend the notation for vapor production employed previously, we have the conservation for vapor phase as

$$\rho_3 u_3 = (1 + \phi_3)\rho_o u_o \tag{36}$$

which defines the quantity ϕ_3. Correspondingly,

$$\rho_{p3} u_3 = (\eta - \phi_3)\rho_o u_o \tag{37}$$

The momentum equation for the complete system may be written, utilizing Equation (35), as

$$p_3 - p_o = \rho_o u_o (1 + \eta)(u_o - u_3) \tag{38}$$

and the energy equation is just

$$\rho_3 u_3 \left(h_3 + \frac{1}{2}u_3^2\right) + \rho_{p3} u_3 \left(h_{p3} + \frac{1}{2}u_3^2\right) = \rho_o u_o \left(h_o + \frac{1}{2}u_o^2\right) + \rho_{po} u_o \left(h_{po} + \frac{1}{2}u_o^2\right) \tag{39}$$

Utilizing the foregoing relations, this may be written directly as

$$h_3 + \frac{1}{2}u_3^2 = h_o + \frac{1}{2}u_o^2 - h_\ell \frac{\phi_3}{1 + \eta} \tag{40}$$

Finally, in addition to the equation of state for the perfect gas, satisfied by the vapor phase, and the definition of the vapor enthalpy given previously, the temperature and pressure of the final equilibrium state must satisfy the Clausius-Clapeyron relation or saturation condition

$$\frac{p_3}{p_o} = e^{\frac{h_\ell}{RT_o}\left(1 - \frac{T_o}{T_3}\right)} \tag{41}$$

These relations, which define completely the possible relations between upstream and downstream equilibrium state, are not readily handled in a manner similar to those for the conventional shock. In acutal computation, it is convenient to select the pressure ratio, p_3/p_o, as the prescribed quantity rather than the Mach number ahead of the shock, other conditions ahead of the shock being assumed known. Then, from Equation (41) and the equation of state,

$$\frac{\rho_3}{\rho_o} = \left(1 - \frac{RT_o}{h_\ell} \log \frac{p_3}{p_o}\right) \frac{p_3}{p_o} \tag{42}$$

while from a combination of the momentum and energy equations corresponding to the Rankine-Hugoniot relation

$$\phi_3 = \frac{2}{\bar{\gamma}-1} \left\{ \frac{\bar{\gamma}(1 - \rho_o/\rho_3) - \left[1 - \frac{\bar{\gamma}+1}{2}(1 - \rho_o/\rho_3)\right]\left[\rho_3/\rho_o - 1\right]}{2\frac{h_\ell}{RT_o} - \left(\frac{p_3}{p_o} - 1\right)\frac{\rho_o}{\rho_3}} \right\} \tag{43}$$

where

$$\bar{\gamma} = \frac{(1+\eta)\gamma}{1+\eta\gamma} \tag{44}$$

and at this stage of the calculation, all quantities on the right side of Equation (43) are known. Other quantities of interest then follow directly as

$$M_o^2 = \frac{p_3/p_o - 1}{(1+\eta)\gamma\left[1-(1+\phi_3)\rho_o/\rho_3\right]} \tag{45}$$

$$\frac{u_3}{u_o} = (1+\phi_3)\frac{\rho_o}{\rho_3} \tag{46}$$

$$\frac{\rho_{p3}}{\rho_{po}} = \left(1 - \frac{\phi_3}{\eta}\right)\frac{u_o}{u_3} \tag{47}$$

$$\frac{\sigma_3}{\sigma_o} = \left(1 - \frac{\phi_3}{\eta}\right)^{1/3} \tag{48}$$

A limitation to these formulas clearly occurs when ϕ_3 becomes equal to η. Physically, this indicates that all of the liquid has been transformed to vapor by the end of the velocity and thermal equilibration zone. This result is shown directly from Equations (47) and (48), which indicate that the liquid phase density, ρ_{p3}, and the liquid droplet radius, σ_3, vanish under these circumstances. For initial states, shock conditions or liquid-vapor parameters which would lead to larger values of $\phi_3 > \eta$, a different formulation of the problem is required. For these cases in question, the final state is not a saturation state and, hence, is not described by the Clausius-Clapeyron equation. Rather, the final state is characterized by the fact that $\phi_3 = \eta$, that is, all liquid has been transformed to vapor. Therefore, in formulating the final state, Equations (41) and (42) must be deleted and the value η substituted for ϕ_3 in Equations (43) and (45) through (48). Then Equation (43) replaces the conventional Rankine-Hugoniot relation, the simultaneous solution of Equations (43) and (45) gives the ratios p_3/p_o and ρ_3/ρ_o for any prescribed upstream Mach number, and the temperature ratio follows from the conventional equation of state

$$\frac{T_3}{T_o} = \frac{p_3}{p_o}\frac{\rho_o}{\rho_3} . \tag{49}$$

Finally, the velocity ratio follows from Equation (46) and there are no liquid state quantities to be computed.

It is interesting to note that the thermal and velocity equilibration zone is complete when the liquid phase disappears and, consequently, there is not only a difference in the final state, depending upon whether or not it is wet, but there is also a difference in the approach to the final state. When the final state is wet, equilibrium is reached because the velocity and temperature of the two phases approach each other. When the final state is superheated, equilibrium is reached because the liquid state disappears.

3.4 SHOCK STRUCTURE FOR WET ALKALI METAL VAPORS

Because of the several assumptions that have been made in the analysis, as well as because of the relative complexity of the results, it is appropriate to consider some specific examples to assure that the assumptions may be reasonably well satisfied and to illustrate the magnitude of

the jumps across each of the three zones. The key assumptions made in the analysis were (1) constant specific heats in the vapor phase, (2) constant value of the latent heat of vaporization, and (3) density ratio of liquid to vapor was large, i.e., $\rho_\ell / \rho > 10^2$. In addition, it is required to know appropriate values of γ and the latent heat parameter h_ℓ/RT in the useful range of any pure substance.

The alkali metals constitute a suitable class of substances because their critical states are rather far removed from the thermodynamic states in which one usually works. Also, the alkali metals are particularly appropriate because the current applications to vapor power cycles utilize the wet range of their thermodynamic states. The appropriate physical properties and parametric quantities for the saturated alkali metal vapor-liquid systems are given in Table I for a range of operating temperatures. The basic data from which these values were calculated were obtained from Reference 11.

It is clear from the table that, for each of the alkali metals vapors, the values of specific heat, c_p, are essentially constant over the range of temperatures; also, the ratio of specific heats γ is nearly constant and equal to 1.60. For each of the elements, the latent heat varies less than 15 percent over the temperature range, indicating that the specific heat values for liquid and vapor are not exactly equal. In general, the liquid specific heat ranges approximately 30 percent larger than that for the vapor, a fact that will introduce slight, but not serious, errors in the calculated shock properties. The ratios of liquid-to-vapor density, ρ_ℓ / ρ, are all large enough to validate the assumption that the volume occupied by the liquid is negligible in calculating the vapor state. Moreover, it is generally large enough to assure that the order-of-magnitude estimates for thicknesses of the various zones are accurate. In the last column, the values of the significant condensation parameter, h_ℓ/RT, are shown and appear to lie within the range $5.0 \leq h_\ell/RT \leq 15.0$, a fact which will be utilized in the following calculations.

In Tables II and III, calculated results are presented for selected values of liquid mass fraction, initial Mach number, ratio of specific heats, and latent heat parameter, h_ℓ/RT_o, chosen on the basis of Table I, to indicate the effects of each of these parameters on the shock structure. Table II pertains to the value $\eta = 0.25$, that is, a liquid mass fraction of 0.20 or a "quality" of 80 percent. Table III pertains to the value $\eta = 0.667$, that is, a liquid mass fraction of 0.40 or a quality of 60 percent. In each table, that is, for each liquid mass fraction, results are given for two shock Mach numbers, 1.5 and 2.0, and, at each Mach number, for the three values of the latent heat parameter, $h_\ell/RT_o = 5.0$, $= 10.0$, and $= 15.0$. For each of these cases, the tabulation is arranged so that the ratio or change across the complete shock appears first and the changes across each of the three structural zones appear below it. For example,

TABLE I

SOME PROPERTIES OF THE SATURATED ALKALI METAL VAPOR - LIQUID SYSTEM

Alkali Metal	T (^oR)	p (psia)	C_p (Btu/lb ^oF)	γ	h_ℓ (Btu/lb)	ρ_ℓ/ρ	$\frac{h_\ell}{RT}$
Li	2400	1.45	0.710	1.60	8755	6.48×10^4	13.8
	2700	6.64	0.708	1.57	8783	1.51×10^4	12.2
	3000	22.5	0.708	1.55	8255	4.72×10^3	10.9
	3500	107.7	0.709	1.52	7837	1.06×10^2	9.07
Na	1300	3.39×10^{-2}	0.215	1.64	1855	1.33×10^6	12.1
	1500	2.34×10^{-1}	0.214	1.62	1806	1.43×10^5	10.5
	2000	9.15	0.213	1.57	1685	4.27×10^3	7.7
	2500	80.2	0.213	1.53	1576	5.4×10^2	5.6
K	1300	0.236	0.127	1.65	906	6.79×10^4	14.0
	1500	1.50	0.127	1.64	897	1.18×10^4	12.2
	2000	29.0	0.126	1.60	835	7.17×10^2	8.82
	2500	165	0.126	1.57	777	1.40×10^2	6.78
Rb	1300	0.576	0.0579	1.64	372	2.37×10^4	12.7
	1500	3.08	0.0578	1.63	362	4.92×10^3	10.9
	2000	44.4	0.0576	1.59	335	4.13×10^2	7.90
	2500	210	0.0576	1.55	312	1.01×10^2	6.09
Cs	1300	0.801	0.0372	1.63	226	1.37×10^4	12.1
	1500	3.95	0.0372	1.62	219	3.10×10^3	10.0
	2000	49.7	0.0371	1.57	205	3.00×10^2	7.56
	2500	215	0.0372	1.54	187	$.805\times10^2$	5.75

TABLE II

VARIATIONS OF VAPOR AND LIQUID STATE ACROSS EACH ZONE OF SHOCK WAVE FOR CONDITIONS $\gamma = 1.6$, $\eta = 0.25$

M_o	1.5			2.0		
h_ℓ/RT_o	5	10	15	5	10	15
p_3/p_o	3.52	4.0	4.19	6.35	7.30	7.48
p_1/p_o	2.54	2.54	2.54	4.69	4.69	4.69
p_2/p_1	1.02	1.01	1.00	1.02	1.01	1.00
p_3/p_2	1.36	1.56	1.65	1.33	1.54	1.59
ρ_3/ρ_o	2.69	3.38	3.73	3.98	5.93	6.52
ρ_1/ρ_o	1.74	1.74	1.74	2.36	2.36	2.36
ρ_2/ρ_1	1.02	1.01	1.00	1.01	1.00	1.00
ρ_3/ρ_2	1.52	1.92	2.14	1.67	2.51	2.77
T_3/T_o	1.31	1.18	1.12	1.60	1.22	1.16
T_1/T_o	1.46	1.46	1.46	1.98	1.98	1.98
T_2/T_1	1.04	1.02	1.00	1.03	1.01	1.00
T_3/T_2	0.86	0.79	0.77	0.79	0.61	0.58
u_3/u_o	0.44	0.33	0.33	0.34	0.21	0.19
u_1/u_o	0.57	0.57	0.57	0.42	0.42	0.42
u_2/u_1	0.97	0.99	1.00	0.97	0.99	1.00
u_3/u_2	0.80	0.58	0.57	0.83	0.51	0.43
ρ_{p3}/ρ_{po}	0.98	1.34	1.83	0.00	0.00	0.29
ρ_{p1}/ρ_{po}	1.00	1.00	1.00	1.00	1.00	1.00
ρ_{p2}/ρ_{p1}	1.12	1.04	1.01	1.15	1.05	1.03
ρ_{p3}/ρ_{p2}	0.85	1.29	1.79	0.00	0.00	0.28
T_{p3}/T_{po}	1.31	1.18	1.12	1.59	1.22	1.16
T_{p1}/T_{po}	1.00	1.00	1.00	1.00	1.00	1.00
T_{p2}/T_{p1}	1.23	1.10	1.07	1.45	1.18	1.12
T_{p3}/T_{p2}	1.06	1.08	1.05	1.10	1.03	1.05

TABLE II (Continued)

M_o	1.5			2.0		
h_ℓ/RT_o	5	10	15	5	10	15
u_{p3}/u_{po}	0.44	0.33	0.33	0.34	0.21	0.19
u_{p1}/u_{po}	1.00	1.00	1.00	1.00	1.00	1.00
u_{p2}/u_{p1}	0.94	0.98	0.99	0.93	0.97	0.99
u_{p3}/u_{p2}	0.46	0.33	0.34	0.36	0.22	0.19
σ_3/σ_o	0.72	0.74	0.81	0.00	0.00	0.36
σ_1/σ_o	1.00	1.00	1.00	1.00	1.00	1.00
σ_2/σ_1	1.02	1.01	1.00	1.02	1.01	1.00
σ_3/σ_2	0.71	0.74	0.81	0.00	0.00	0.36

TABLE III

VARIATIONS OF VAPOR AND LIQUID STATE ACROSS EACH ZONE OF SHOCK WAVE FOR CONDITIONS $\gamma = 1.6$, $\eta = 0.667$

M_o	1.5			2.0		
h_ℓ/RT_o	5	10	15	5	10	15
p_3/p_o	5.08	5.53	5.61	8.93	9.64	10.07
p_1/p_o	2.54	2.54	2.54	4.69	4.69	4.69
p_2/p_1	1.06	1.02	1.01	1.04	1.02	1.01
p_3/p_2	1.89	2.14	2.19	1.83	2.02	2.14
ρ_3/ρ_o	3.39	4.60	4.93	4.94	7.53	8.52
ρ_1/ρ_o	1.75	1.75	1.75	2.36	2.36	2.36
ρ_2/ρ_1	1.04	1.01	1.00	1.03	1.01	1.00
ρ_3/ρ_2	1.86	2.60	2.82	2.03	3.16	3.61
T_3/T_o	1.50	1.20	1.14	1.78	1.30	1.18
T_1/T_o	1.46	1.46	1.46	1.98	1.98	1.98
T_2/T_1	1.10	1.03	1.01	1.07	1.03	1.01
T_3/T_2	0.93	0.80	0.77	0.84	0.64	0.59
u_3/u_o	0.32	0.31	0.23	0.25	0.25	0.15
u_1/u_o	0.57	0.57	0.57	0.42	0.42	0.42
u_2/u_1	0.92	0.97	0.99	0.92	0.97	0.99
u_3/u_2	0.61	0.56	0.41	0.65	0.61	0.36
ρ_{p3}/ρ_{po}	2.48	2.91	3.38	2.31	2.28	3.80
ρ_{p1}/ρ_{po}	1.00	1.00	1.00	1.00	1.00	1.00
ρ_{p2}/ρ_{p1}	1.12	1.04	1.02	1.15	1.05	1.03
ρ_{p3}/ρ_{p2}	2.21	2.80	3.31	2.01	2.17	3.69
T_{p3}/T_{po}	1.50	1.20	1.14	1.78	1.30	1.18
T_{p1}/T_{po}	1.00	1.00	1.00	1.00	1.00	1.00
T_{p2}/T_{p1}	1.23	1.10	1.07	1.45	1.18	1.12
T_{p3}/T_{p2}	1.22	1.09	1.07	1.23	1.10	1.05

TABLE III (Continued)

M_o	1.5			2.0		
h_ℓ/RT_o	5	10	15	5	10	15
u_{p3}/u_{po}	0.32	0.31	0.23	0.25	0.25	0.15
u_{p1}/u_{po}	1.00	1.00	1.00	1.00	1.00	1.00
u_{p2}/u_{p1}	0.94	0.98	0.99	0.93	0.98	0.99
u_{p3}/u_{p2}	0.34	0.32	0.23	0.27	0.26	0.15
σ_3/σ_o	0.94	0.88	0.92	0.84	0.64	0.83
σ_1/σ_o	1.00	1.00	1.00	1.00	1.00	1.00
σ_2/σ_1	1.02	1.01	1.00	1.02	1.01	1.00
σ_3/σ_2	0.92	0.87	0.92	0.82	0.63	0.83

when the parameters are $\eta = 0.667$, $M_o = 1.5$, and $h_\ell/RT = 5.0$, the pressure ratio across the complete shock is 5.08. The pressure ratio, p_1/p_o, across the gasdynamic shock is 2.54; the pressure ratio, p_2/p_1, across the vapor relaxation zone is 0.990; and the pressure ratio, p_3/p_2, across the velocity and thermal equilibration zone is 2.02. Other quantities are tabulated in a similar manner.

In general, the changes are in the directions and of the magnitudes that have been indicated in the previous discussion. The changes across the gasdynamic shock and those across the equilibration zone are of the same order of magnitude for the variables associated with the vapor phase. The changes across the equilibration zone are dominant for the liquid state variables. With the exception of the liquid droplet temperature, the changes across the vapor relaxation zone are of smaller magnitude than those across the other two. The droplet temperature ratio, T_{p2}/T_{p1}, is surprisingly large, responding, of course, to the pressure ratio, p_1/p_o, across the gasdynamic shock according to Equation (31). Usually, the droplet temperature acquires the largest portion of its temperature rise across the vapor relaxation zone; this temperature rise originates principally from the latent heat brought to the droplet by the condensation process which occurs in response to the vapor pressure rise across the gasdynamic shock.

SECTION 4

STRUCTURE OF VELOCITY AND THERMAL EQUILIBRATION ZONE

Of the three zones of the shock wave that have been discussed, the final equilibration zone, in which the velocities and temperature of the two phases achieve equality, dominates the thickness of the complete wave. Moreover, when the dimension of the shock thickness is such as to become of importance in comparison with other physical dimensions of the problem, it is this region that will first be the controlling one and whose detailed structure will enter into the solution of the boundary value problem. Consequently, this region will be examined in detail and some examples of its structure will be computed.

4.1 EQUATIONS DESCRIBING EQUILIBRATION ZONE

Denoting as before the mass rate of vapor production per unit volume as μ_v, the continuity equation for vapor flow is

$$\frac{d}{dx}(\rho u) = \mu_v \tag{50}$$

and the continuity equation for the mixture is

$$\rho u + \rho_p u_p = (\rho_3 + \rho_{p3}) u_3 \tag{51}$$

because at State 3, far downstream of the shock wave, the velocities of the two phases are equal. In the same manner, the conservation of momentum becomes

$$\rho u^2 + \rho_p u_p^2 + p = (\rho_3 + \rho_{p3}) u_3^2 + p_3 \tag{52}$$

where it has been assumed explicitly that within this relatively thick equilibration layer, the viscous stresses associated with gross deformation of the vapor phase are negligible. When only the particulate phase is considered, account must be taken of the rate at which mass is lost from the liquid phase and of the forces exerted by the vapor upon the droplets.

Because the vapor flow about the droplet is dominated by viscous stresses, we assume in this region that the mass exchange between phases occurs at the droplet velocity. Also, and largely because we assume that the viscous interaction between a droplet and the vapor is not significantly affected by the phase change and, consequently, the force retarding the motion of a droplet through the vapor may be written

$$f = (6\pi\sigma\mu(u_p - u)\alpha_1(Re) \tag{53}$$

The factor $\alpha_1(Re)$ is a function of the Reynolds number of the droplet motion which corrects Stokes law for the Reynolds number range of unity and larger. One such empirical correction has been given by Rannie.[10] The total force of interaction between the two phases in a unit volume is nf, where n is the number of droplets per unit volume. The density, ρ_p, of the liquid phase, considered as a disperse continuous medium, is $nm = \rho_p$, where m is the local mass of a single droplet. As discussed in some detail in Reference 4, it usually proves convenient to define a length, λ_v, which is characteristic of the velocity equilibration process

$$\lambda_v = \frac{m_o a_o}{6\pi\sigma_o\mu_o} \tag{54}$$

where the subscripts refer to the state far ahead of the shock. It is specifically assumed that both sound speed a in the vapor and the viscosity of the vapor vary with temperature so that a/μ is constant throughout the shock. The value of λ_v is roughly the distance that a droplet will move while it reduces the relative velocity between the vapor and itself to e^{-1} of its initial value, assuming that the mixture is moving with a speed comparable to the sonic velocity. Utilizing the foregoing assumptions and definitions, the equation of motion for the liquid phase may be written

$$u_p \frac{du_p}{dx} = -a \frac{u_p - u}{\lambda_v} \frac{\alpha_1(Re)}{\Sigma} \tag{55}$$

where

$$\Sigma = (\sigma/\sigma_o)^2 \tag{56}$$

is the ratio of local surface area of a droplet to its original area upstream of the shock.

Formulation of energy conservation through the shock requires care in treating the different phases, as did the foregoing consideration of momentum conservation. For the two phases together, however, the exchange and interaction terms cancel each other and the energy equation may be written

$$\rho u\left(h + \frac{1}{2} u^2\right) + \rho_p u_p \left(h_p + \frac{1}{2} u_p^2\right) = \rho_3 u_3 \left(h_3 + \frac{1}{2} u_3^2\right) + \rho_{p3} u_3 \left(h_{p3} + \frac{1}{2} u_3^2\right) \tag{57}$$

Through the definition of the latent heat, Equation (20), and the assumptions that the latent heat and specific heats are constant, Equation (21), the above relation may be conveniently written

$$\rho u \left(c_p T + \frac{1}{2} u^2\right) + \rho_p u_p \left(c_p T_p + \frac{1}{2} u^2\right)$$

$$+\left(\rho_{p3} u_{p3} - \rho_p u_p\right) h_\ell = \left(\rho_3 + \rho_{p3}\right) u_3 \left(c_p T_3 + \frac{1}{2} u_3^2\right) \tag{58}$$

This form has the advantage of showing explicitly how the latent heat of phase transition enters the problem and is more suitable for computation.

In formulating the energy equation for the liquid phase alone, detailed account must be taken of the enthalpy changes associated with phase transition, the heat transferred by thermal conduction between the two phases, and the work done by the flowing vapor on the system of liquid droplets. The vapor leaving the droplet surface carries with it the heat, $h_p + 1/2\ u_p^2 + h_\ell$, per unit mass, and, to the same approximation used in formulating the momentum exchange between phases, the heat lost from the droplets because of thermal conductivity is

$$\rho_p\ ac_p\ \frac{T_p - T}{\lambda_T}\ \frac{\alpha_2(\mathrm{Re})}{\Sigma} \tag{59}$$

The quantity λ_T, the thermal equilibration length, is defined

$$\lambda_T = \frac{m_o c_{p_o} a_o}{4\pi\sigma_o k_o} \tag{60}$$

in the same spirit as Equation (54) defining the velocity equilibration length. The function $\alpha_2(\mathrm{Re})$ corrects the simple conduction formula for the effects of Reynolds number larger than unity.

Finally, the work done by the droplets in moving through the vapor is equal to the product of the drag force between phases and u_p, the droplet velocity. The energy equation for the liquid phase may then be written in the alternate forms

$$\frac{d}{dx}\left\{\rho_p u_p \left(h_p + \frac{1}{2} u_p^2\right)\right\} = -\mu_v \left\{h_p + \frac{1}{2} u_p^2 + h_\ell\right\} - \rho_p \, a u_p \frac{u_p - u}{\lambda_v} \frac{\alpha_1(\mathrm{Re})}{\Sigma} - \rho_p a c_p \frac{T_p - T}{\lambda_T} \frac{\alpha_2(\mathrm{Re})}{\Sigma_1} \tag{61}$$

or

$$\rho_p u_p c_p \frac{dT_p}{dx} = -\mu_v h_\ell - \rho_p a c_p \frac{T_p - T}{\lambda_T} \frac{\alpha_2(\mathrm{Re})}{\Sigma} \tag{62}$$

The second form, Equation (62), follows from the more basic formulation by utilizing the equation of continuity for liquid phase and the equation of motion, Equation (55).

The structure of the equilibration zone is completely described by Equations (50), (51), (52), (55), (58), and (62), together with the general equations of state for the vapor

$$p = \rho R T \tag{63}$$

and the Clausius-Clapeyron equation, which now relates the droplet temperature and the vapor pressure

$$\frac{p}{p_3} = e^{\frac{h_\ell}{RT_3}\left(1 - \frac{T_3}{T_p}\right)} \tag{64}$$

Initial conditions on all variables are prescribed at State 2, the end of the vapor relaxation zone, and the reference condition is taken as State 3, the vinal state which is a singular point of the problem. Because the length variable x appears in the derivatives only, it may be eliminated between differential Equations (55) and (62), utilizing instead the droplet velocity as the independent variable. The structure may then be formulated employing equations

$$\frac{dT_p}{du_p} + \frac{h_\ell}{c_p} \frac{1}{\rho_p u_p} \frac{d(\rho u)}{du_p} = \beta \left(\frac{T_p - T}{u_p - u} \right) \tag{65}$$

$$\rho u + \rho_p u_p = \rho_3 u_3 + \rho_{p3} u_3 \tag{66}$$

$$(\rho u) u + (\rho_p u_p) u_p + p = \left[(\rho_3 u_3) + (\rho_{p3} u_{p3}) \right] u_3 + p_3 \tag{67}$$

$$\rho u \left(c_p T + \frac{1}{2} u^2 \right) + \rho_p u_p \left(c_p T_p + \frac{1}{2} u_p^2 \right) + (\rho_{p3} u_3 - \rho_p u_p) h_\ell$$

$$= \left[(\rho_3 u_3) + (\rho_{p3} u_3) \right] \left(c_p T_3 + \frac{1}{2} u_3^2 \right) \tag{68}$$

together with Equations (63) and (64). The parameter β is defined

$$\beta = \frac{\lambda_v}{\lambda_T} \frac{\alpha_2(\mathrm{Re})}{\alpha_1(\mathrm{Re})} \tag{69}$$

The five algebraic equations permit, in principle, the single differential Equation (65) to be reduced to one containing a single dependent variable which is numerically soluble. It is more convenient for practical calculations, because of the algebraic complexity, to convert to a set of three simultaneous differential relations and to compute step-wise from these.

Slightly different numerical procedures are needed according to whether or not the liquid phase vanishes at the end of the equilibration zone. This arises, for example, because of the term $\rho_p u_p$ in the denominator of Equation (65), a term which vanishes at the end point. The behavior of the solution near the singular point is changed, therefore, by the vanishing of the liquid phase. The numerical analysis is easily adjusted to accommodate this and it will not be discussed further.

4.2 EQUILIBRATION ZONE IN ALKALI METAL VAPORS

The structure of the equilibration zone has been computed in detail for the three examples corresponding to those given in Table III for an initial Mach number of 2.0. These examples represent the wet vapor with 40 percent liquid by weight, and the particles are still present at the end of the equilibration zone. The three examples use values of the latent heat parameter, h_ℓ / RT_o, equal to 5.0, 10.0, and 15.0, covering the appropriate range for the alkali metal vapors listed in Table I.

Figures 4-1, 4-2 and 4-3 show the more interesting features for each of the three equilibration zones whose structures were calculated. The gas velocity, gas temperature, gas mass flow, and droplet temperature are given as functions of the droplet velocity. This hodograph plot is more useful in presenting the structure of the zone than is the plot in physical space, because of the obvious reason that the physical extent of the equilibration zone is infinite. The actual distance from the end of the saturation relaxation zone is shown as a second, nonlinear scale along the abscissa, measured in terms of the velocity equilibration length λ_v.

In each case, the behavior of the vapor temperature is unusual enough to warrant some comment. The vapor temperature first rises, principally because of the dissipation associated with the droplet motion through the viscous vapor and then, as the droplet and vapor velocities approach each other, the temperature drops to the appropriate final value equal to the droplet temperature. It is the behavior near the final state that differs remarkably from one value of h_ℓ/RT_o to the other, and an examination of the three sets of curves reveals the mechanism of the process. For the value $h_\ell/RT_o = 5.0$, the droplet and vapor velocities equilibrate more rapidly than do the vapor temperatures or the vapor mass flow. The broken straight line on the curve indicates the equality of vapor and droplet velocities, showing that they tend to become nearly equal before the other critical changes are complete.

The values of x/λ_v which have been entered in Figures 4-1, 4-2 and 4-3 show this tendency very clearly. For $h_\ell/RT_o = 5$, which corresponds to $\eta = 1.05$ for the example, the results show that the vapor temperature and mass flow reach equilibration only for x/λ_v values far in excess of unity.

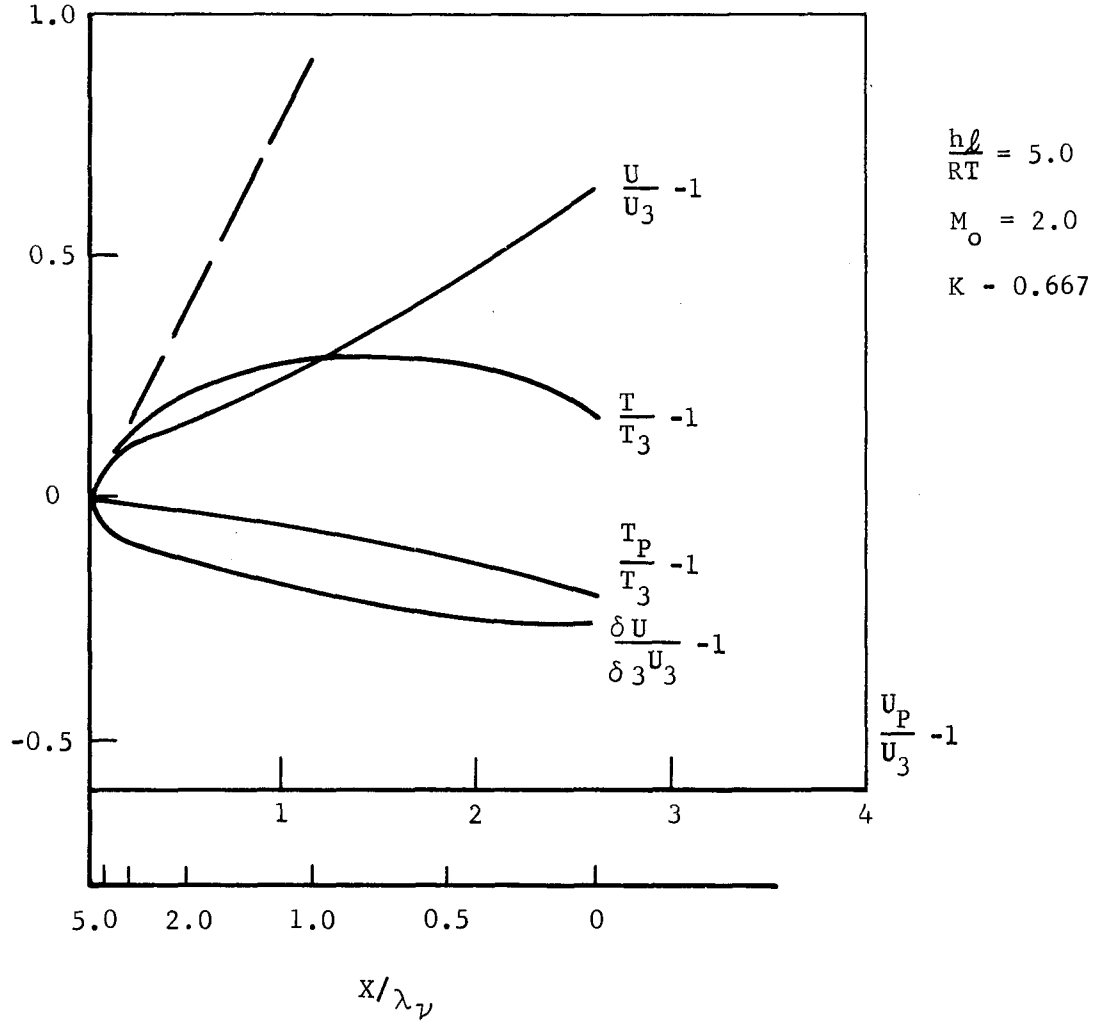

FIGURE 4-1. DISTRIBUTION OF VAPOR AND DROPLET PROPERTIES IN EQUILIBRATION ZONE OF NORMAL SHOCK, M_o = 2.0, γ = 1.6, η = 0.667, $h\ell/RT_o$ = 5.0

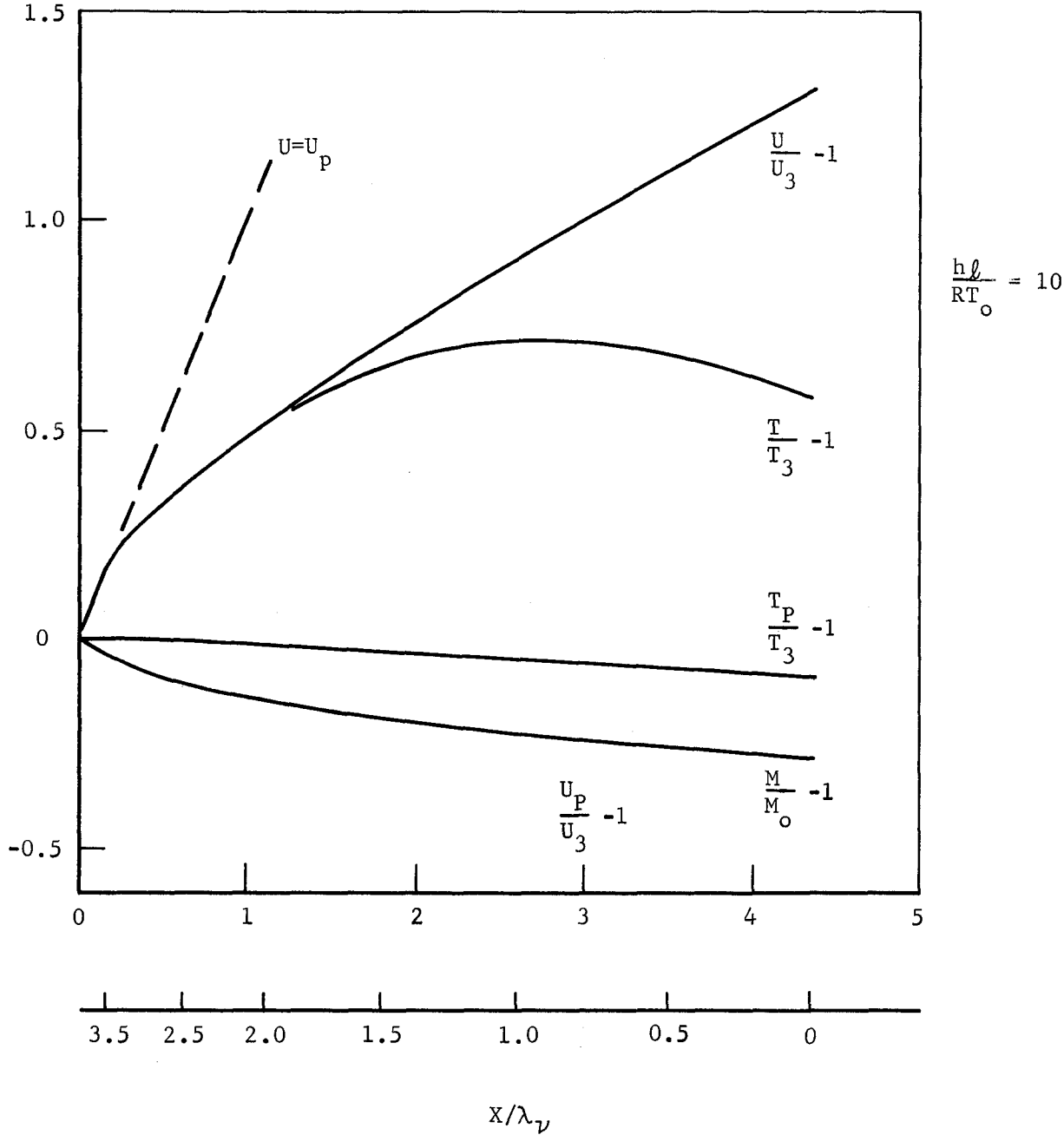

FIGURE 4-2. DISTRIBUTION OF VAPOR AND DROPLET PROPERTIES IN EQUILIBRATION ZONE OF NORMAL SHOCK, $M_o = 2.0$, $\gamma = 1.6$, $\eta = 0.667$, $h\ell/RT_o = 10.0$

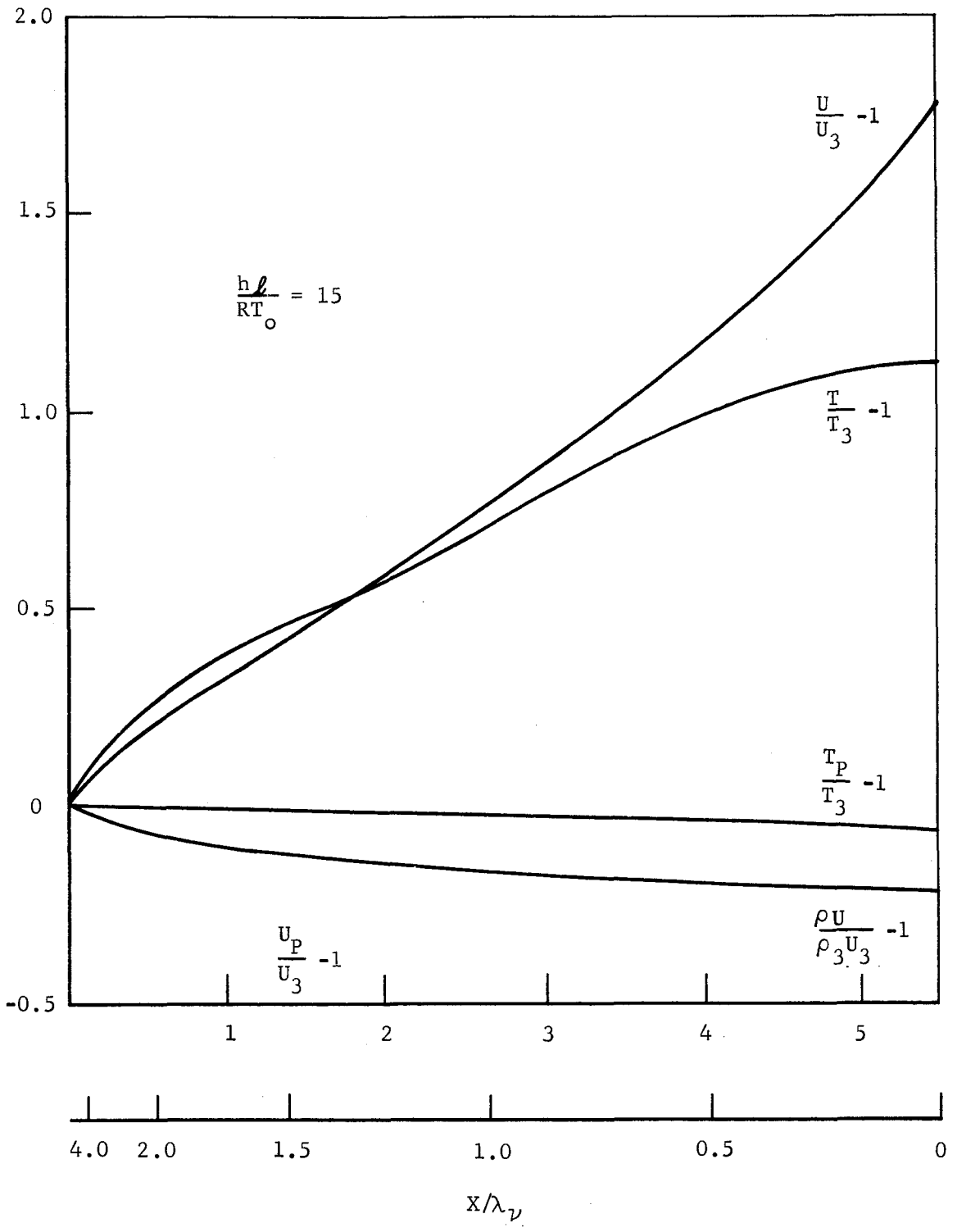

FIGURE 4-3. DISTRIBUTION OF VAPOR AND DROPLET PROPERTIES IN EQUILIBRATION ZONE OF NORMAL SHOCK, M_o = 2.0, γ = 1.6, η = 0.667, $h\ell/RT_o$ = 15.0.

SECTION 5

TEST FACILITY

For the potassium turbine erosion program, Aeronutronic provided a complete on-site potassium vapor test facility. Figure 5-1 is an external view of the fireproof potassium test building. The facility provides all the necessary services including 100 kw_e electrical power, argon cover gas, a nitrogen purge and fire deluge system, a large cooling air capacity, vacuum capabilities extending into the micron range, plus all of the necessary equipment for the safe handling of the alkali metals.

Figure 5-2 shows the boiling-condensing potassium loop prior to final insulation and startup. The loop is a closed cycle, forced convection, boiling-condensing welded type with a resistance-heated boiler capable of delivering a mass flow of 0.01 lb/sec of dry potassium vapor at 1500°F. Except for the Haynes-25 boiler preheater the loop is made of 304 and 316 stainless steels. The preheater, with nucleating fingers attached, also functions as a hot trap with zirconium as an oxygen affinity media. The loop has a resistance-heated dryer section capable of 100°F to 300°F of superheat. The remainder of the loop is trace heated. Figure 5-3 shows the installation drawing of the potassium loop.

Forced circulation is accomplished with a Mine Safety Appliances ac electromagnetic pump capable of producing a head rise of 35 psi at 0.01 lb/sec with a voltage input of 240 v. Flow is measured with a Mine Safety Appliances dc electromagnetic flow meter.

The condenser is air cooled, and, at the loop rated flow has demonstrated the ability to hold condensing pressures from 0.5 to 4.0 psia with reasonable ease. The test section is designed to house nozzle-wedge test specimens or the test turbine. Figure 5-4 is a schematic drawing of the test section showing the mounting of the test turbine. As shown in Figure 5-4, valving is arranged up- and downstream of the test section making isolation of this area relatively simple. This facilitates decontamination of the test area and also permits replacement of test specimens without undue loop contamination.

Figure 5-5 shows the main control panel for the loop. Control is maintained by manual manipulation of powerstat for power input, a boiler inlet flow control valve, a condenser level indicator, and associated pressure and

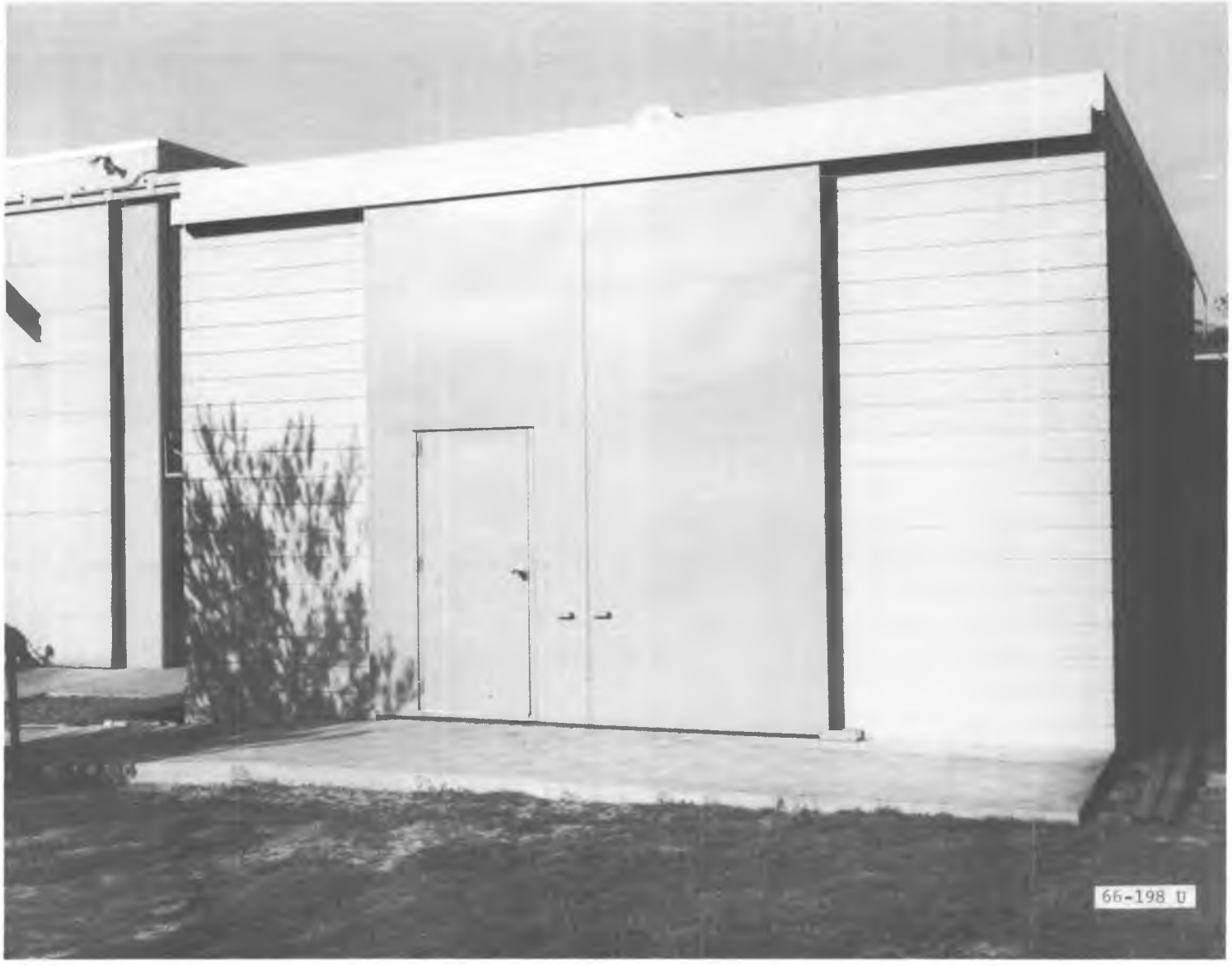

FIGURE 5-1. POTASSIUM FACILITY EXTERNAL VIEW

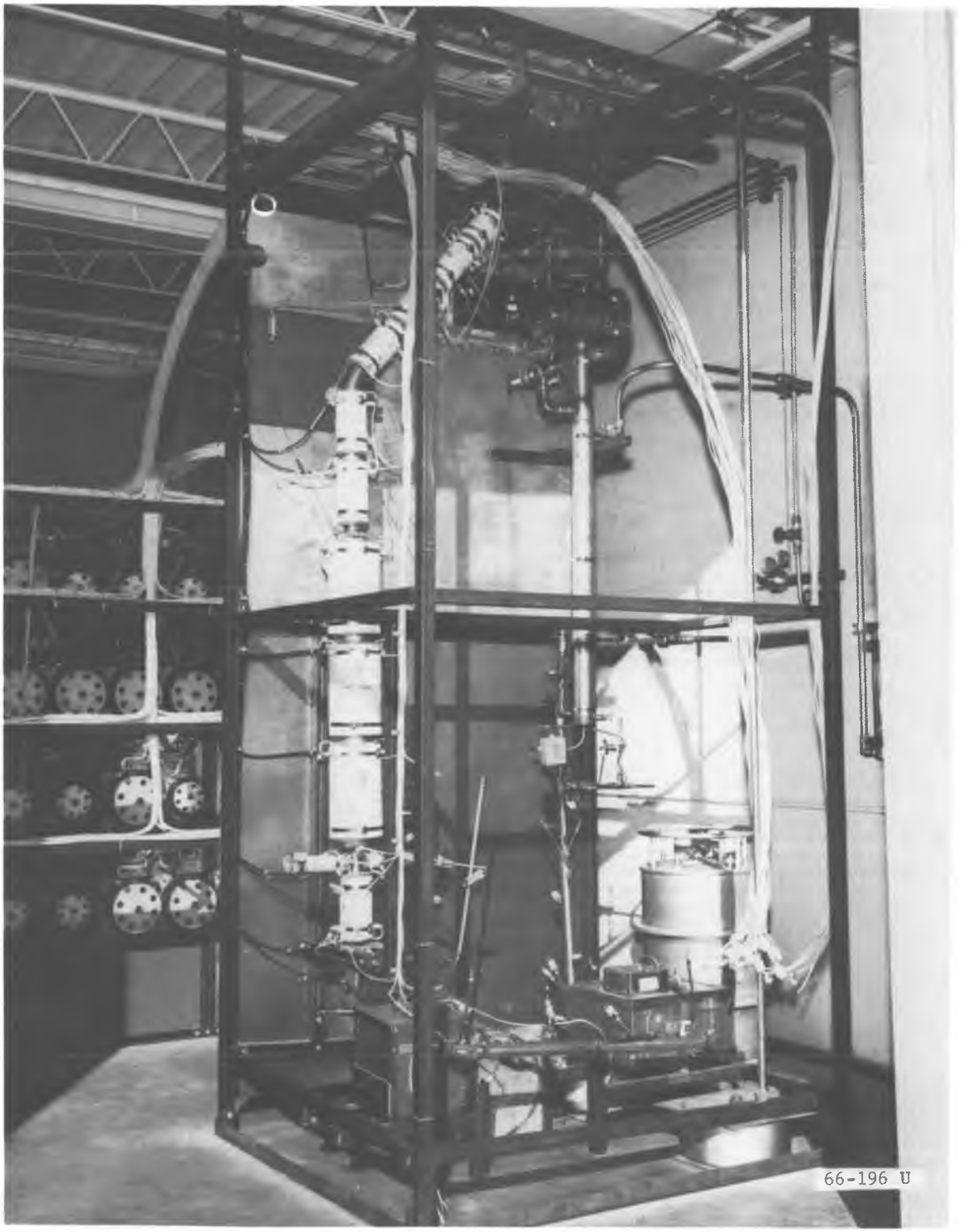

FIGURE 5-2. POTASSIUM LOOP PRIOR TO FINAL INSULATION

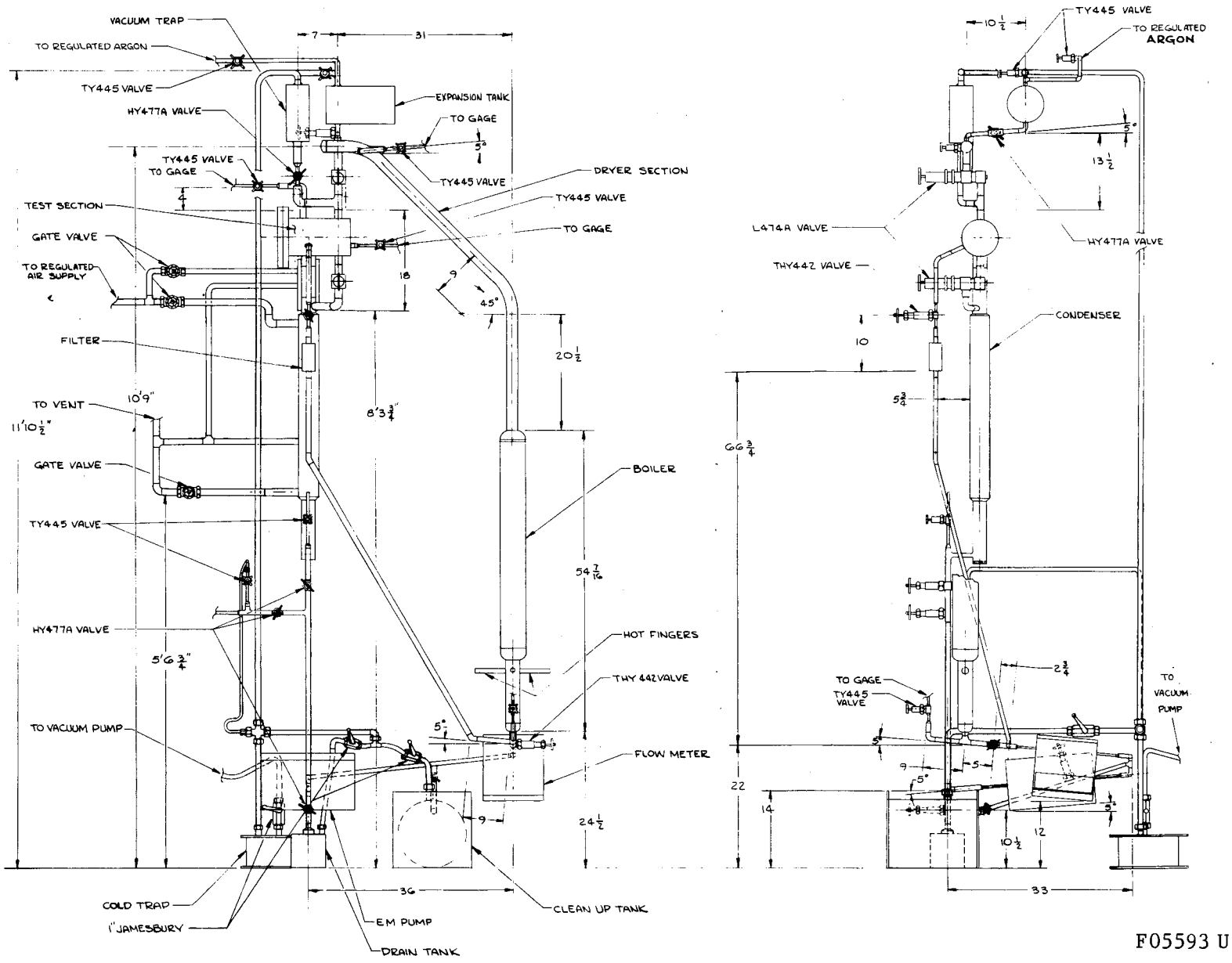

F05593 U

FIGURE 5-3. POTASSIUM LOOP INSTALLATION DRAWING

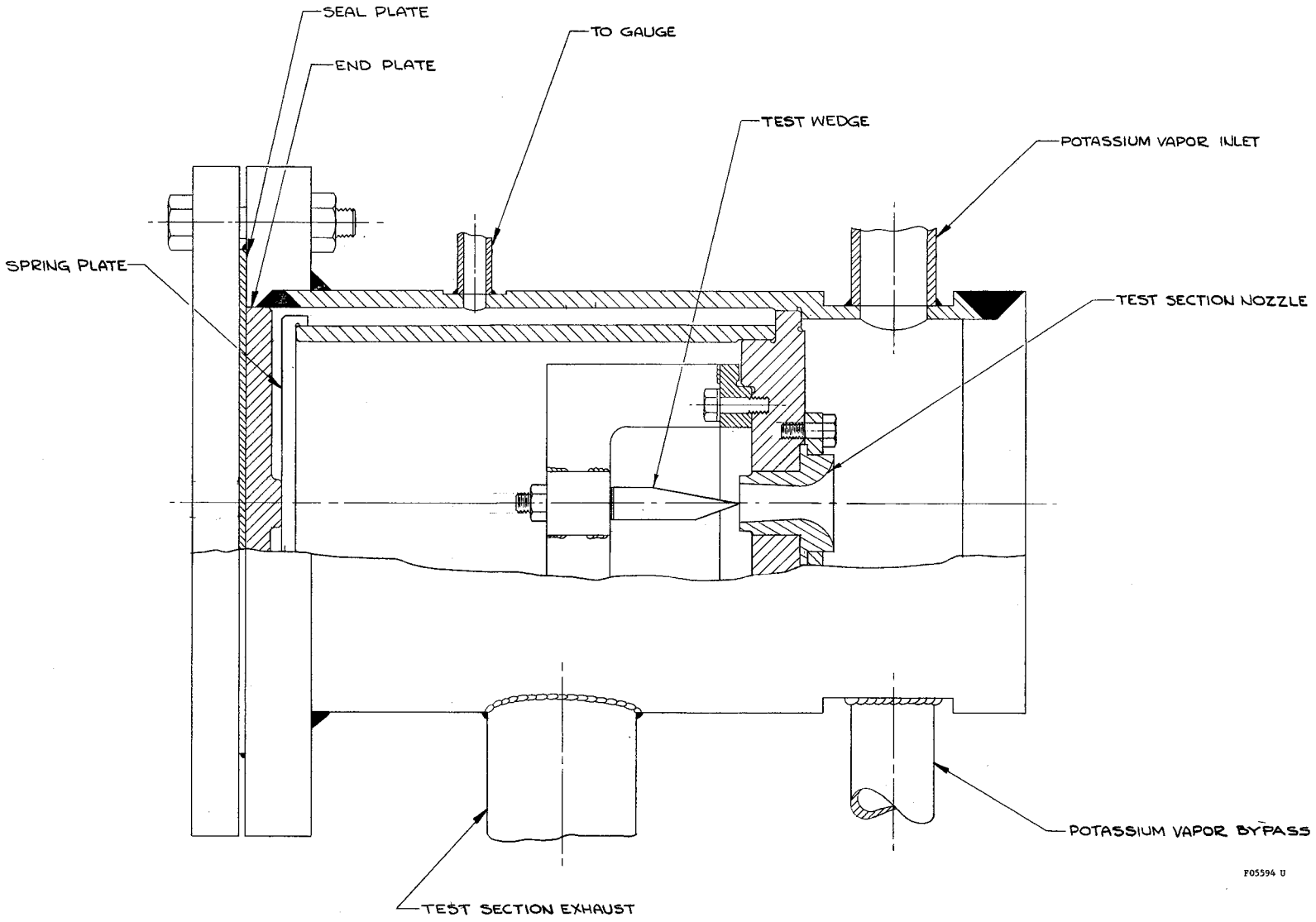

FIGURE 5-4. TEST SECTION LAYOUT DRAWING WITH MOUNTED NOZZLE-WEDGE SPECIMEN

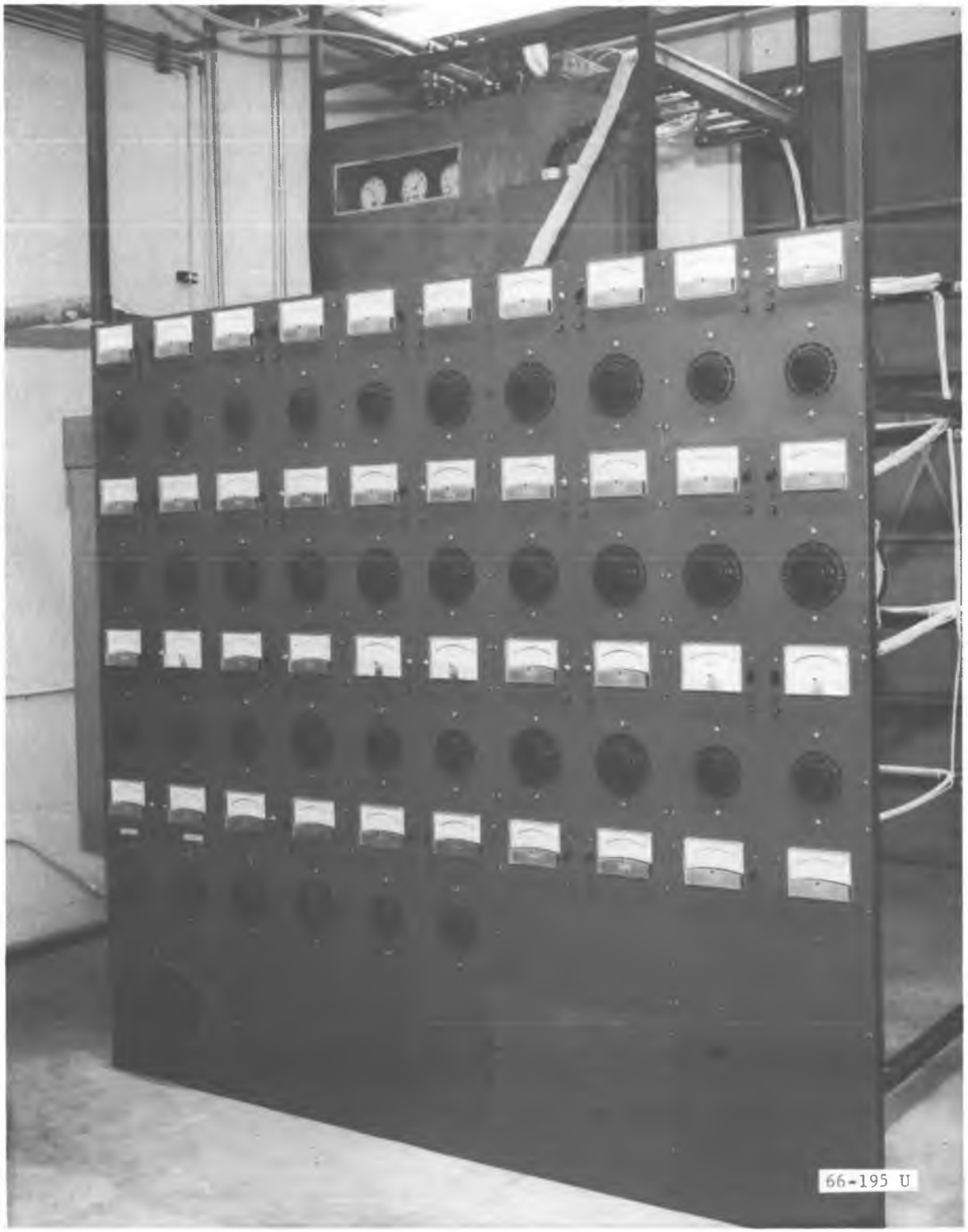

FIGURE 5-5. POTASSIUM LOOP CONTROL PANEL

temperature instrumentation. By filling the loop to a predetermined level and holding a prescribed level in the condenser loop, flow is proportional to the boiler input power. The power output of the boiler heaters is controlled by a variable voltage to each heater or pair of heaters. This allows good control and eliminates excessive temperature excursions in any one area of the boiler or dryer sections.

Instrumentation for the loop consists of C/A thermocouples and stainless steel welded Bourdon tube pressure gauges. The thermocouples are readout on a multipoint recorder or are led direct to a temperature compensated thermocouple meter. The multipoint recorder allows 20 data points to be recorded on a time sharing basis.

Pressures are measured with stainless steel Bourdon tube gauges protected from the high process fluid temperature by a length of potassium-filled line leading from the loop to the pressure gauge. These lines are traced with resistance heaters to maintain their operating temperature above the potassium freezing point. Experience to date has been satisfactory using these units.

SECTION 6

POTASSIUM DROPLET SIZE DETERMINATION

The erosion of turbine blades resulting from the flow of wet vapors has been subject to extensive empirical studies where the working vapor was steam. The technological preoccupation with this particular medium discouraged the sort of generalized investigation that would permit the results to be applied to other vapors. As a consequence, the erosion problem in turbines utilizing alkali metal vapors has motivated a new and more fundamental approach to the entire subject. One aspect of this effort involved the determination of droplet size. Toward this end, Aeronutronic developed a unique technique for this measurement. The principles underlying the method and its application to potassium turbine nozzles are described in this section.

6.1 OBLIQUE SHOCK WAVES AND THE DETERMINATION OF DROPLET SIZE

The determination of particle size is one of the peculiarly difficult and sensitive phases of any research or development project involving particulate matter. It is sensitive because the degree to which the particle trajectory departs from the gaseous streamline varies as the square of the particle radius. Consequently, an error of a factor of three in particle radius (an error which is very likely from most approaches) will change the departure of particle trajectories from streamlines by a factor of nine. In terms of the present problem, this may change the number rate of impingement by a factor of nine. Conversely, since the impingement rate has such a sensitive dependence upon particle size, measurement of particle impingement becomes a correspondingly sensitive measure of particle size. It is a technique related to this observation that is explored for estimating the average free stream droplet size downstream of a supersonic nozzle.

Consider a wedge of semivertex angle α as shown in Figure 6-1 and placed symmetrically in a supersonic flow of Mach number $M > 1$. When the gas alone is present, an oblique shock wave is attached to the leading edge (for M sufficiently large) making an angle ϵ with the surface of the wedge.

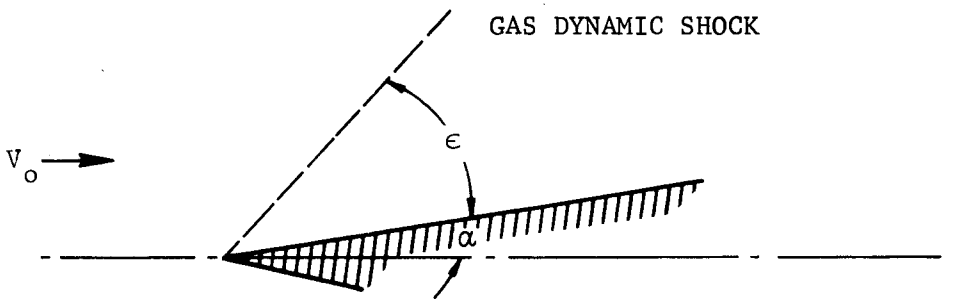

FIGURE 6-1. WEDGE IN SUPERSONIC FLOW

Downstream of the shock, the gas moves, except for motion caused by the forces imparted by the particles, parallel with the wedge surface. For liquid or solid particles of large sizes compared with molecular dimensions, the velocity of the particles does not change across the shock and, consequently, they retain a velocity component $V_o \sin \alpha$ normal to the surface immediately downstream of the shock. If we denote by u the particle velocity normal to the wedge surface, then this component of the particle velocity satisfies the differential equation.

$$m \frac{du}{dt} = - \rho \frac{u^2}{2} C_d \pi \sigma^2 \tag{6.1}$$

where m is the particle mass, σ the particle radius, ρ the constant density downstream of the shock wave, and C_d the droplet drag coefficient which is a function of particle Reynolds number and Knudsen number. For the present analysis, C_d will be considered constant. Then Equation (3.1) may be rewritten in the following form:

$$\frac{du}{dt} = - \frac{u^2}{\Lambda} \tag{6.2}$$

where Λ is known as the momentum range (Reference 6) indicating that the motion described by Equation (6.1) takes place with a length scale. The momentum range is defined by the following equation:

$$\Lambda = \frac{8}{3C_d} \frac{\rho_\ell}{\rho} \sigma \tag{6.3}$$

where ρ_ℓ is the density of the liquid comprising the droplets. Physically, the length Λ represents the distance which the particle will slip relative to the gas while its relative velocity is reduced to half its initial relative velocity.

If the initial velocity of the droplet relative to the gas is u_o, the velocity u at any time is obtained by integrating Equation (6.2) with the boundary conditions

$$t = 0 \qquad u = u_o$$

$$t = t \qquad u = u$$

resulting in the following equation:

$$\frac{u}{u_o} = \frac{u}{V_o \sin \alpha} = \frac{1}{1 + \dfrac{V_o \sin \alpha \cdot t}{\Lambda}} \tag{6.4}$$

During the same time, the droplet is moving tangentially to the wedge with the approximate velocity $V_o \cos \alpha$ and the distance covered is approximately $V_o \cdot t \cdot \cos \alpha$ where t is measured from the time the droplet crosses the shock wave. The trajectories may be drawn quite easily for droplets that enter the shock at various distances above the centerline of the wedge, and a schematic diagram of this situation is shown in Figure 6-2.

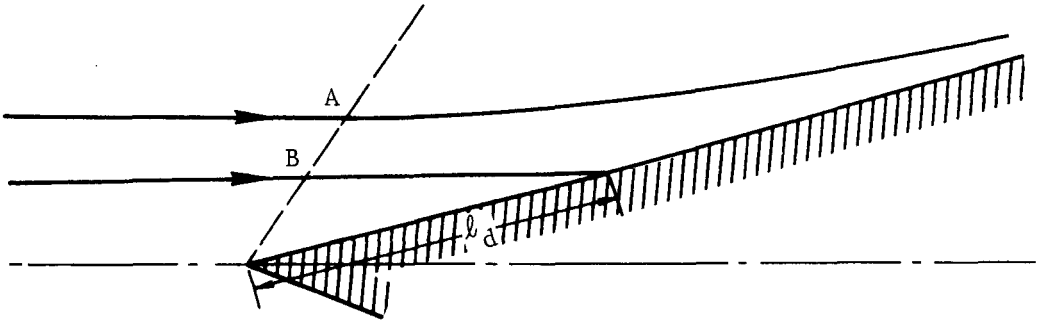

FIGURE 6-2. TWO-PHASE FLOW EFFECT ON WEDGE

The particle entering the shock at point A is at such a distance from the wedge that it eventually moves tangentially to the surface and, in particular, never hits the surface with any significant momentum. The particle moving closer to the wedge centerline and entering the shock at point B does impart some momentum to the wedge surface and, in fact, is capable of doing some local structural damage if the wedge material is appropriate. The particle impacts will produce damage when the velocity component normal to the wedge surface is equal to or larger than a known critical velocity u*. According to Equation (6.4), the condition that the particle will damage the surface is then that

$$\frac{u^*}{V_o \sin} \geq \frac{1}{1 + \dfrac{V_o \sin \alpha \cdot t}{\Lambda}} \tag{6.5}$$

or ℓ_d is the distance measured along the wedge from the leading edge over which damage is done; this length may be written

$$\frac{\ell_d}{\Lambda} = \left(\frac{V_o}{u^*} - \frac{1}{\sin \alpha} \right) \cos \alpha \tag{6.6}$$

Combining Equations (6.3) and (6.6), the desired relationship between damage length and droplet size is obtained:

$$\ell_d/\sigma = 8/3 \cos \alpha \frac{\rho_\ell}{\rho} \frac{1}{C_d} \left(\frac{V_o}{u^*} - \frac{1}{\sin \alpha} \right) \qquad (6.7)$$

Equation (6.7) indicates that in a given experiment, the observed value of ℓ_d is proportional to the droplet radius, or in other words, the damage length increases directly with droplet radius. Consequently, the observed damage on a wedge of this type can be interpreted to give a relatively accurate measure of the particle size. Note that the linear dependence of ℓ_d on σ ensures a quite reasonable accuracy of measurement probably with greater accuracy than warranted in view of the usual lack of reproducibility of condensation phenomena.

It is clear, however, there exists a whole spectrum of particle sizes rather than a cloud of particles having a single radius. In this case, the result obtained, that in the visible end of damage, will give an average radius weighted according to that size giving the maximum damage. This is the appropriate mean value in dealing with a problem, such as the present one, where the measurement of surface damage is the aim of the investigation.

6.2 SELECTION OF TEST CONDITIONS

6.2.1 THERMODYNAMIC PROCESSES

Figure 6-3 identifies the thermodynamic expansion processes for the specified seven test runs. All processes begin with saturated vapor and expand to various quantities, covering the specified quality range $0.80 < x < 0.95$. The low qualities and high enthalpy changes are of interest for the design of supersonic potassium impulse turbines. The selection of the indicated processes was based upon the following considerations:

(1) Low exhaust pressure to increase physical dimensions of the nozzle-wedge specimen.

(2) Large enthalpy change to ensure supersonic flow.

(3) Sufficient coverage of specified saturation temperature regime $1000°F < T < 1500°F$ and nozzle exhaust quality range $0.80 < x < 0.95$.

Processes 2, 3, and 4 all have the same throat, but are cut off at various area ratios, thus allowing determination of droplet size as a function of varying quality, but with identical inlet conditions. Processes 5 and 6 have the same area ratios and qualities but different nozzle lengths in order to identify the effect of varying expansion velocity on droplet size.

Processes 1 and 3, and 2, 5, and 6 end at the same respective qualities and are designed to observe the effect of varying saturation inlet conditions on droplet size. Process 7 is identical to Process 1 so that the reproducibility and accuracy of the selected test method may be checked.

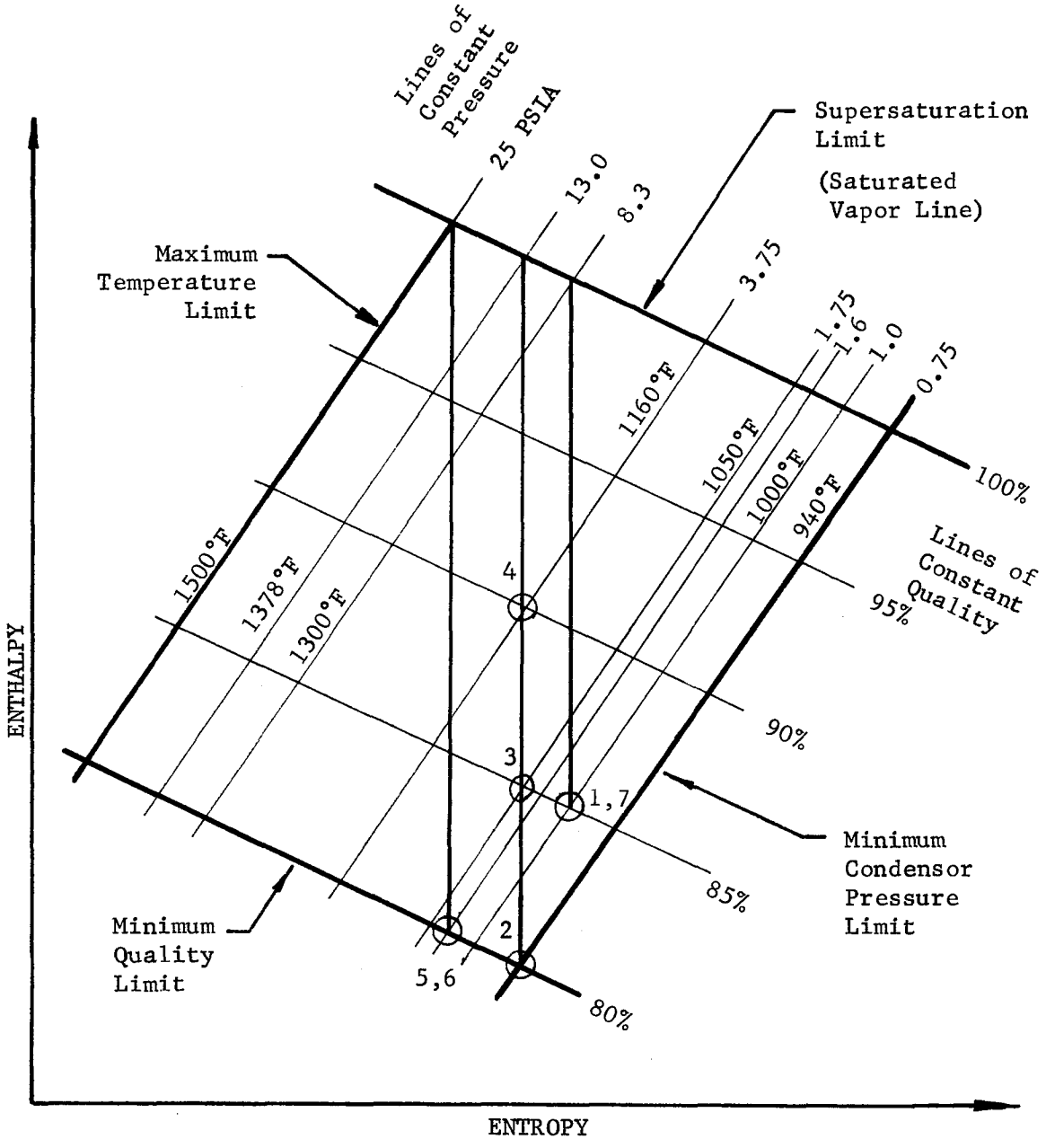

F05596 U

FIGURE 6-3. MOLLIER CHART FOR SELECTED THERMODYNAMIC PROCESSES

6.2.2 NOZZLE AND WEDGE DESIGN

With the thermodynamic processes defined, areas of the throat and exit were defined by two forms of the continuity equation:

$$A_* = \frac{\dot{W}\sqrt{\frac{\bar{v}_t}{P_t g}}}{n^{1/2}\left(\frac{2}{n+1}\right)^{\frac{n+1}{2(n-1)}}} \tag{6.8}$$

$$A_e = \frac{\bar{v}_e \dot{W} X_e}{\sqrt{2gJ\Delta H_e}} \tag{6.9}$$

Equation (6.8) is the polytropic mass flow equation for choked flow which was used to calculate the throat areas. An average polytropic exponent of n = 1.4 was used, which is in agreement with the recent results of Reference 13 while the specific volumes, $\bar{v}_t$ and $\bar{v}_e$, were taken from the thermodynamic tables of Reference 14.

Equation (6.9) is the mass flow equation $\dot{W} = \rho AV$, assuming equilibrium flow, with specific volume (density) obtained from Reference 6 and velocity calculated from the energy $V = \sqrt{2gJ\Delta H}$. Equation (6.9) compares favorably with exit areas as obtained from Reference 15.

For the present experiment, conical nozzles were selected. The individual nozzle length was calculated by selecting a mean expansion velocity $\dot{P}$, which identifies each nozzle. The mean expansion velocity $\dot{P}$ is related with the thermodynamic processes and the nozzle length by the following equation developed by Reference 16.

$$\frac{\dot{P}\ell}{\sqrt{2gJ\Delta h}} = \frac{2\gamma}{\gamma-1} \ln \left[\frac{1 + \sqrt{1-\left(\frac{P}{P_o}\right)^{\frac{\gamma-1}{\gamma}}}}{1 + \sqrt{\frac{\gamma-1}{\gamma+1}}} \right] - \frac{\gamma}{\gamma-1} \ln \left[\frac{\gamma+1}{2} \left(\frac{P}{P_o}\right)^{\frac{\gamma-1}{\gamma}} \right] - \frac{2\gamma}{\gamma-1} \sqrt{1-\left(\frac{P}{P_o}\right)^{\frac{\gamma-1}{\gamma}}} + \frac{2\gamma}{\gamma-1} \sqrt{\frac{\gamma-1}{\gamma+1}} \tag{6.10}$$

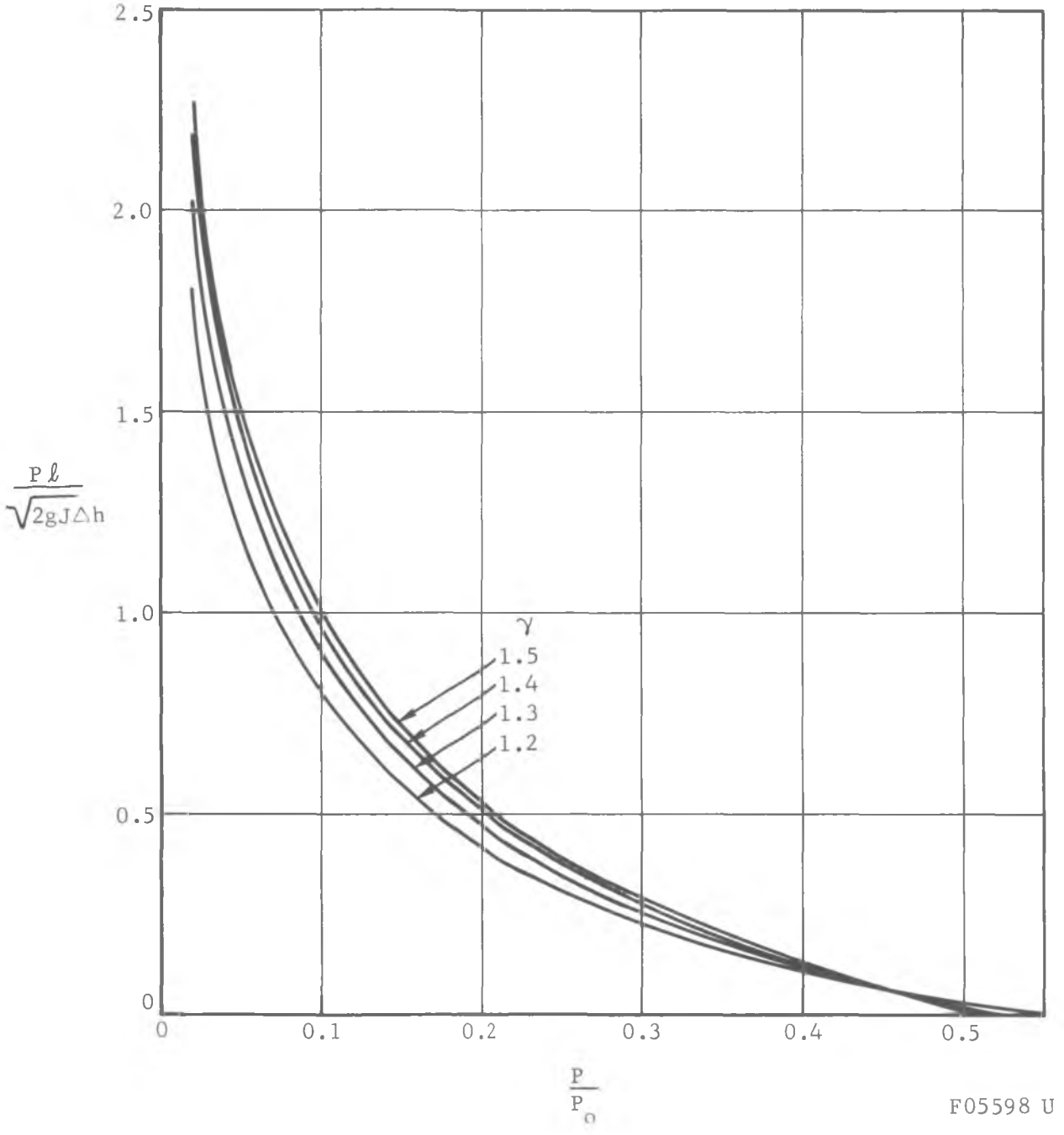

FIGURE 6-4. NONDIMENSIONAL CHARACTERISTIC EXPANSION VELOCITY AS A FUNCTION OF γ, THE RATIO OF SPECIFIC HEATS

Equation 6.10 has been evaluated numerically and is presented in Figure 6-4 where the dimensionless expansion velocity-nozzle length parameter is plotted as a function of the expansion velocity $\dot{P}$ and the ratio of the specific heats, γ. While Reference 17 conducted its experiments with nozzles having a very low average expansion velocity of $\dot{P}$ = 6830, the present experiment investigates condensation effects for $\dot{P}$ = 40,000 to 160,000. Reference 1 concluded that the free stream droplet size depends strongly on the expansion velocity, whereby the droplet size should decrease with increasing values of $\dot{P}$.

Selection of the wedges was based on Equation (6.7) and the wedge angle required to maintain an attached flow on the wedge. A plot of Equation (6.7) with a selected drag coefficient is shown in Figure 6-5 for impingement on a nickel surface with a nominal u* = 420 ft/sec. The wedge angles are noted on this figure and were chosen to cover a large change in damage length in the event that some of the parameters were incorrectly determined.

Nickel was chosen over seven other candidate plating materials since it was relatively soft and noncorrosive in a potassium environment. The nickel was plated on highly polished stainless steel wedges.

The results of the calculations for nozzle sizing and chosen values of $\dot{P}$, length of nozzle, and wedge angles used are shown on Table IV.

The minimum impingement velocity, u*, was calculated from References 18 and 19; i.e.,

$$u^* = \frac{19E' (Z+Z')}{\left(\rho c' Z'^3\right)^{1/2}} \tag{6.11}$$

The most significant parameter to this calculation was the dynamic compressive yield strength of the target material. Unfortunately, it is not known for most materials especially at elevated temperatures. Therefore, it was predicted by first obtaining the static tensile yield strengths for all metals of interest, and, based on known metals behavior, the static tensile yield strength was assumed equal to the compressive yield strength. Static tensile yield at 1500°F was then obtained from high temperature material properties and the relationship between room temperature static and dynamic properties for iron were assumed to hold at elevated temperatures for all metals. This relationship (from Reference 20) is

$$\frac{S}{Y} = 5.98 - 2.42 \log_{10} Y. \tag{6.12}$$

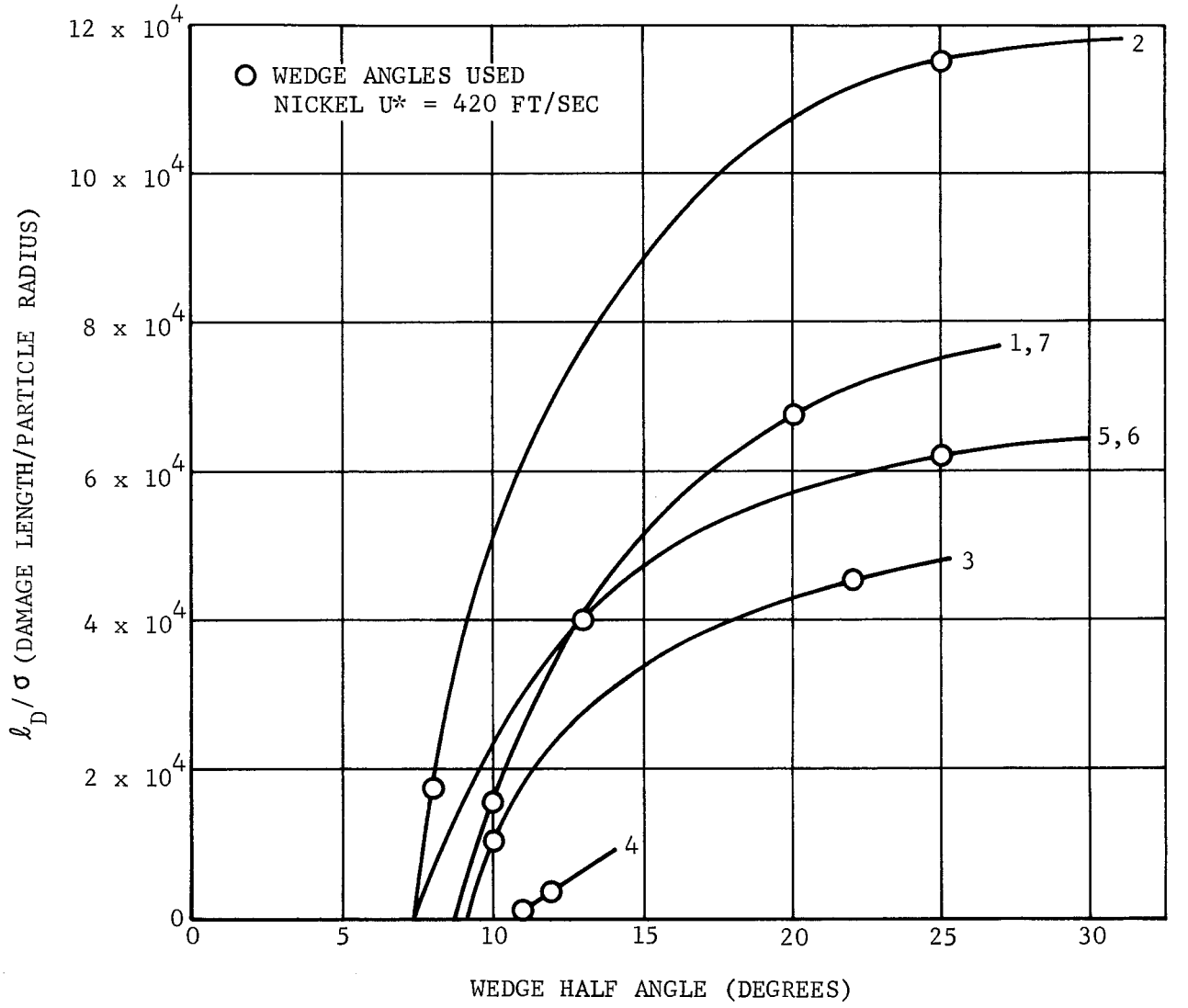

FIGURE 6-5. NONDIMENSIONAL DAMAGE LENGTHS FOR NICKEL IMPINGEMENT

Table IV - Summary of First Six Tests With Accompanying Dimensions

Test No.	Length from Throat to Exit (in.)	Throat Diameter (in.)	Exit Diameter (in.)	Half Wedge Angles (deg)	$\dot{P}_o$ (1/sec)
1	0.97	0.293	0.405	10,20	40,000
2	1.617	0.236	0.405	8,25	40,000
3	0.898	0.236	0.325	10,22	40,000
4	0.357	0.236	0.261	11,12	40,000
5	0.393	0.1722	0.300	13,25	160,000
6	0.572	0.1722	0.300	13,25	40,000
7	Same as 1				

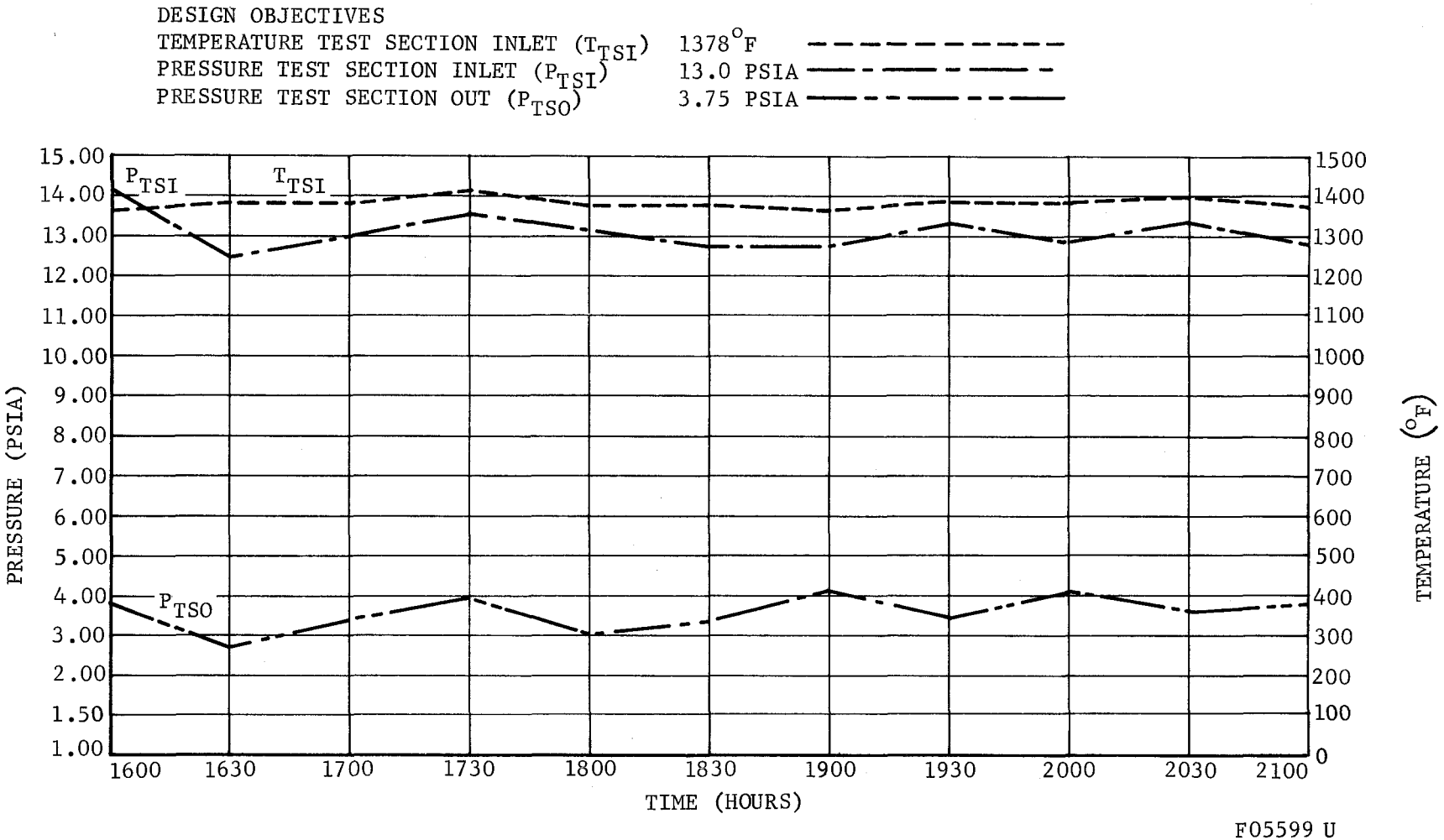

F05599 U

FIGURE 6-6. TYPICAL TEMPERATURE-PRESSURE HISTORY OF TEST 4

6.3. TEST PROGRAM

The test program consisted of seven short duration runs . Table V presents a summary of the average test conditions experienced by each nozzle-wedge specimen. Figure 6-6 shows a typical temperature and pressure history as a function of operating time. In this plot, inlet and exit pressures together with the stagnation temperature are shown. It is significant to note that very steady conditions were achieved for most of the test runs.

Table V. Summary of Average Test Parameters

Wedge No.	Duration of Test (hrs)	Inlet Temperature (^{o}F)	Inlet Pressure (psia)	Downstream Pressure (psia)
1	4.0	1250	7.2	1.0
2	4.5	1380	12.5	0.75
3	4.0	1375	13.5	1.75
4	5.0	1380	13.5	3.20
5	3.5	1600	19.5	1.50
6	3.5	1440	18.3	1.1
7 (same geometry as 1)	4.0	1270	7.8	1.0

6.3.1 TEST OPERATIONS

The seven tests that were accomplished were short, ranging from 3.5 to 6.0 hours at design conditions. A nominal time of 5 hours was required to establish operating conditions for each test. During this warmup period, nucleate boiling was established by having the hot fingers lead

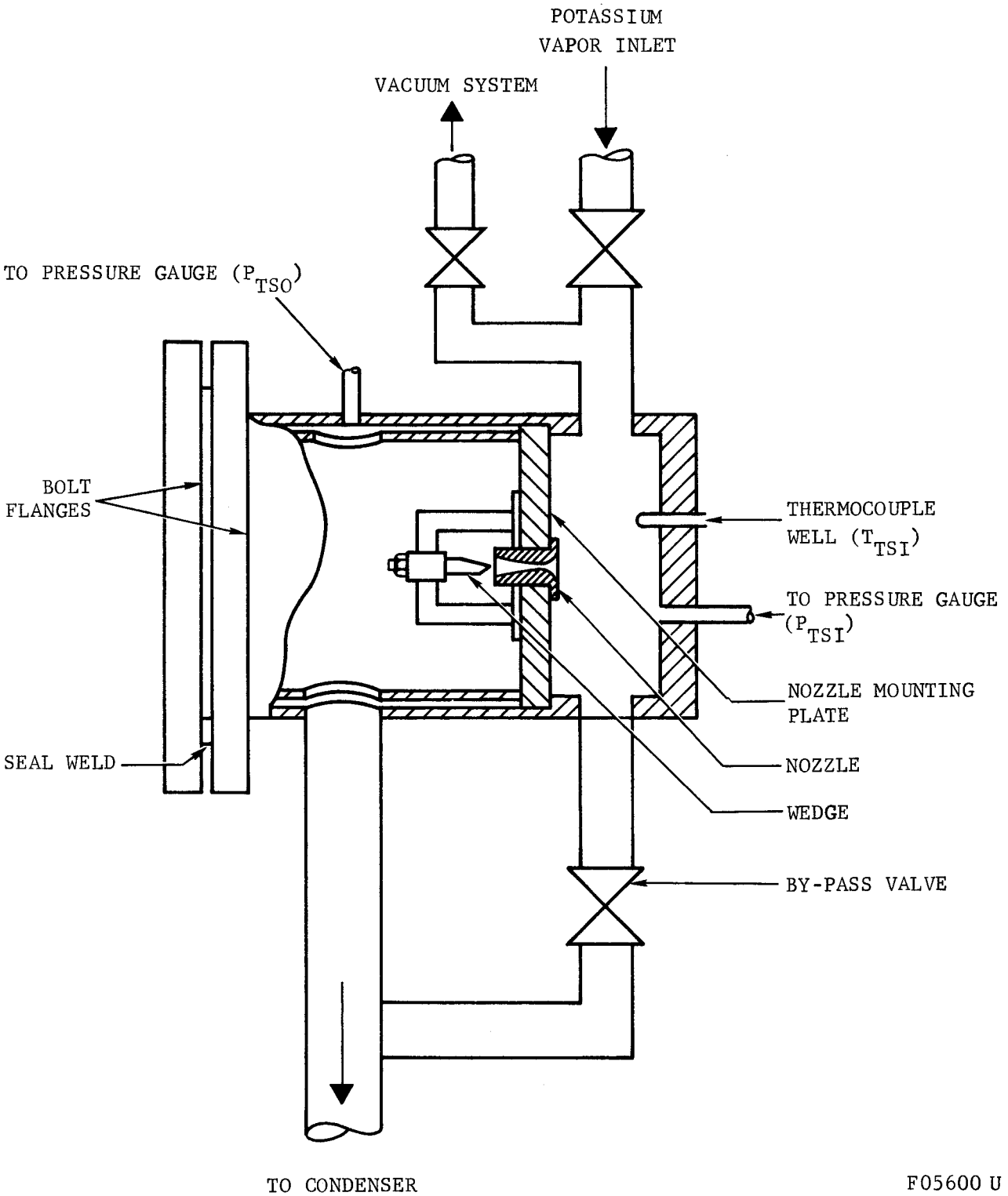

FIGURE 6-7. SCHEMATIC OF POTASSIUM LOOP TEST SECTION

the bulk potassium temperature of the boiler by 200°F. The boiler input power was then uniformly increased and the drier heaters increased until 5 to 10°F superheat was achieved. The potassium flow was controlled by use of the boiler inlet valve. As illustrated in Figure 6-7, vapor flow was throttled across the test section inlet valve and exhausted through the test section bypass valve.

As design conditions were approached, the bypass valve was slowly closed and the inlet valve opened, subjecting the chamber upstream of the nozzle to the higher potassium vapor pressure. The vapor then expanded through the nozzle and impinged upon the wedge section under test. Pressure and temperature upstream of the test section were maintained by manual manipulation of the boiler heaters. Downstream pressure (condenser pressure) was controlled by manipulating condenser level and flow of coolant air.

After each test, the loop's potassium inventory was pumped into the boiler which was then cooled. The test section and condenser was isolated from the remainder of the loop by closing appropriate valves, heated, and vacuum distilled for a period of 48 hours. This removed all residual potassium and allowed removal of the test specimens with reasonable safety. It also minimized the reaction of potassium with oxygen of the air.

After the test specimen was removed, a new specimen was installed and the seal plate welded in place. The loop was then evacuated and backfilled with argon several times prior to heating. The final evacuation was performed after the potassium was melted and raised to a temperature of 600°F.

6.4 ANALYSIS OF TEST RESULTS

Figures 6-8 through 6-11 present four of the high wedge angle specimens subjected to the selected potassium test condition. In addition to the damage caused by particle impingement, there was evidence that a liquid potassium film existed over the surface of the wedge in some of the experiments. This accounts for the fact that impingement damage was less clearly defined for some wedges.

Comparison of the high wedge angle result with the low angle wedges shows that the condensate droplets were of such a size distribution that primarily the high angle side presents sufficient accurate data. The most spectacular result is presented by the damage pattern of Figure 6-9.

In order to calculate the resulting droplet sizes, the average temperature and pressure conditions were utilized. The average test conditions were summarized in Table V , while Table VI presents the summary of the observed damage lengths.

Based on this information, the vapor state conditions downstream of the oblique shock have been calculated and the basic flow parameters such as Reynolds and Knudsen numbers have been determined, and the first approximation of particle size was obtained from Equation 6.7 with constant drag coefficient. The drag coefficient was calculated by the relation:

$$C_d = C_{do} f_{c_d} \tag{6.13}$$

where C_{do} is found as a function of Reynolds number from Reference 21 and f_{c_d} is a correction depending on the Knudsen number taken from Reference 1.

By means of successive iteration, it was then possible to determine accurately the condensate sizes in accordance with the damage length and the selected test condition. The result of the test data analysis is presented in Figure 6-12 where the condensate particle diameter is presented as a function of the nozzle vapor exit quality. No effect of temperature on size was noted.

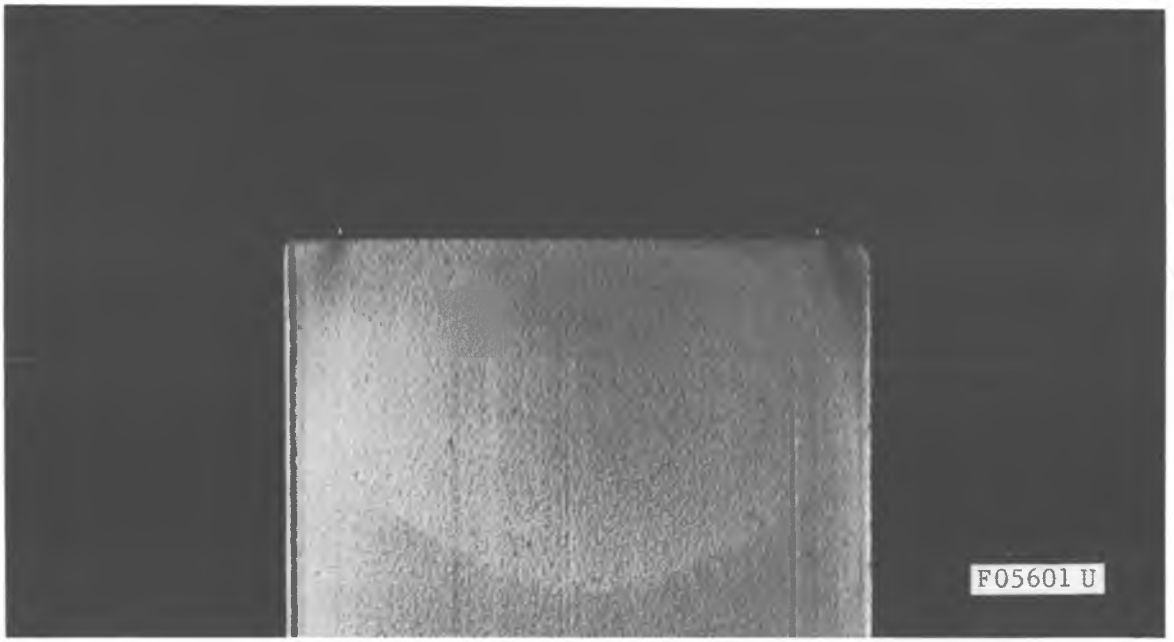

FIGURE 6-8. PHOTOGRAPH OF TEST WEDGE 1, 20° SIDE

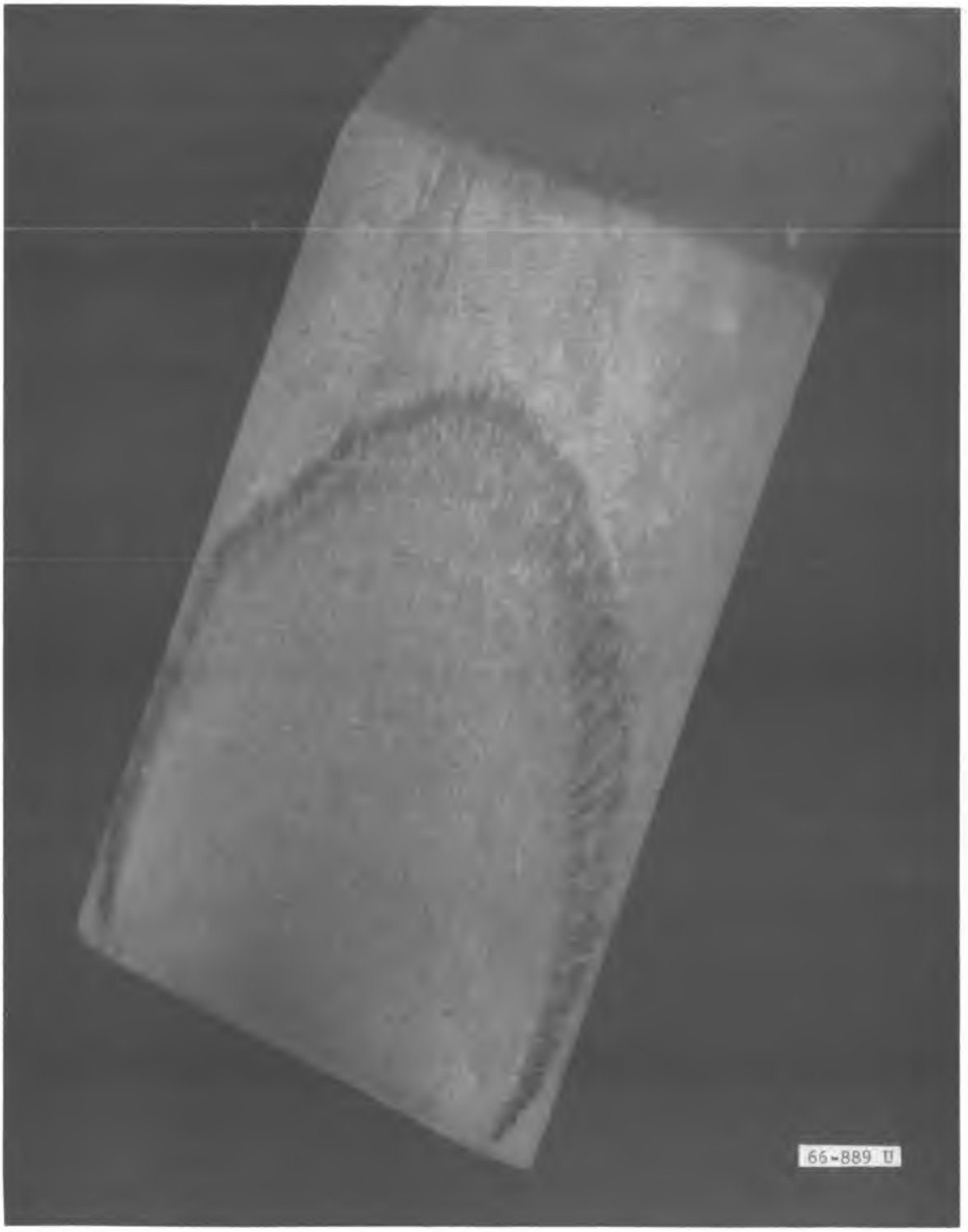

FIGURE 6-9. PHOTOGRAPH OF TEST WEDGE 2, 25° SIDE

FIGURE 6-10. PHOTOGRAPH OF TEST WEDGE 4, 120° SIDE

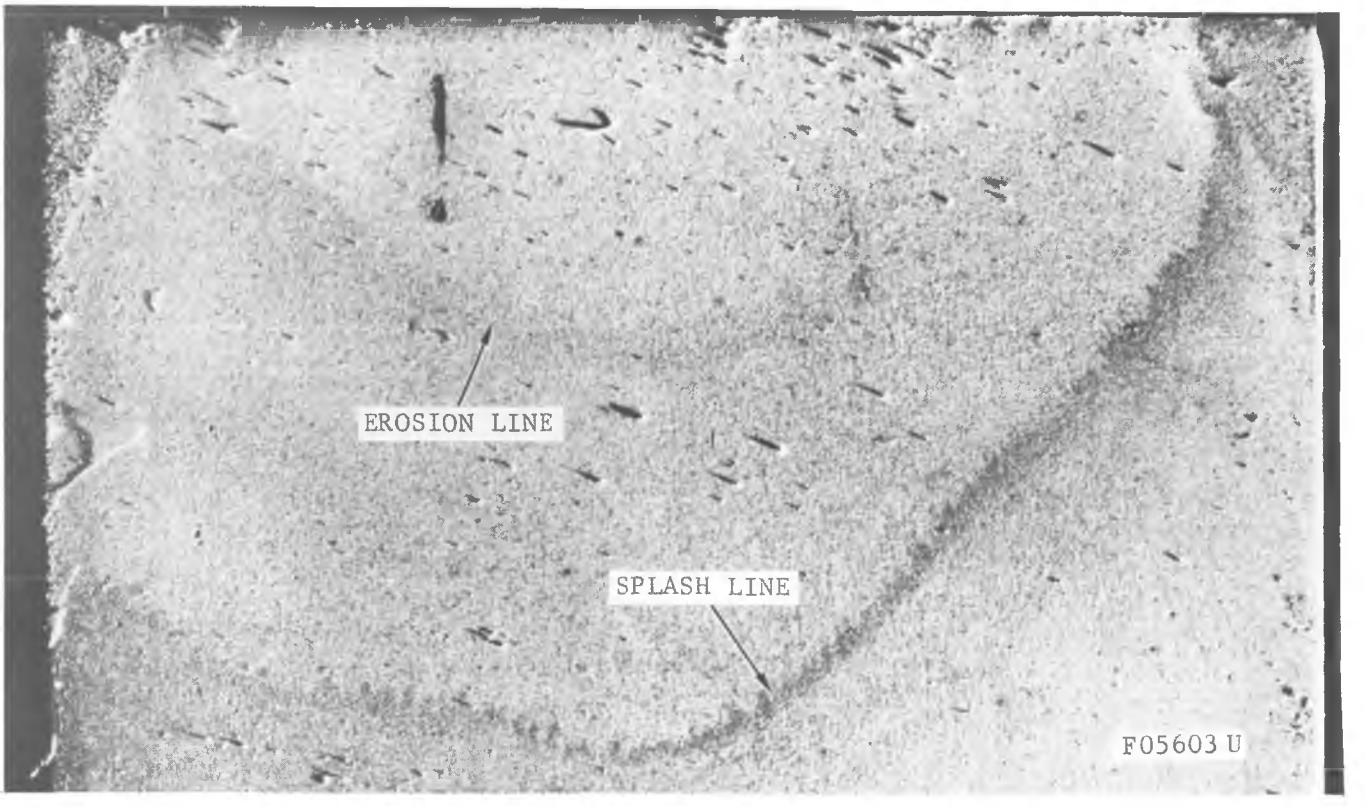

FIGURE 6-11. PHOTOGRAPH OF TEST WEDGE 7, 20° SIDE

Table VI - Test Results of Observed Damage to Wedges and Stagnation Conditions

Test	Erosion Lengths (mm) High Angle Side	Erosion Lengths (mm) Low Angle Side	Comments
1	3.3	0.20	Hardly visible
2	10.6	hardly visible	Most clear result
3	(7.6)	(0.12)	Not clear
4	0.11	0.079	Very clear result
5	5.66	4.56	Heat transfer region. Specimen fouled badly with KO_3. Uniform KO_3 coating in nozzle 0.030 inch thick.
6	6.5	2.55	Similar result as #2 only not as clear
7	3.3	hardly visible	Similar result as #1

While the results of Test 3 are inconclusive, all the other six tests follow the expected trend of decreasing particle size with increasing values of quality. The excellent correlation of all the test data shown in Figure 6-5 presents a significant result which will provide a sound basis for the future analysis of actual potassium impulse type of turbines. It is interesting to note that the free stream particle size is much larger than predicted by available condensation theories. For example, the result shows clearly that the free stream particle size is actually an order of magnitude larger than the particle size predicted by theory.[22,23] It is possible that the unusually large droplet size can be accounted for by collision and agglomeration.[24]

Inspection of the test data in Figure 6-12 indicates that the maximum spread of the test data is less than a factor of two for the 85 percent quality point which is a remarkable result when one considers micron particles and the complex condensation process. The close agreement of Tests 1 and 7, together with the close agreement of Tests 2 and 6, are also proof of the reproducibility and accuracy of the experimental test results obtained by the present program. Although Tests 5 and 6 were designed to

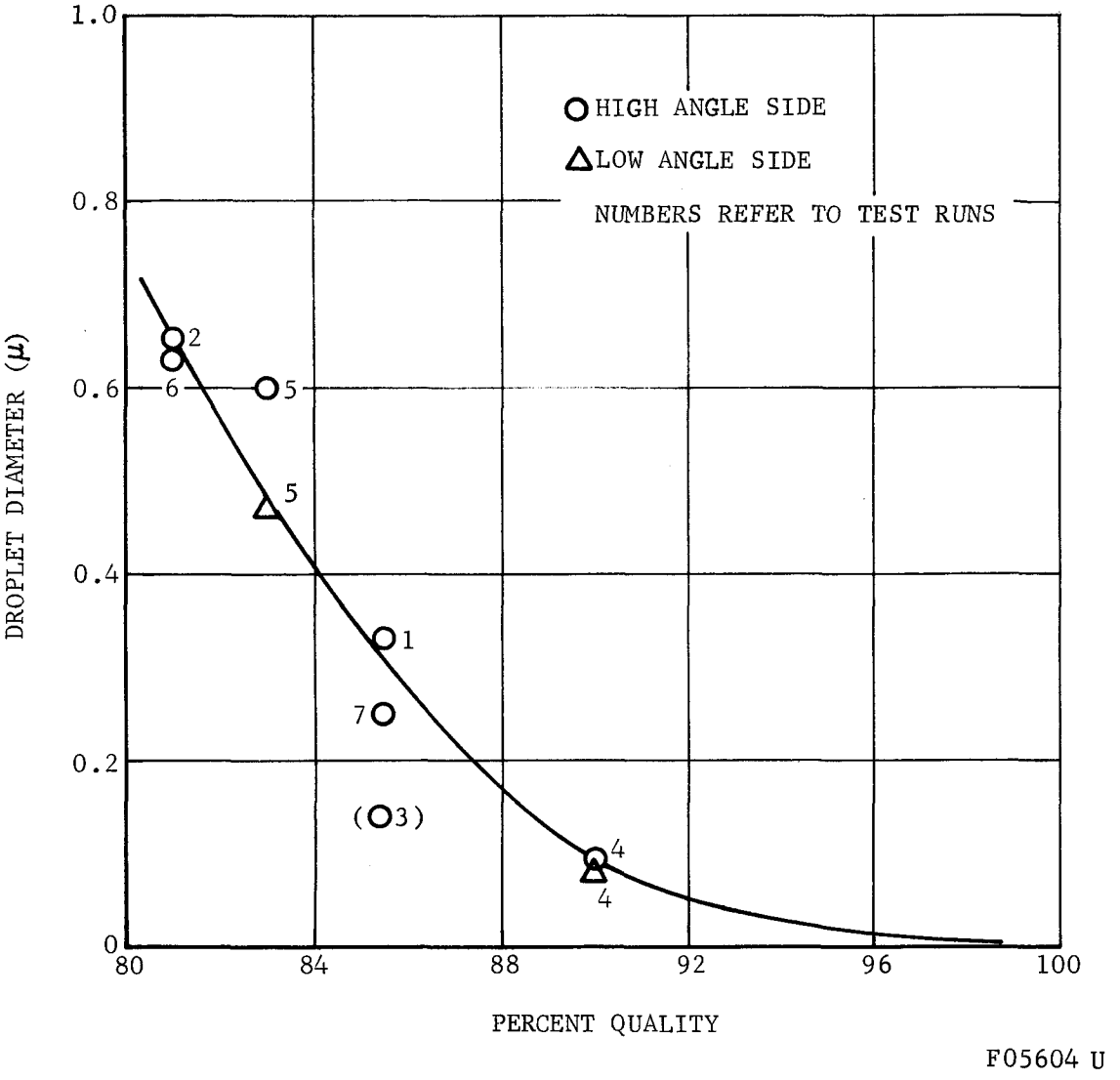

FIGURE 6-12. CORRELATION OF DROPLET SIZE AND VAPOR QUALITY FOR POTASSIUM FLOW

investigate the effect of length of nozzle (i.e., P) the runs could not be compared since stagnation conditions were not identical. Tests 5 and 6, however, did result in similar measured droplet sizes.

Figure 6-13 shows a plot of minimum impingement velocity required to cause erosion to the nickel plated stainless steel wedges. The curve should be most accurate in the 1000 to 1300°F temperature range where experimental data were used while the room temperature value was known from the literature. Using Equation 4.3, this experimental information allows determination of the dynamic yield strength of nickel as a function of temperature. The latter is presently not available in the literature.

Figure 6-14 is a photograph of the inlet of Test Nozzle 2 with the beginning of a deposition occurring at a subsonic value of $A/A^* \simeq 2$. Similar deposition and/or erosion patterns were observed on most test nozzle inlets. This observation leads to the conclusion that condensation occurred upstream of the nozzle throat and, therefore, the nozzle design procedure utilizing n = 1.4 was correct for the selected thermodynamic processes.

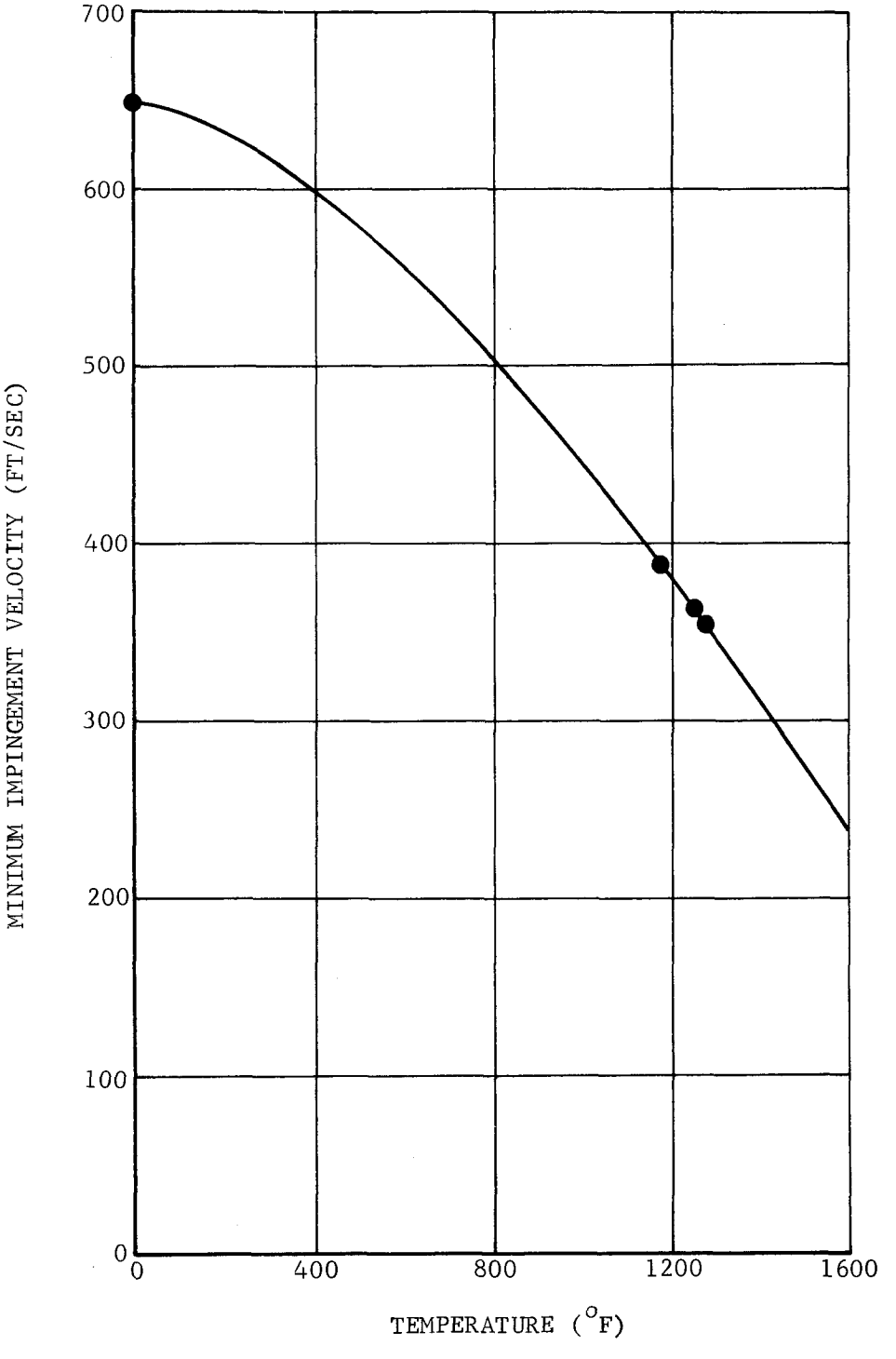

FIGURE 6-13. MINIMUM IMPINGEMENT VELOCITY REQUIRED TO CAUSE DAMAGE TO A NICKEL SURFACE AS A FUNCTION OF TEMPERATURE (BASED ON EXPERIMENTAL RESULTS OF LIQUID POTASSIUM IMPINGING ON NICKEL PLATED STAINLESS STEEL WEDGES)

FIGURE 6-14. PHOTOGRAPH OF TEST NOZZLE 2 SHOWING DEPOSITION PATTERN ON SUBSONIC PORTION OF NOZZLE

SECTION 7

TURBINE INVESTIGATION

The portion of the investigation described in this section was an effort to further the knowledge of turbine blade erosion by running a turbine wheel containing several different blade configurations for a significant length of time in a potassium loop under conditions for which the condensate droplet size could be established. Such basic parameters as droplet size, orientation and absolute value of the impingement vector with respect to the turbine blading, thermodynamic cycle state point conditions, condensation rate, and turbine materials might limit the application of the liquid metal dynamic power plant due to appreciable turbine performance losses or progressive blade erosion from liquid droplet impingement. A preliminary appraisal of the limiting tip speed of a partial admission, single-stage, supersonic, potassium turbine is presented and discussed.

7.1 FLUID COLLECTION ON BLADES

The mechanism of collecting liquid on turbine blades, as contrasted with the flow of these liquid layers once they are deposited, may be divided roughly into two parts. The first part, near the leading edge, takes place as a result of the vapor turning about the leading edge with a radius of curvature of the same order as that of the leading edge. The second part, along the concave blade surface, takes place as a result of the vapor turning through the blade row. In estimating the amount of liquid collected, therefore, it is relevant to investigate the transport of liquid droplets in the vapor as the vapor turns through an arc of specified radius.

Consider the two-dimensional flow in cylindrical polar coordinates r, θ where u and v are the radial and tangential components of the gas velocity and u_p, v_p are the corresponding components of the particle velocity. If the phase change rate is small in the regions we are concerned with, then the appropriate equations of continuity and motion are

$$\frac{1}{r}\frac{\partial(ru)}{\partial r} + \frac{1}{r}\frac{\partial v}{\partial \theta} = o \tag{7.1}$$

$$\rho u \frac{\partial u}{\partial r} + \rho v \frac{\partial u}{r\partial \theta} - \frac{\rho v^2}{r} = -\frac{\partial p}{\partial r} + \frac{\rho_p U_o (u_p - u)}{\lambda_v} \tag{7.2}$$

$$\rho u \frac{\partial v}{\partial r} + \rho v \frac{\partial v}{r\partial \theta} + \frac{\rho uv}{r} = -\frac{1}{r}\frac{\partial p}{\partial \theta} + \frac{\rho_p U_o (v_p - v)}{\lambda_v} \tag{7.3}$$

for the gas phase and

$$\frac{1}{r}\frac{\rho_p r u_p \partial(\rho_p r_p)}{\partial r} + \frac{1}{r}\frac{\rho_p v_p \partial v_p}{\partial \theta} = 0 \tag{7.4}$$

$$\rho_p u_p \frac{\partial u_p}{\partial r} + \rho_p v_p \frac{\partial u_p}{r\partial\theta} - \frac{\rho_p v_p^2}{r} = -\frac{\rho_p u_o}{\lambda_v}(u_p - u) \tag{7.5}$$

$$\rho_p u_p \frac{\partial v_p}{\partial r} + \rho_p v_p \frac{\partial v_p}{r\partial\theta} + \frac{\rho_p u_p v_p}{r} = -\frac{\rho_p u_o}{\lambda_v}(v_p - v) \tag{7.6}$$

for the liquid phase. For this consideration, it will be sufficient to consider the vapor as incompressible. The unusual terms appearing on the right sides of the equations of motion are the mutual forces exerted between the two phases as a result of the motion of small liquid droplets with respect to the vapor. The characteristic velocity u_o may be taken as the relative velocity of vapor and blade. The characteristic length λ_v is defined.

$$\lambda_v = \frac{m u_o}{6\pi\sigma\mu} \tag{7.7}$$

where m is the constant mass of a single liquid droplet of radius σ. When λ_v is small in comparison with other characteristic lengths of the problem, which is usually true here for the very small droplets that grow in the turbine nozzle, then the flow problem may be treated by a perturbation analysis. This process, discussed in general in Reference 6, is based on the fact that the actual flow field is rather near to that flow field that would occur if the droplets did not move with respect to the vapor. Let this flow field be represented by the quantities $u^{(o)}$, $v^{(o)}$, $\rho^{(o)}$, and $\rho_p{}^{(o)}$ = constant, where the velocity component $u^{(o)}$, $v^{(o)}$ are the same for both phases. Strictly speaking, this is a limiting flow field that is approached as $\lambda_v \longrightarrow$ o and, thus, the particle forces that appear on the right sides of the equations are not zero but approach finite values as the velocity equilibration length $\lambda_v \longrightarrow$ o. It is appropriate, therefore, to expand all quantities in perturbation series expressed as power series expansion in λ_v. Therefore,

$$u = u^{(o)} + \lambda_v u^{(1)} + \lambda_v{}^2 u^{(2)} + \ldots \tag{7.8}$$

$$v = v^{(o)} + \lambda_v v^{(1)} + \lambda_v{}^2 v^{(2)} + \ldots \tag{7.9}$$

$$p = p^{(o)} + \lambda_v p^{(1)} + \lambda_v^2 p^{(2)} + \ldots \qquad 7.10$$

$$u_p = u^{(o)} + \lambda_v u_p^{(1)} + \lambda_v^2 u_p^{(2)} + \ldots \qquad 7.11$$

$$v_p = v^{(o)} + \lambda_v v_p^{(1)} + \lambda_v^2 v_p^{(2)} + \ldots \qquad 7.12$$

$$\rho_p = \eta\rho + \lambda_v \rho_p^{(1)} + \lambda_v^2 \rho_p^{(2)} + \ldots \qquad 7.13$$

and it will be quite sufficient for the present analysis to consider only the first order perturbation quantities.

Without reproducing the details of the mathematical analysis, it may be shown that the first order slip velocity of the liquid particles toward the surface may be written

$$u_p^{(1)} = \frac{v^{(o)^2}}{Ru_o} \qquad 7.14$$

where R is the radius of curvature of the streamline near the surface. Moreover, for the flow situations of interest in this problem, the value of $v^{(o)}$ is very nearly the relative vapor-turbine blade velocity u_o. The local velocity of particle flow into the surface of the blade is, therefore,

$$v_\ell = \lambda_v u_o / R \qquad 7.15$$

and the mass flow of liquid to the surface per unit area is $m_\ell = \rho_p^{(o)} v_\ell$. Substituting for the velocity equilibration length from Equation (7.7), we obtain the result

$$v_\ell = \frac{m u_o}{6\pi\sigma\mu} \frac{u_o}{R}$$

$$= \frac{2}{9} \left(\frac{\rho_\ell \sigma u_o}{\mu}\right) u_o \frac{\sigma}{R} \qquad 7.16$$

where ρ_ℓ is the mass density of the liquid phase.

Now, if all quantities in the result, particularly the radius of curvature R, remain constant while the vapor turns through an angle of θ radians, then the total mass flux to the surface as the result of this process is

$$M_\ell \cdot R \cdot \theta = \frac{2}{9} \frac{\rho u_o \sigma}{\mu} \cdot \eta \rho_\ell u_o \sigma \theta \qquad 7.17$$

where the result gives the total mass flow of liquid to the blade surface per unit length of blade. The points of special interest are that this mass flow varies as the square of the droplet radius, as the square of the vapor velocity relative to the blade, and directly as the turning angle. Note particularly that it is independent of the blade chord.

7.2 DROPLETS RESULTING FROM LIQUID LAYERS

The liquid that collects upon stationary surfaces by the process described in the last section flows nearly axially and is shed from the trailing edge of the surfaces. On the other hand, the liquid that collects on rotating blades flows in a very nearly radial direction and is shed from the blade trailing edges very close to the tip. This fact may be seen most easily by computing the ratio of the centrifugal force, which moves the liquid film radially, to the gaseous shearing stress, which moves the liquid film tangentially along the blade surface. Now, if ω is the angular velocity of the turbine wheel and R_t is the tip radius, then the total centrifugal force on the liquid film that covers a unit area of the blade surface is of the order

$$\rho_\ell \omega^2 R_t \delta \qquad 7.18$$

where δ is the film thickness. Also, if C_f is the skin friction coefficient between the gas and the liquid film surface, the tangential stress on a unit area of the film surface is just

$$\frac{1}{2} \rho u_o^2 C_f \qquad 7.19$$

where ρ is the gas density and u_o is the relative velocity between gas and moving blade. The ratio of these two quantities, given by Equations 7.18 and 7.19, respectively, then represent the force ratio to be computed. It is not possible, however, to construct a useful ratio until the film thickness is estimated in terms of known quantities. A reasonable estimate may be made by assuming that simple shear flow in the liquid layer, that

the mass flow of liquid in the layer is equal total mass of liquid impinging on a unit length of blade in a unit time, and that the liquid layer leaves the blade at the trailing edge. Then, the shearing stress applied to the surface of the liquid by the gas flow is equal to the shearing stress in the liquid layer itself, and this may be written

$$\frac{1}{2}\rho u_o^2 C_f = \mu_\ell \frac{u_\ell}{\delta} \qquad 7.20$$

where μ_ℓ and u_ℓ are respectively the viscosity of the liquid and the velocity of the liquid at the film surface. It is usual that $u_\ell \ll U_o$. If the mass flow of liquid in the layer per unit length of the blade is denoted M_ℓ, then the relationship between this quantity and the velocity at the film surface is

$$M_\ell = \rho_\ell u_\ell \frac{\delta}{2} \qquad 7.21$$

so that Equation (89) becomes

$$\frac{1}{2}\rho u_o^2 C_f = \frac{2\mu_\ell M_\ell}{\rho_\ell \delta^2} \qquad 7.22$$

But this mass flow rate, M_ℓ, has already been computed as the right side of Equation 7.17, with the consequence that the combination of Equations 7.17 and 7.22 determines the film thickness, δ, in terms of known quantities. Equation 7.22 then gives

$$\frac{1}{2}\rho u_o^2 C_f = \frac{4}{9} \cdot \left(\frac{\mu_\ell}{\rho_\ell \delta}\right)^2 \cdot \eta \rho_\ell u_o \sigma\theta \cdot \left(\frac{\rho u_o \sigma}{\mu}\right) \qquad 7.23$$

Now, from Equations 7.18 and 7.19, the square of the ratio of centrifugal to tangential forces on the liquid film is

$$\zeta^2 = \left(\frac{\rho_\ell \omega^2 R_t}{\frac{1}{2}\rho u_o^2 C_f}\right)^2 \delta^2$$

$$= \left(\frac{2^5}{3^2}\right) \frac{\rho_\ell \omega^4 R_t^2 \mu_\ell}{(\rho u_o^2 C_f)^3} \cdot \eta \rho u_o \sigma\theta \left(\frac{\rho_\ell \sigma u_o}{\mu}\right) \qquad 7.24$$

where the value of δ^2 has been used from the calculation resulting in Equation 7.23. Simplification of this expression leads to the ratio of centrifugal to tangential forces as

$$\zeta = \frac{4\sqrt{2}}{3} \left(\frac{\rho_\ell}{\rho}\right) \sqrt{\frac{\mu_\ell}{\mu}} \left(\frac{\omega R_t}{u_o}\right)^2 \left(\frac{\sigma}{R_t}\right) \sqrt{\frac{\eta\theta}{C_f^3}} \qquad 7.25$$

For reasonable values of the parameters, the value of ζ is in the range of 10^3 to 10^4, indicating that the centrifugal forces on the liquid dominate strongly. As a consequence, it is clear that the liquid layer flows nearly radially on the blades of a rotating stage.

The foregoing results have some significant consequences relating to the formation of liquid droplets from sheets of liquid leaving the blades. For rotating blades, the liquid will leave very close to the blade tip, the droplets will be large, and the radii determined by stability of droplets[10] in a gas flow. The total mass flow contained in these droplets will be essentially equal to the mass flow of liquid impinging on the entire blade. For stationary blades, the liquid will leave rather uniformly along the trailing edge. The droplet size will be determined either by stability criteria, or the thickness of the layer at the trailing edge, whichever is the smaller. In case the thickness δ is the determining criterion, it may be inferred from Equation 7.23 that the droplet diameter is of the order of magnitude of the thickness and, hence, the ratio of the film thickness to the original droplet diameter (2σ) is

$$\frac{\delta}{2\sigma} \approx \sqrt{\frac{\mu_\ell}{\mu} \frac{\eta\theta}{C_f}} \qquad 7.26$$

For reasonable values of the parameters, this droplet radius multiplication ratio is between 10 to 100.

7.3 TEST PROGRAM

The test program consisted of running the supersonic erosion test turbine for 96 continuous hours in the potassium loop with the following average conditions being maintained:

Average turbine inlet pressure:	5.6 psia
Average turbine inlet temperature:	1250°F
Average turbine exhaust pressure:	0.81 psia
Average turbine rotational speed:	17,800 rpm

The purpose of the test program was to determine the extent of turbine blade damage, if any, when a supersonic turbine is run for a relatively long duration in a potassium system and also to determine, if possible, the effects of various parameters such as blade angle, direction and magnitude of the impingement vector, and condensate droplet size.

7.3.1 TEST TURBINE

The turbine wheel used for the erosion test is shown, prior to testing, in Figure 7-1. This impulse type wheel was constructed of TZM material (0.5 percent titanium, 0.1 percent zirconium, balance molybdenum), was 5.0 inches in tip diameter, had 0.290 inch high blades, and blade chords of 0.294 inch. The wheel was divided into eight equal sections in which the blade angles were varied. Corresponding to the labelling in Figure 7-1, Sections II and VIII had blade angles of 25 degrees, Sections I, III, V, and VII had blade angles of 30 degrees, and Sections VI and IV had 35 and 40 degree blade angles, respectively. Figure 7-2 shows a typical turbine blade and nozzle section and velocity triangle which define the terms used herein. Figure 7-3 shows the main components of the test turbine (after the completion of the test); the turbine wheel, shaft, counterbalance wheel, and bearings. The entire test section layout is shown in cross section in Figure 7-4 while Figure 7-5 shows a photograph of the assembled test section.

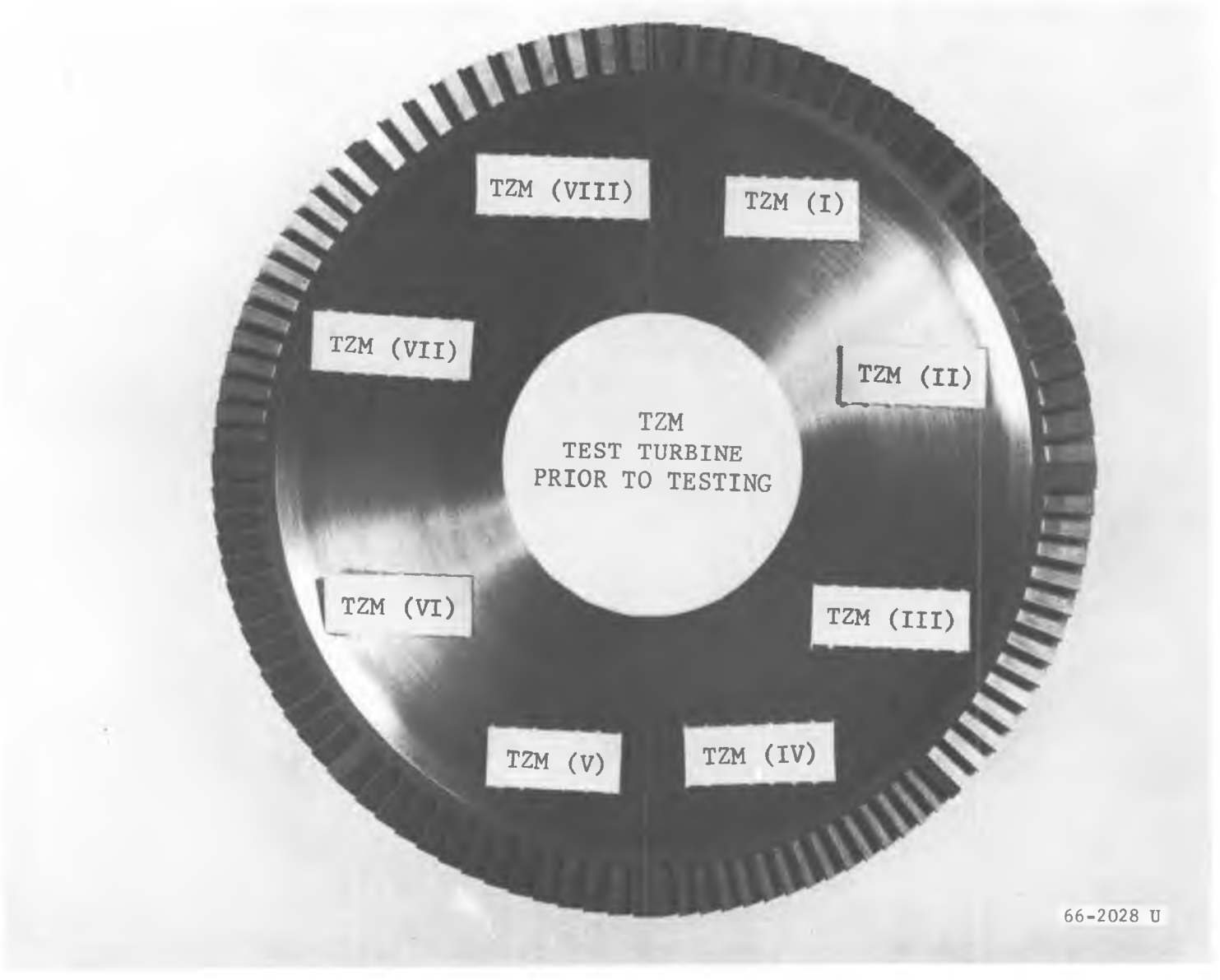

FIGURE 7-1. TEST TURBINE WHEEL PRIOR TO TESTING

α = ABSOLUTE FLOW ANGLE

β_1 = BLADE ANGLE

β_2 = RELATIVE FLOW ANGLE

C = NOZZLE ABSOLUTE SPOUTING VELOCITY

U = TURBINE WHEEL TIP SPEED

W = RELATIVE FLOW VELOCITY

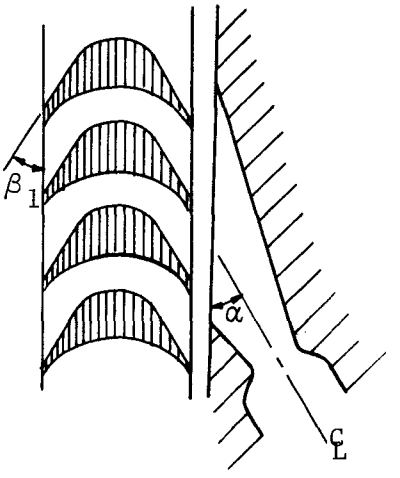

TURBINE BLADE AND NOZZLE SECTION

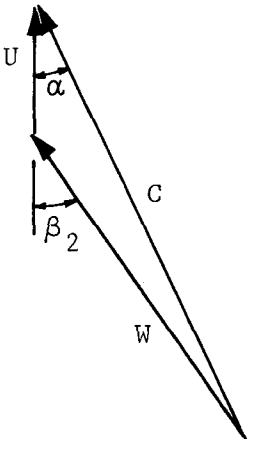

VELOCITY TRIANGLE

F09157 U

FIGURE 7-2. TURBINE TERMINOLOGY

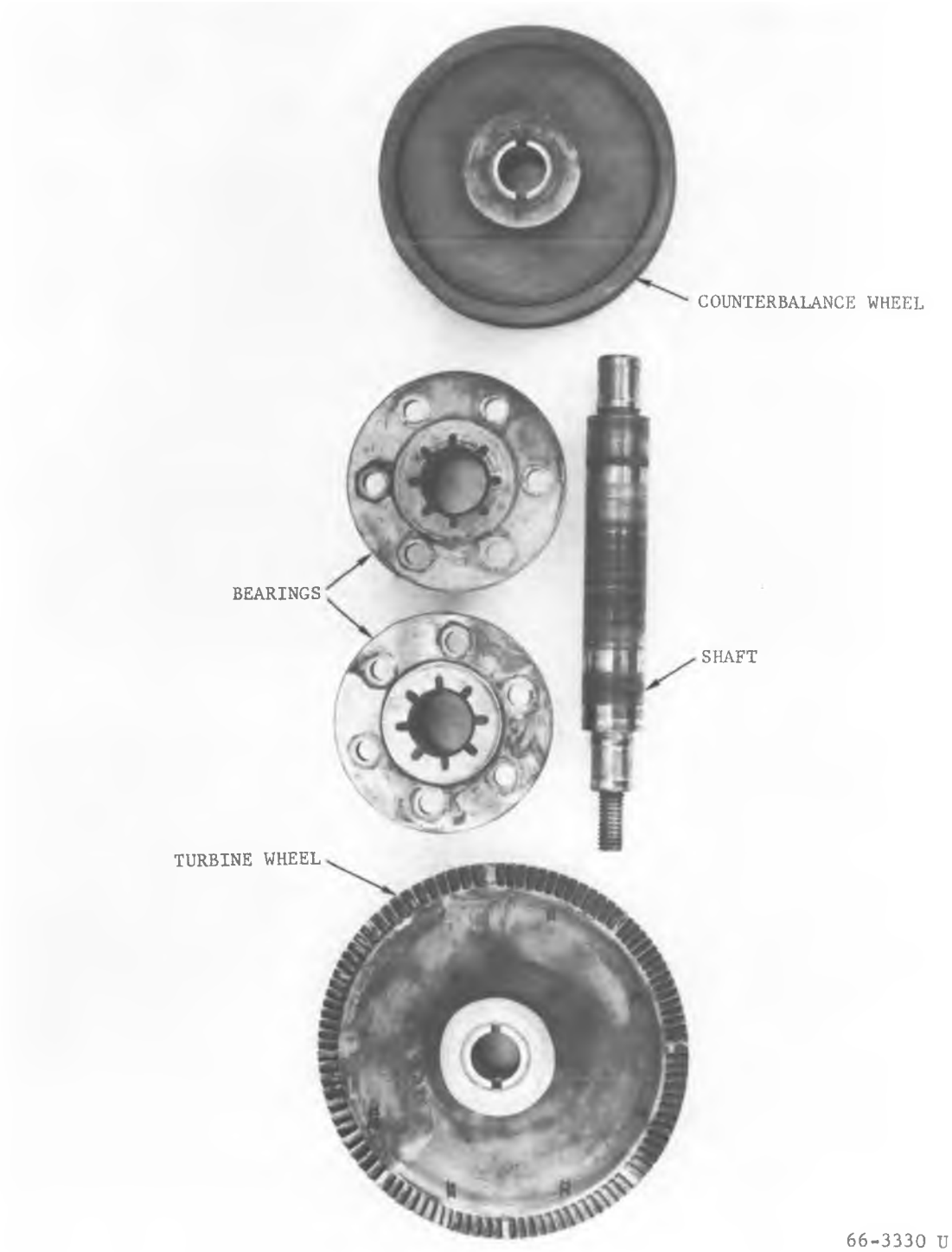

FIGURE 7-3. TURBINE WHEEL, SHAFT, BEARINGS, AND COUNTERWEIGHT AFTER ENDURANCE TEST

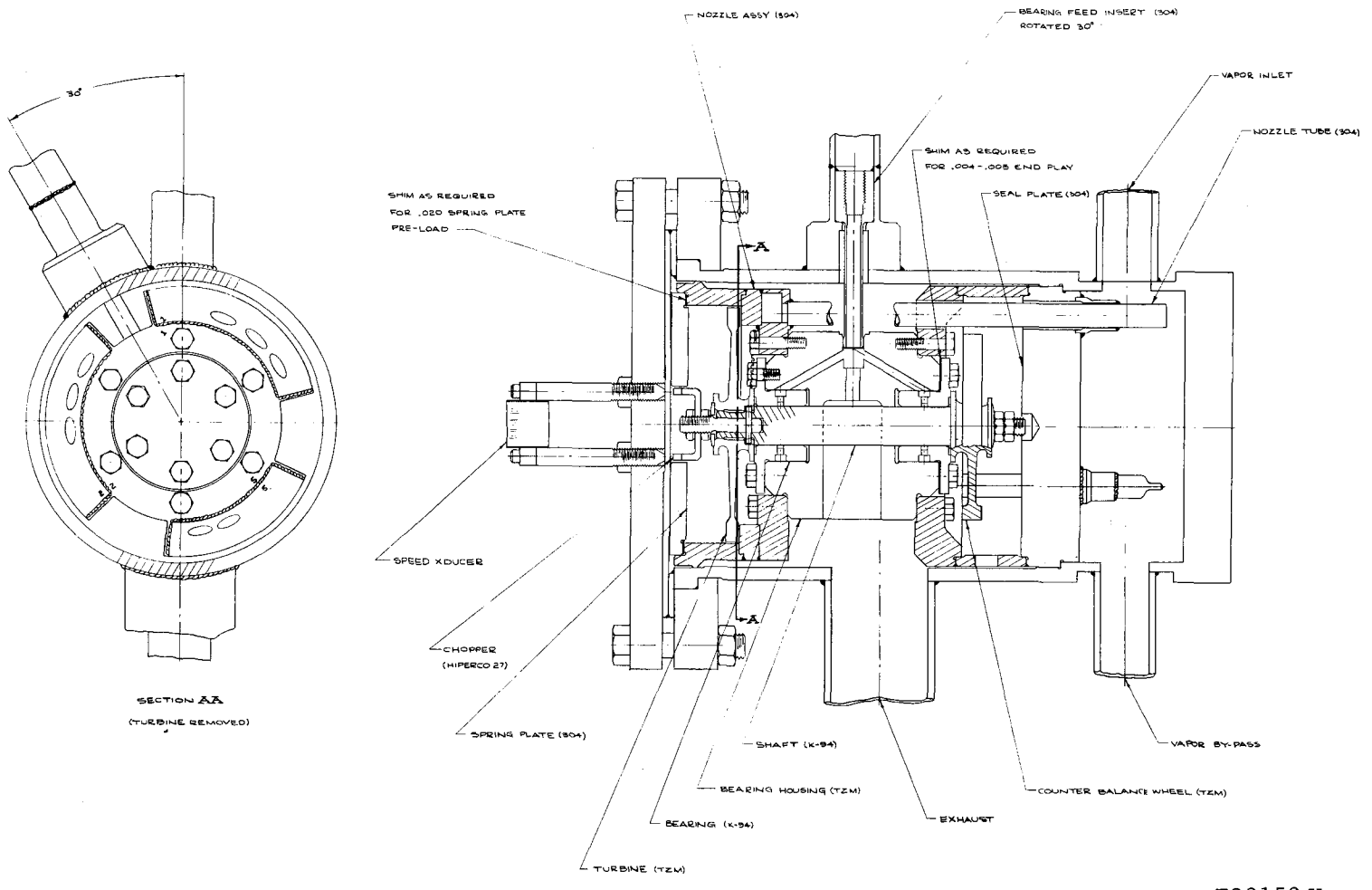

FIGURE 7-4. TEST SECTION LAYOUT DRAWING SHOWING MOUNTED TEST TURBINE

FIGURE 7-5. ASSEMBLED TEST SECTION PRIOR TO TESTING

The bearings employed were of the fluid film journal type which used the systems liquid potassium for the lubricant. The turbine and counterbalance wheel were mounted on the shaft which also served as the journals. The material for both the shafts and the bearing was fine grained tungsten carbide with a 14 percent cobalt binder.

In order to minimize distortion and misalignment due to thermal expansion differential, the bearings where mounted in a husky housing made of Climax TZM Molybdenum. The radial clearance between the journal and bearings was 0.001 inch. The flanged faces of both the turbine wheel and the counterbalance wheel were used to take the axial thrust. The clearance for axial play was 0.020 inch total. This relatively large clearance (room temperature) was selected in order to compensate for the temperature difference between the shaft and the bearing housing during operation.

As indicated in Figure 7-4, the rotating assembly was designed such that the bearings are equally loaded in the static condition, i.e., the counterbalance wheel was also designed to have the same polar moment of inertia. The finished rotating assembly was then dynamically balanced to within 0.001 inch-ounce of displacement.

The cylindrical bearings were stabilized by means of a hydrostatic load being applied across the mid-portion of the shaft. Figure 7-4 also shows the location of the hydrostatic load pocket, the bearing and load pocket supply pressure lines.

In addition, a speed sensing pickup was incorporated in the test unit, which allowed speed sensing through the hermetically sealed housing. The magnetic field is set up by a 1/2-inch diameter, 1/2-inch long Alnic V permanent magnet. The magnet is installed between two Hyperco-27 poles, which butt up to the end of the hermetic housing. The magnetic field travels down the poles, through the housing which is approximately 0.075 inch thick and across a 0.040 inch air gap to a (2) pole magnetic chopper. When the chopper rotates, the magnetic field intensity in the magnet varies. The varying field is sensed through a 10,000 turn coil which is wound on a bobbin placed around the magnet.

This arrangement produces a 2-cycle output signal per revolution of the shaft. The output level increases with speed to approximately 10,000 rpm and then essentially remains constant due to the effects of eddy currents set up in the chopper, housing and surrounding structure. The output level at 10,000 rpm is approximately 1 volt, peak to peak. This output level is quite low, but was adequate for the present test in conjunction with a digital counter. The pole pieces leading from the magnet to the housing are several inches long to isolate the sensing coil from the high temperature housing.

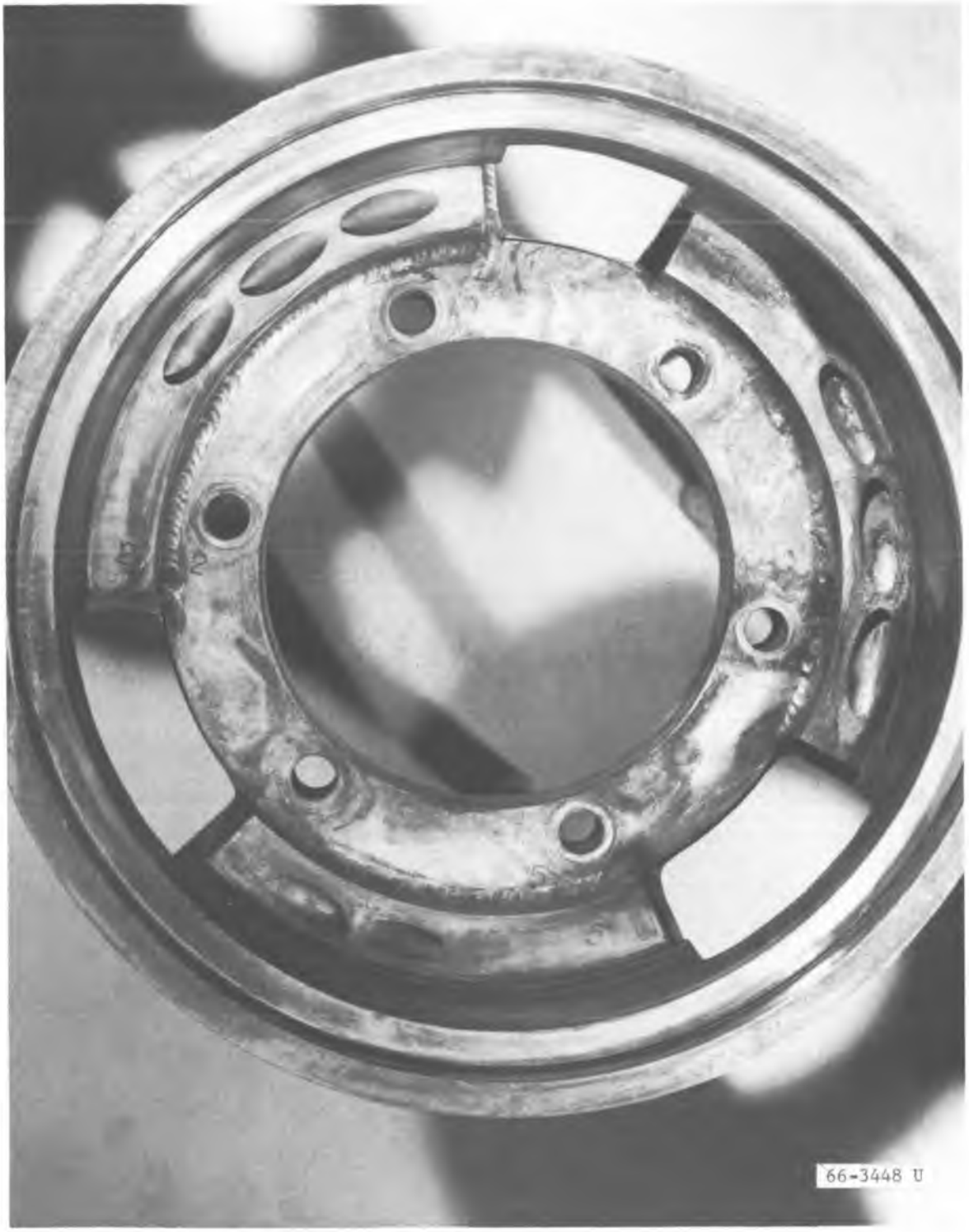

FIGURE 7-6. TEST TURBINE NOZZLE ASSEMBLY SHOWING THE THREE PARTIAL ADMISSION NOZZLE BLOCKS

The turbine buckets were machined by the electro-spark discharge method (Elox). The same tooling was utilized for all blade sections; however, the tool holder was rotated for each section, in order to provide the specified variation in leading edge blade angle or gas flow incidence angle. Due to the resulting low efficiency turbine configuration, the bearing friction was sufficient for speed stabilization and no additional positive loading device was installed.

The test turbine design included three different partial admission nozzle blocks as shown in Figure 7-6 taken after the test was completed. As can be seen in this figure, the nozzle blocks are numbered 1, 2, and 5, in accordance to the thermodynamic processes selected during task I. Nozzle block No. 1 consists of three 0.167 inch throat diameter nozzles having an absolute flow angle of 21 degrees. This nozzle block was the one used during the 96-hour continuous test run. Nozzle block No. 2 consists of three 0.156 inch throat diameter nozzles having an absolute flow angle of 22 degrees. This nozzle was used for a short time only due to difficulties in attaining sufficiently high turbine speeds. Nozzle block No. 5, which consisted of two 0.122 inch throat diameter nozzles with absolute flow angle of 22 degrees, was used only during initial checkout runs of the test turbine.

7.3.2 TEST OPERATIONS

The first attempts to obtain sustained operation of the potassium turbine using nozzle No. 5 with two 0.122 inch throat diameter nozzles were unsuccessful. Initial rotation was achieved but after two minutes or rotation, in which the speed reached 14,000 rpm, the unit stopped abruptly. Successive restart attempts were unsuccessful. The turbine was then removed from the loop. The journal bearings were found to exhibit slight wear and the thrust bearings showed definite signs of seizing. Both journal bearings were then hand polished and the thrust bearings were relapped. The bearing housing was also re-machined to allow an end play of 0.026 inch between the thrust bearings instead of the initial 0.004 inch.

The unit was reinstalled in the potassium loop but difficulties were again experienced in starting the test turbine. In particular, it was found that when using nozzle block No. 2 with full pressure on the fluid dynamic shaft load device, the shaft speed was limited to 6000 rpm. Analysis of the test results indicated that a combination of problems, such as leakage of vapor flow through the test section and insufficient starting torque, limited the test turbine speed. In order to resolve this problem, the loop operation was stopped. The turbine was removed from the loop, cleaned, and subjected to nitrogen testing using alcohol as the bearing lubricant. During these tests, start-ups were accomplished with both nozzle blocks No. 1 (three 0.167 inch throat diameter nozzles with 21 degrees entrance angle) and No. 2 (three 0.156 throat diameter nozzles with 22 degrees entrance angle) with various amounts of hydrodynamic shaft loading provided. It was determined that nozzle block No. 1 produced the largest starting torque with the test turbine.

The break-away torque on the dry unit was 7-9 inches-ounces. With the bearings wet with alcohol it took 2.5 to 3.0 psi nitrogen gas differential pressure across the turbine wheel to initiate rotation. It was further determined that as bearing lube pressure was increased, thus increasing the hydrostatic loading on the shaft, the gas pressure differential required to rotate the turbine increased. After the turbine had accelerated to 20,000 rpm the bearing lube pressure and shaft loading could be increased without any significant shaft speed reduction. It was therefore decided not to initiate bearing lubricant flow until initial rotation had been established. It was also decided to use nozzle block No. 1 in subsequent testing due to its ability to produce a higher starting torque with the available vapor flow condition of the potassium loop.

After the nitrogen-alcohol tests, the unit was baked out and reinstalled in the potassium loop. The seal plate was then welded in place. The pressure plate was bolted in place and tightened to load the seal between the high pressure chamber of the test fixture and the turbine exhaust cavity.

The potassium loop was then brought to 1000°F. At this time the turbine by-pass valve was closed as the loop continued up in temperature. As design conditions were approached the turbine inlet valve was closed allowing the boiler pressure to build up to 5 psia. As the turbine inlet valve was opened the turbine began to accelerate and bearing lubricant flow was established. Heater and flow settings were then adjusted to maintain design conditions as closely as possible. A 96-hour continuous endurance run was then achieved. Figure 7-7 presents the test conditions experienced as a function of the cumulative test time.

One problem which occurred throughout the program was the leakage of potassium around the seal isolating the high pressure chamber from the low pressure side of the test section. This leakage was prevalent on all of the turbine runs and resulted in increased boiler flow. With this increased mass flow, the boiler operating at full capacity was unable to operate consistently above the 1250°F turbine inlet temperature. It was possible, however, to accumulate 96 hours of continuous turbine rotation. It was also noted during the test, that an increase of hydrostatic loading of the shaft was necessary to maintain turbine speed (at about 60 hours) following the turbine slow-down due to a probable increase of bearing friction. The load device was exposed to full pump discharge pressure to maintain the best performance. The test was terminated when turbine operation became erratic and it was impossible to regain a steady turbine speed.

Disassembly showed the journal bearings to be in reasonably good condition but there was approximately 0.06 inch material removed from the turbine end thrust bearing indicating a complete breakdown in lubrication to that thrust face.

Both the turbine wheel blades and the nozzles used in the test showed considerable evidence of erosion and/or corrosion. These components are discussed in detail in the following paragraphs.

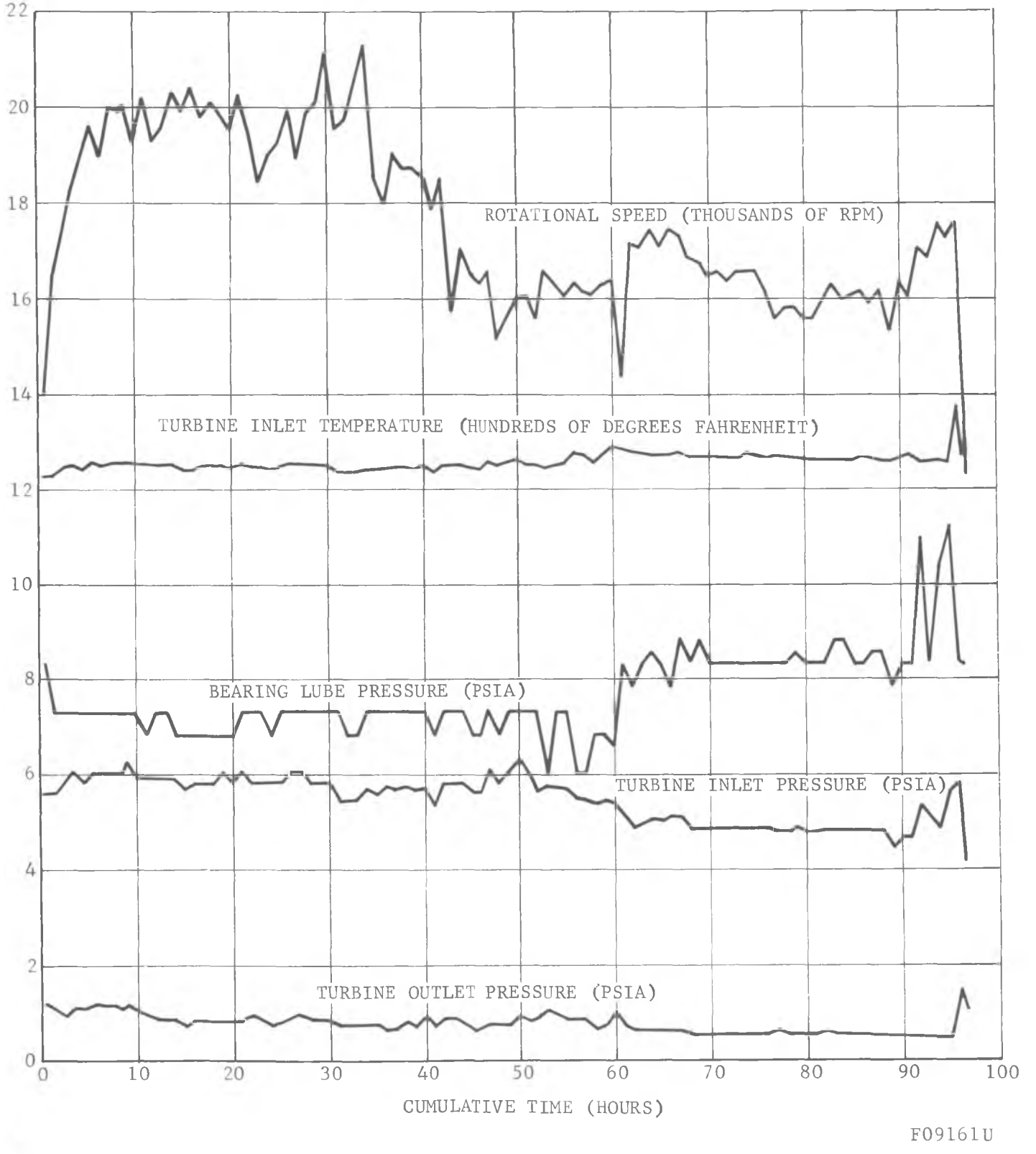

FIGURE 7-7. TEST CONDITIONS DURING ENDURANCE TEST OF POTASSIUM TURBINE

7.4. TEST RESULTS

7.4.1 TURBINE BLADES

The test turbine wheel showed very definite erosion patterns on all blade configurations after the conclusion of the endurance run. Figure 7-8 shows the test turbine wheel as it appeared after testing (the before testing picture has been shown in Figure 7-1). The typical appearance of the turbine blades before testing is presented in Figure 7-9 where a close-up photograph of the Section VIII blades is shown. Figures 7-10 through 7-13 are close-up photographs of the turbine blades after testing having blade angles of 25, 30, 35, and 40 degrees, respectively. A sketch of the typical erosion patterns encountered on the blades of each section is presented in Figure 7-14. It should be emphasized that the differences in blade geometries had no discernable effect on the erosion pattern.

All erosion encountered was concentrated in the vicinity of the blade leading edge, as would be expected. Only slightly noticeable erosion occurred on the concave surface of the blades. The convex surface, however, had a deep groove which ran in an approximately straight line from a position slightly above the blade root up to the blade tip making a slight angle (approximately 5 to 10 degrees) with a ray, as shown in Figure 7-14. Other than this single deep erosion groove, the convex surface of the blades had only slightly visible erosion damage.

The flat surface at the leading edge of the turbine blades had several interesting features. First, near the blade root there was a very prominent groove which started at the concave edge at an angle of about 60 degrees and ran upward to the convex edge at an angle of 30 to 40 degrees. This groove is believed due to liquid impinging on the flat of the blade coming off the nozzle walls and proceeding at the angle of 30 to 40 degrees due to two forces on the liquid layer: (1) a centrifugal force in the radial direction and (2) an aerodynamic force in the tangential direction. The groove on the convex face of the blade seems to start at or near the point where the groove on the flat surface intersects the convex edge. Near the tip of the blade on the flat face is a dull gray-white deposit. This deposit is easily scratched revealing a bright metallic surface. Between the deposit and groove, the flat face is slightly but uniformly eroded.

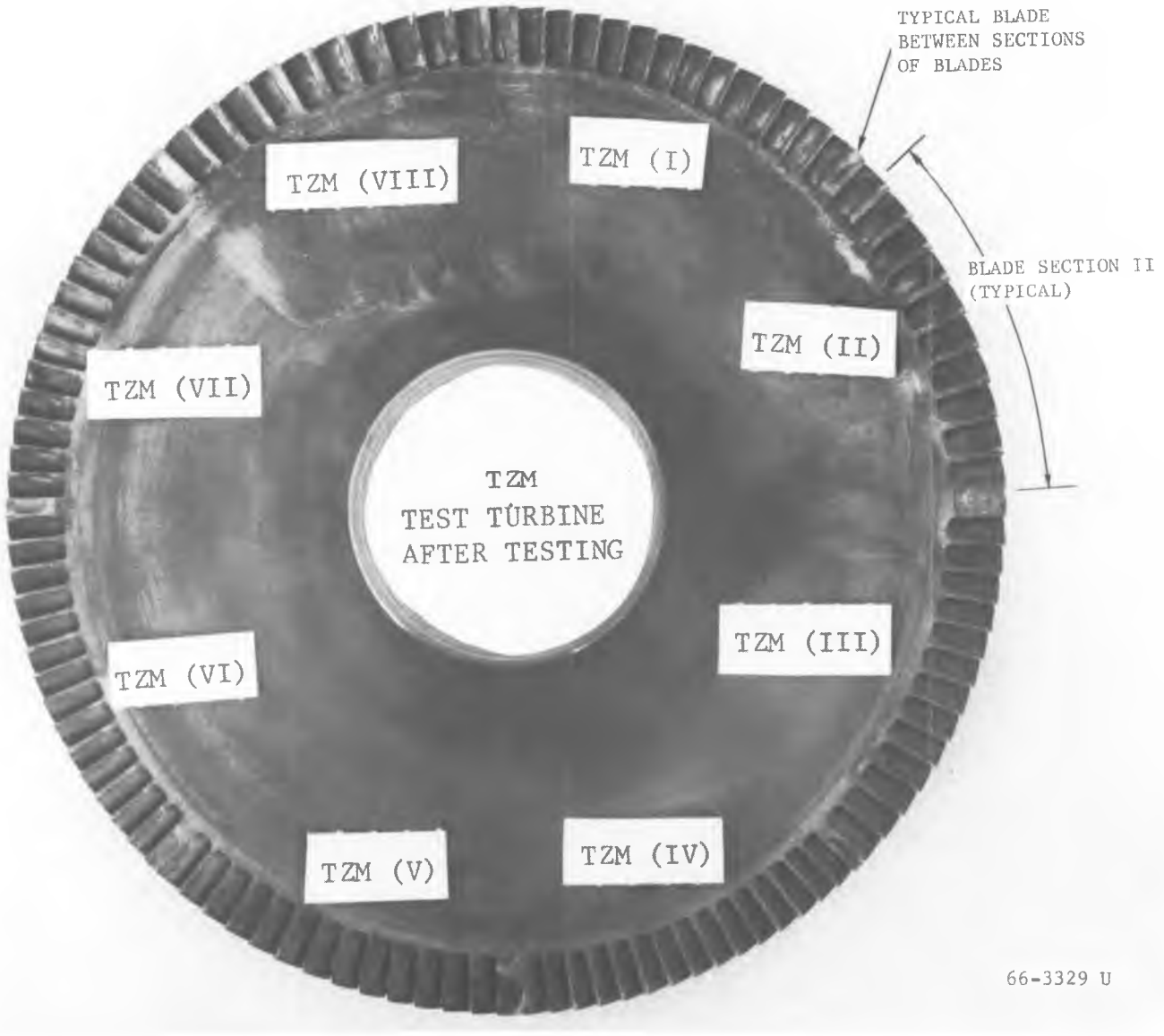

FIGURE 7-8. TASK II TURBINE WHEEL AFTER ENDURANCE TESTING

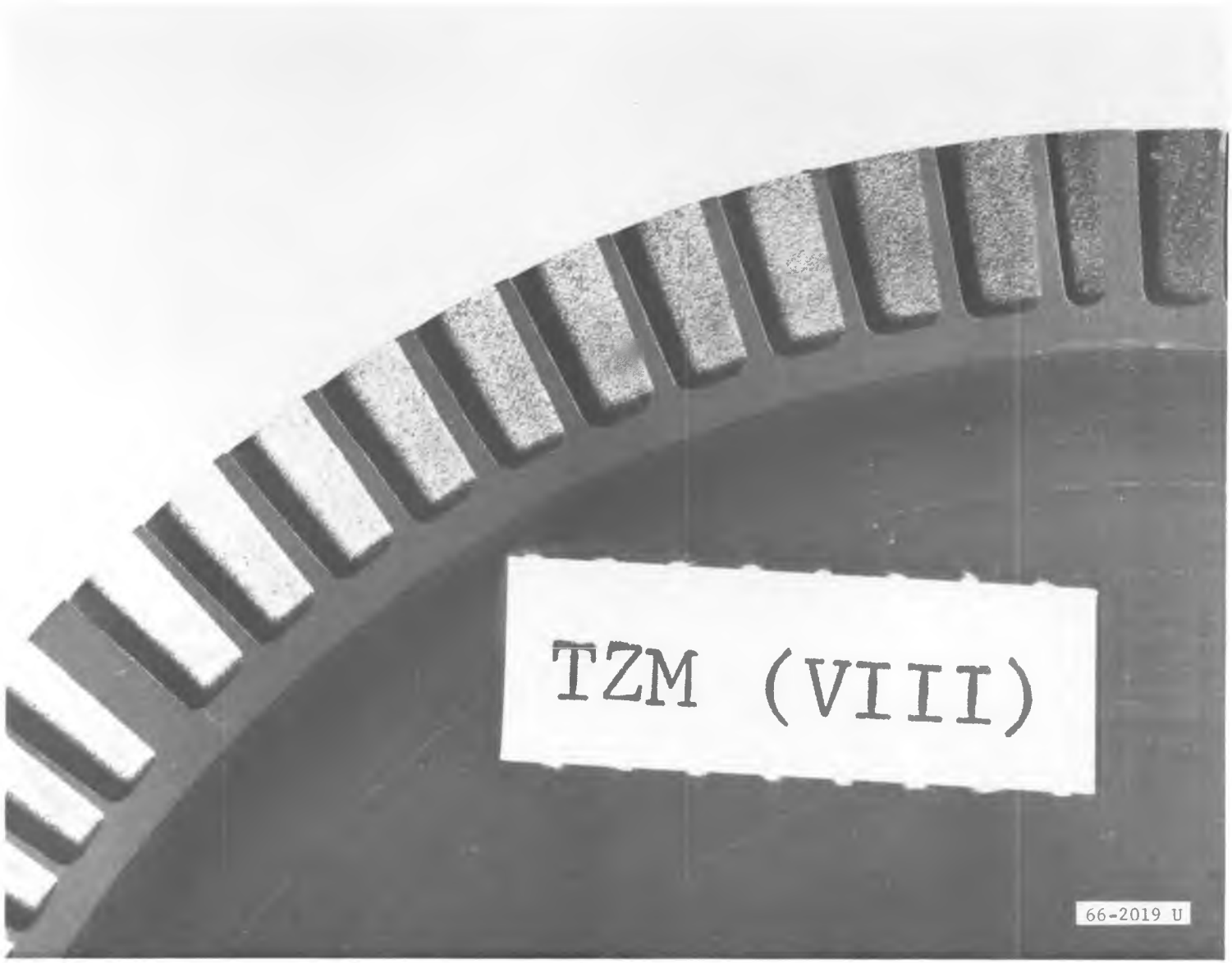

FIGURE 7-9. TYPICAL APPEARANCE OF TURBINE BLADES BEFORE TESTING

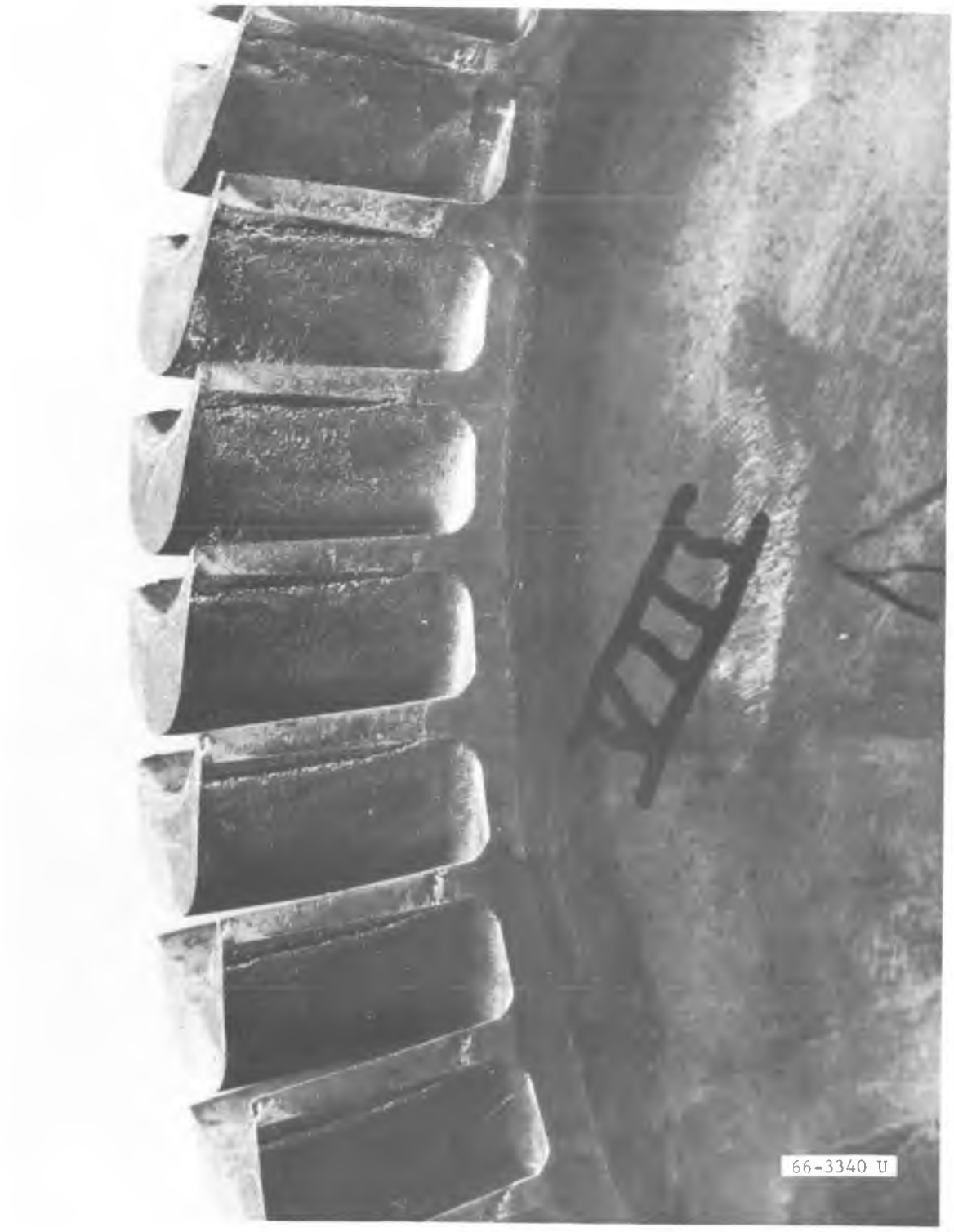

FIGURE 7-10. TURBINE BLADES AFTER ENDURANCE TEST, 25 DEGREE BLADE ANGLE SECTION VIII

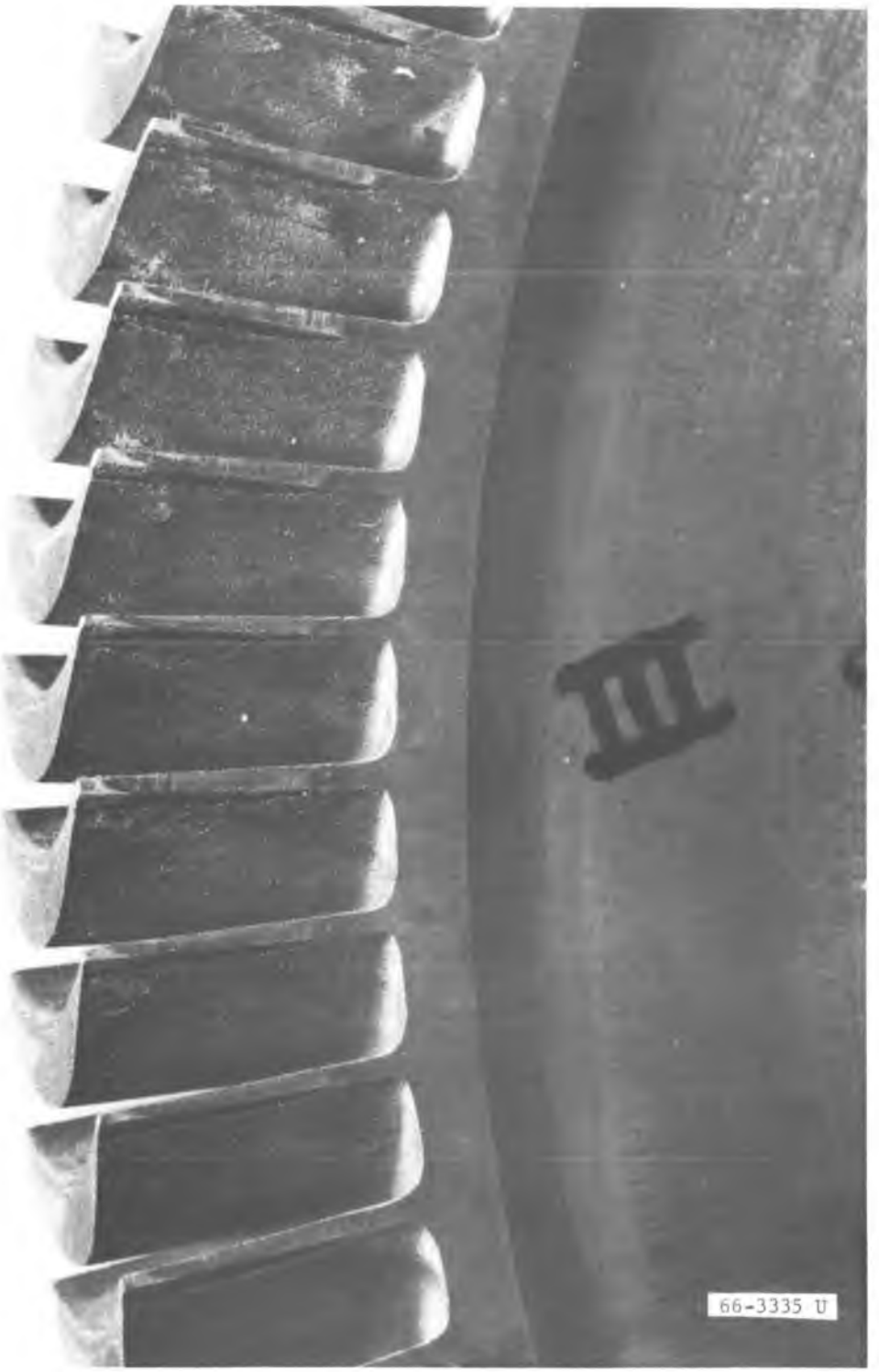

FIGURE 7-11. TURBINE BLADES AFTER ENDURANCE TEST, 30 DEGREE BLADE ANGLE SECTION III

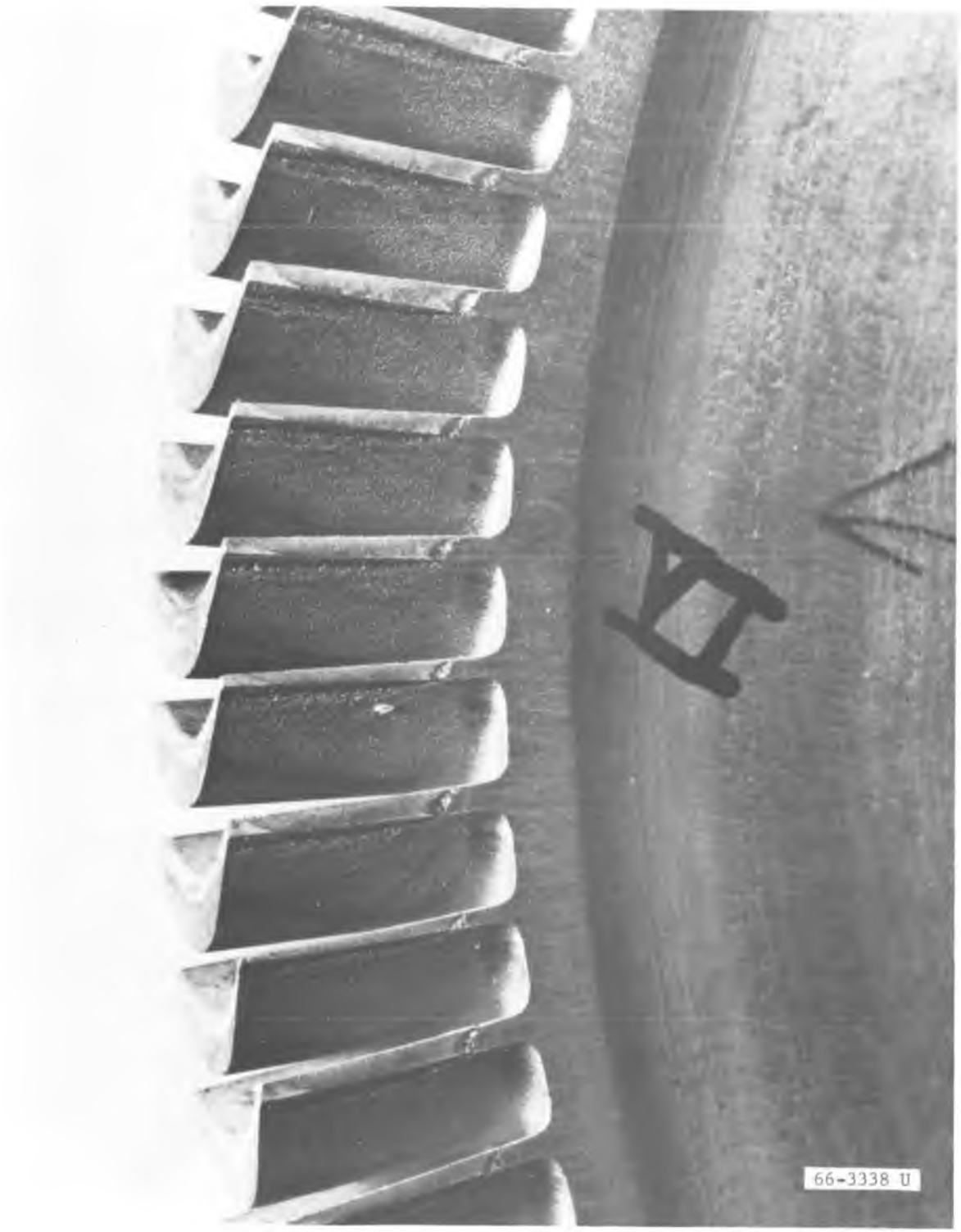

FIGURE 7-12. TURBINE BLADES AFTER ENDURANCE TEST, 35 DEGREE BLADE ANGLE SECTION SECTION VI

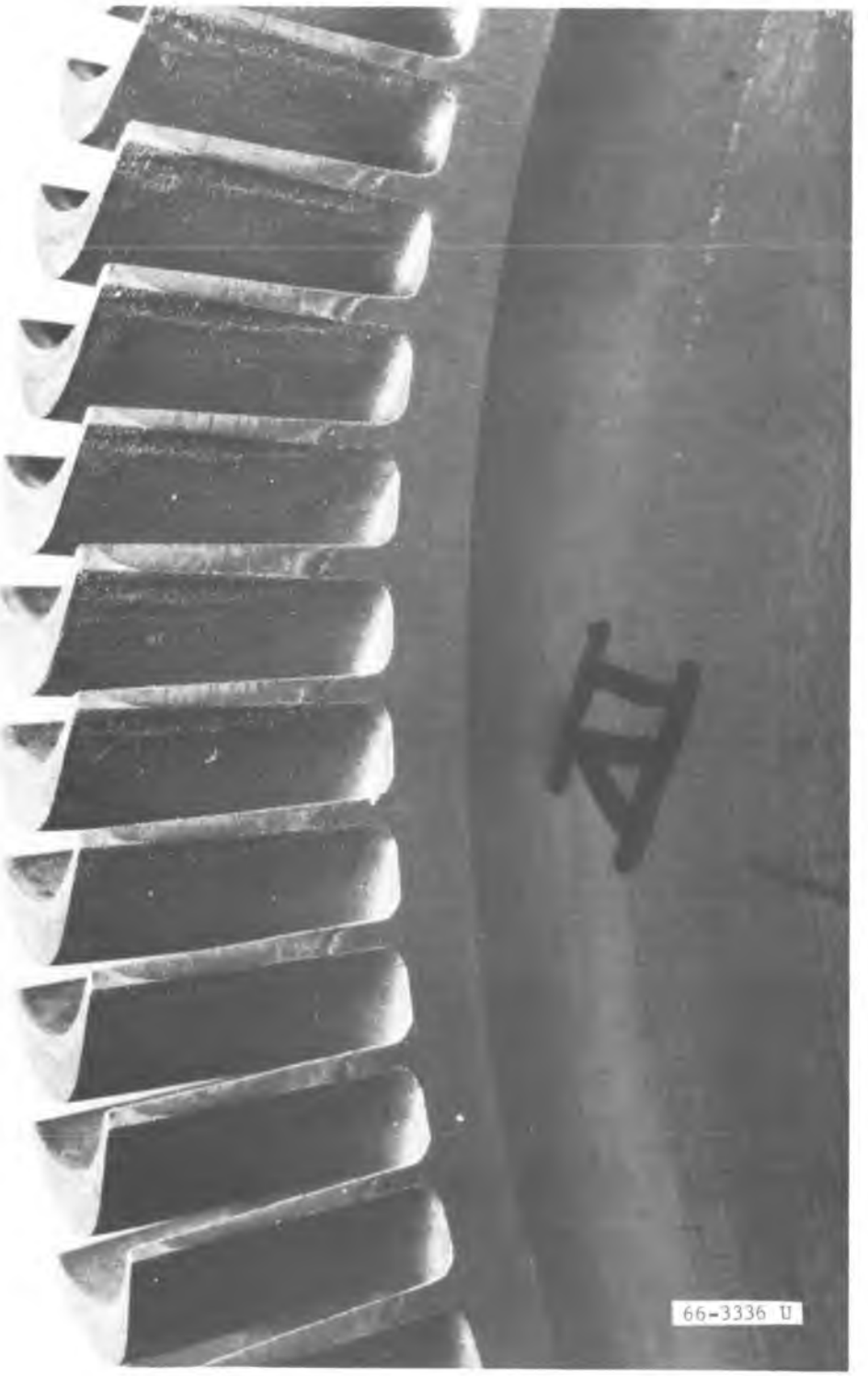

FIGURE 7-13. TURBINE BLADES AFTER ENDURANCE TEST, 40 DEGREE BLADE ANGLE SECTION IV

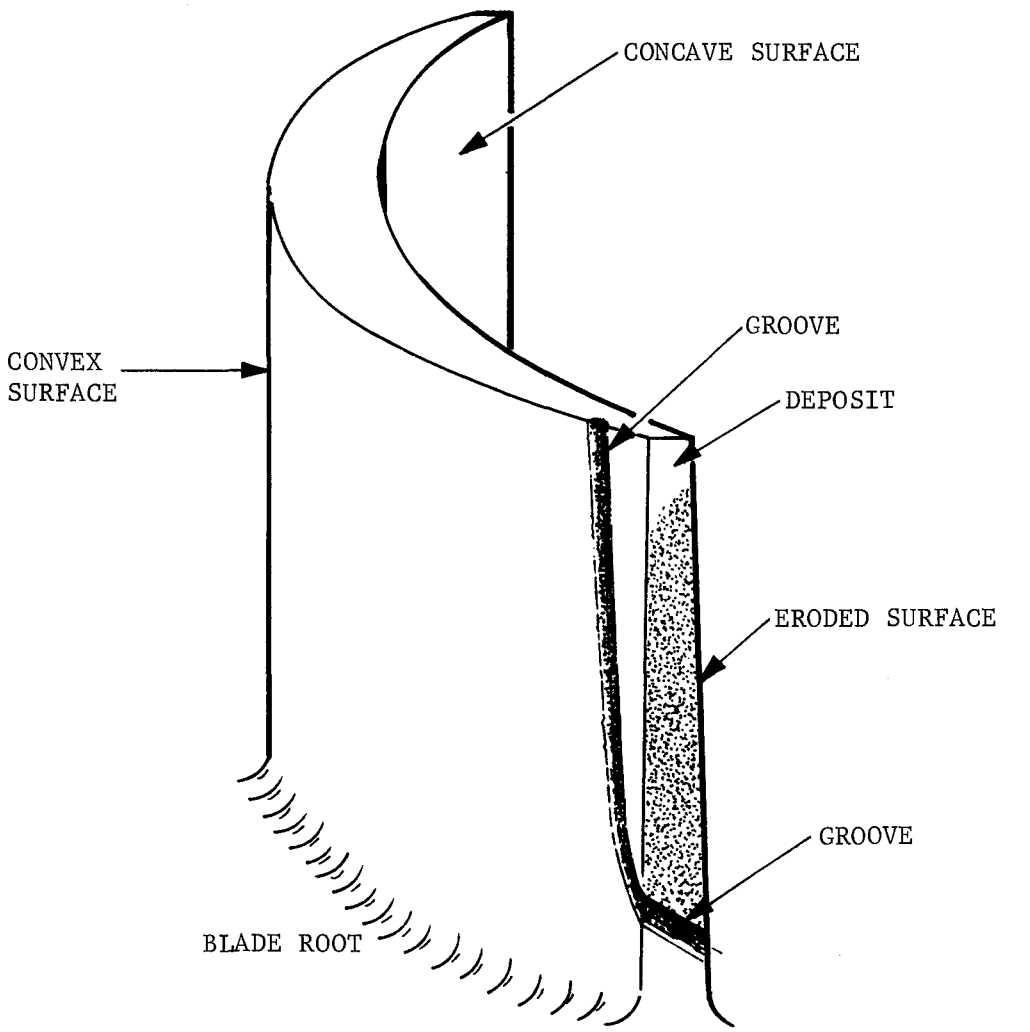

FIGURE 7-14. TYPICAL TURBINE BLADE EROSION PATTERN

The blades between sections of blades, Figures 7-15 and 7-16 show some interesting phenomena. Figure 7-17 is an interpretive drawing of the photograph of Figure 7-16. The groove or liquid film gouge is similar to that on Figure 7-14 except that on the flat of the blade it reaches a maximum radius on the wheel and is impaired from going further radially because of strong aerodynamic forces in the tangential direction.

The groove on the convex side of the large blade is similar to that of the small blades except that it may be deeper indicating a higher mass transfer. Figure 7-17 also shows a heavy groove at the outer radius or near the tip of the blade and on the flat. This groove may also be due to liquid emerging from the nozzle walls. The next heaviest erosion is shown on Figure 7-17 as the mild erosion area and on Figure 7-16 as the darkened area. Within this region a uniform parallel wave pattern was found to exist on all the blades between sections of blades with a wave length of 0.002 inch. The area of least erosion is the slight erosion area indicated on Figure 7-17. Finally a gray-white deposit is shown which is found on all the blades of the wheel.

Due to their longer flat lengths, the blades between sections of blades, as indicated in Figure 7-8, act as wedges in a supersonic nozzle exhaust environment. These blades, except for a centrifugal force, show phenomena which are similar to those seen on the wedges of this program. An erosion length can possibly be defined on Figure 7-16. However, due to detached flow conditions the corresponding particle size could not be deduced from the indicated damage length.

7.4.2 NOZZLES

An unexpectedly large amount of erosion and corrosion occurred in the nozzles of nozzle block No. 1 during the 96-hour turbine test. The entire turbine nozzle assembly after testing was shown previously in Figure 7-5 A close-up view of nozzle block No. 1 is presented in Figure 7-18. As can be seen from this figure, the middle nozzle has a large material deposit inside it with a very substantial material loss resembling erosion occurring between this deposit and the end of the nozzle. A similar but much smaller deposit and erosion occurred in the first nozzle (to the left of the middle nozzle). However, this deposit was much nearer the throat than the deposit in the middle nozzle. Very slight deposition occurred in the last nozzle.

The large deposit in the middle nozzle was chemically analyzed and found to contain the metallic elements in the approximate proportions shown in Table VII. All these elements except copper are constituents of the materials from which the potassium loop is fabricated; i.e., Haynes 25 (boiler preheater), 316 stainless (nozzle assembly), and 304 stainless (remainder of loop). As indicated at the 1966 Turbine Erosion Meeting*,

*Turbine Erosion Meeting, Jet Propulsion Laboratory, Pasadena, California, December 29 and 30, 1966.

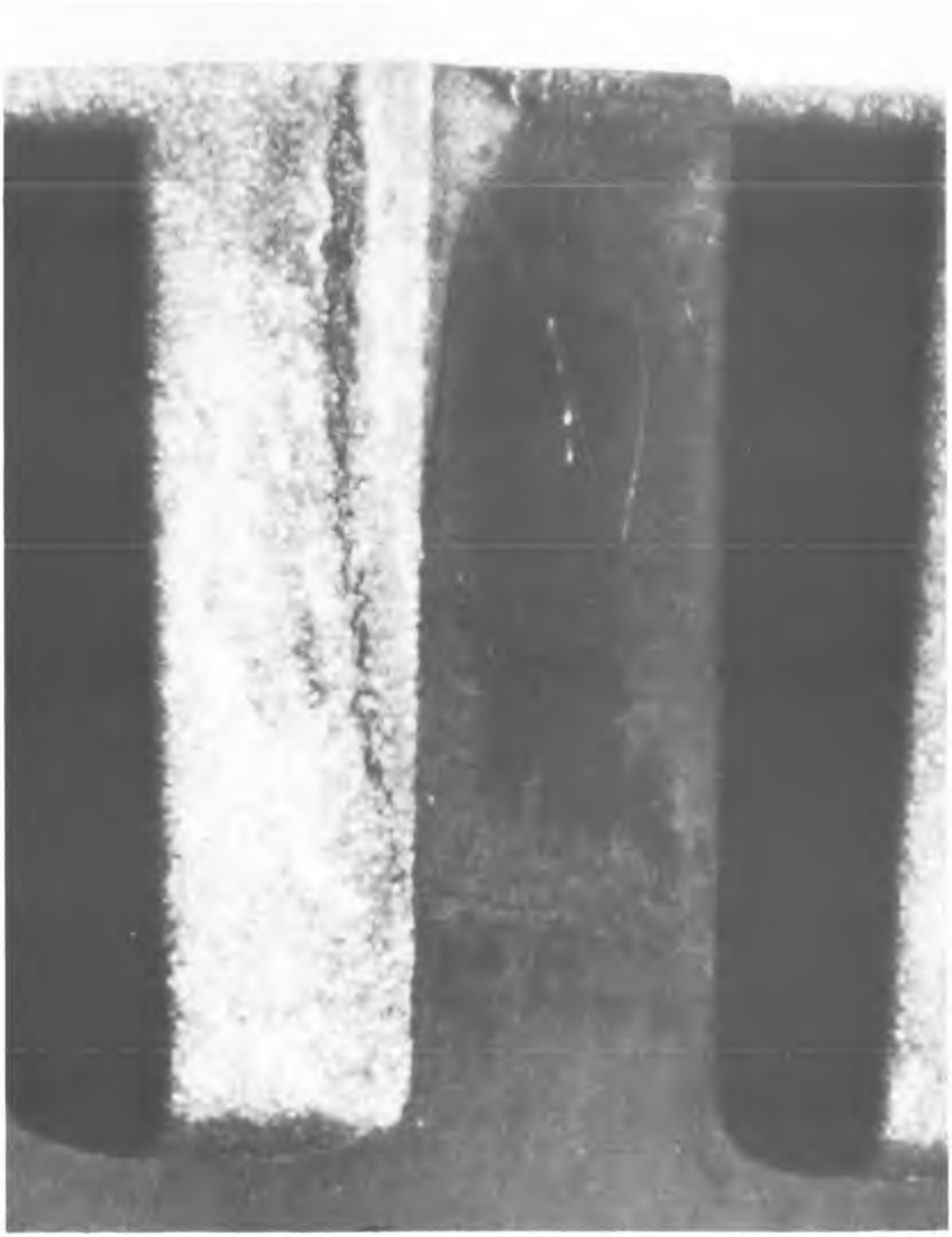

F09169U

FIGURE 7-15. EROSION PATTERN ON BLADE BETWEEN BLADE SECTIONS III AND IV (LOOKING AXIALLY)

F09170U

FIGURE 7-16. EROSION PATTERN ON BLADE BETWEEN BLADE SECTIONS IV AND V (LOOKING AXIALLY)

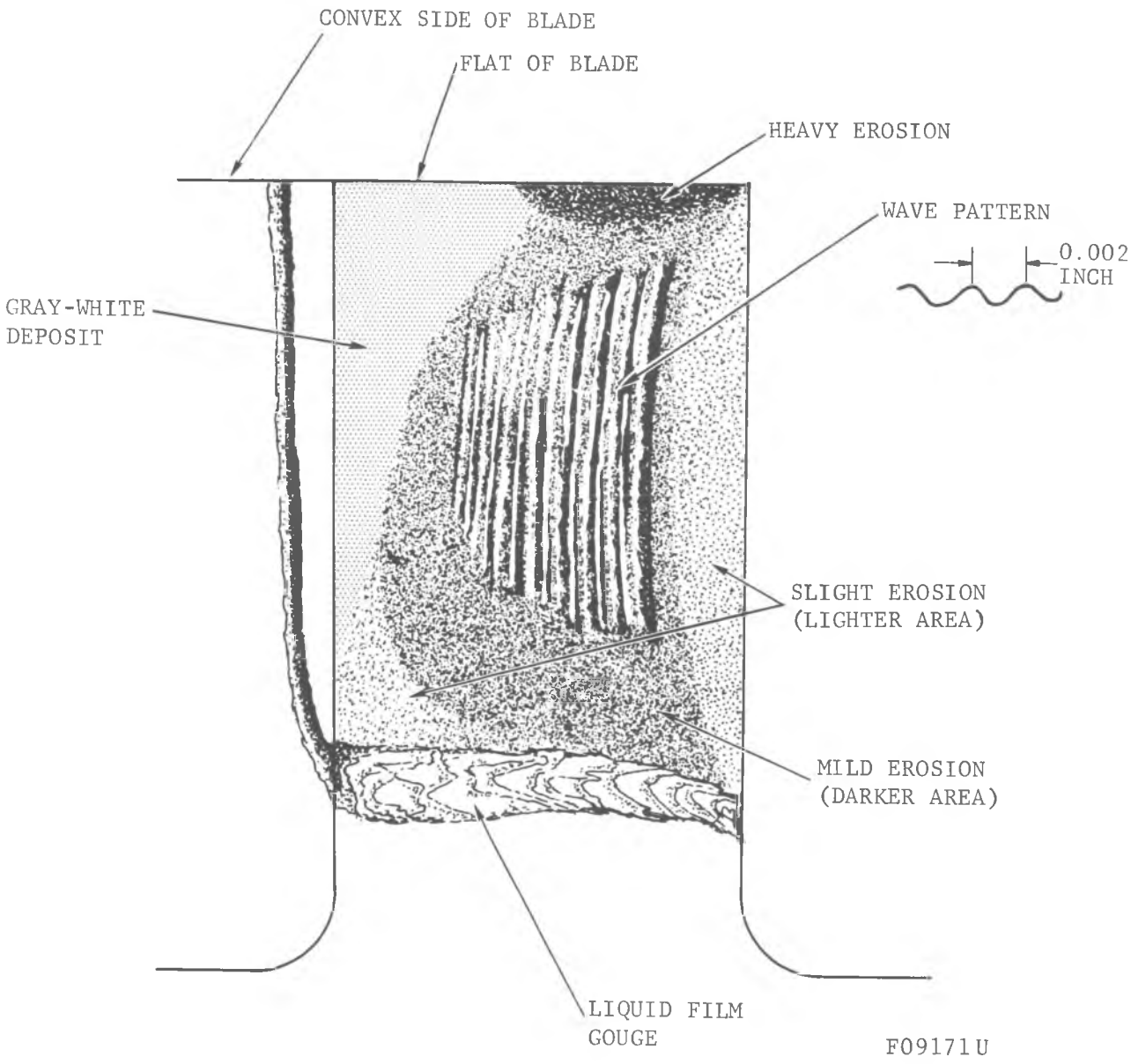

FIGURE 7-17. INTERPRETIVE SKETCH OF FIGURE 7-16.

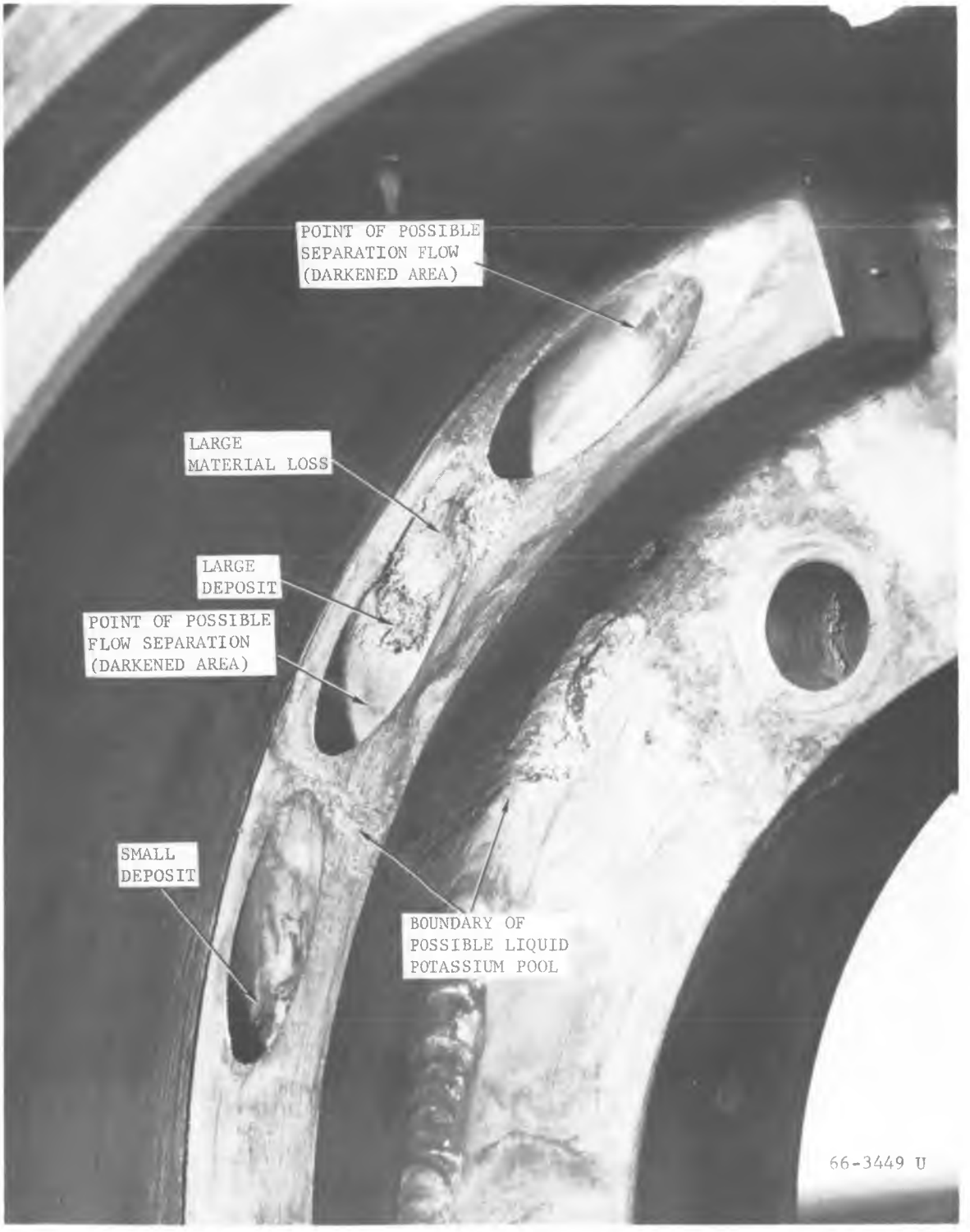

FIGURE 7-18. NOZZLE BLOCK NO. 1 AFTER ENDURANCE TEST

Table VII. Deposit Composition

Element	Relative Percent
Iron	73.8
Nickel	20.4
Copper	3.1
Chromium	1.7
Cobalt	0.5
Manganese	0.4
Molybdenum	0.1

other investigators have also noticed this loop material mass transfer to their turbine nozzles. The presence of copper in the deposit cannot be satisfactorily explained. Although some copper gaskets are present in the loop, they are located in the vacuum line and it is inconceivable that copper from this cold location could find its way into the test section.

Also shown in Figure 7-18 is what could possibly be the boundary of a pool of liquid potassium which existed during the running of the test. At any rate, there was significant mass transfer in the vicinity of the middle nozzle. The boundary, which is easily discernible in the photograph, is not a stain but consists of built-up and eaten-out areas. The surfaces on either side of this visible boundary are rather smooth; thus, if a pool of liquid potassium did exist around the middle nozzle, it appears that most of the mass transfer which occurred took place at the edge of this pool. During the test run, nozzle block No. 1 was oriented at approximately the 11 o'clock position as viewed looking into the discharge side of the nozzle assembly.

After the test, the plenum chamber of nozzle block No. 1 was cut open and inspected. There was no evidence of either erosion or corrosion. The surfaces, including the nozzle entrances, were virtually clean and free of any stains or variations in color tone. Some slight deposit was discernible at the nozzle entrances.

Close examination of the last two nozzles reveals a darkened area nearer the throat (see Figure 7-18). Although this feature might exist in the first nozzle, it cannot be distinguished because of the stains occurring there. From the symmetry, location, and appearance of this darkened area (which is somewhat harder to distinguish on the photograph than on the actual hardware), it is thought possible that the flow prematurely separated from the nozzle wall at this location.

From the appearance of the nozzles, corrosion or chemical attack seems to have taken place. This conclusion seems to be in line with Reference 25. They state that for potassium loops with oxygen content above 50 ppm there is a strong correlation between damage observed and oxygen content. Although no measure of oxygen during loop operation was made, it is believed that the content was above this limit because of the number of times the loop was opened and closed during the Task I and II testing.

7.5 DISCUSSION OF RESULTS FROM TURBINE EROSION TESTS

7.5.1 ESTIMATED DROPLET SIZES

Two sizes of drops impinged on the turbine wheel: (1) the primary drops in the vapor flow of a submicron size as presented in Reference 3, and (2) the large secondary drops shed from the liquid puddle formed downstream of the separation zone of the nozzle. The primary drops caused the slight erosion or corrosion visible on the flat of each blade while the secondary drops formed the groove on the flat and convex sides of the blade. The erosion groove on the flat of the blade, as indicated on Figure 7-14, forms the basis of a model for prediction of the secondary droplet sizes. As shown in Figure 7-19, the groove starts at an angle, θ, formed by the equilibrium between two forces: (1) the centrifugal force, F_c, in the radial direction and (2) the aerodynamic drag force, F_D, on the droplets in the tangential direction. The observed angle, θ, was approximately 60 degrees.

The centrifugal force is expressed as

$$F_c = \frac{1}{3} \pi d^3 \rho_\ell \frac{u^2}{D} \qquad 7.27$$

and the aerodynamic drag force by

$$F_D = \frac{1}{8} \pi d^2 C_D \rho_v U_s^2 \qquad 7.28$$

or in terms of the Weber number

$$F_D = \frac{1}{8} \pi d C_D \sigma W_e \qquad 7.29$$

The angle of the groove is:

$$\theta = \tan^{-1} \frac{F_c}{F_D}$$

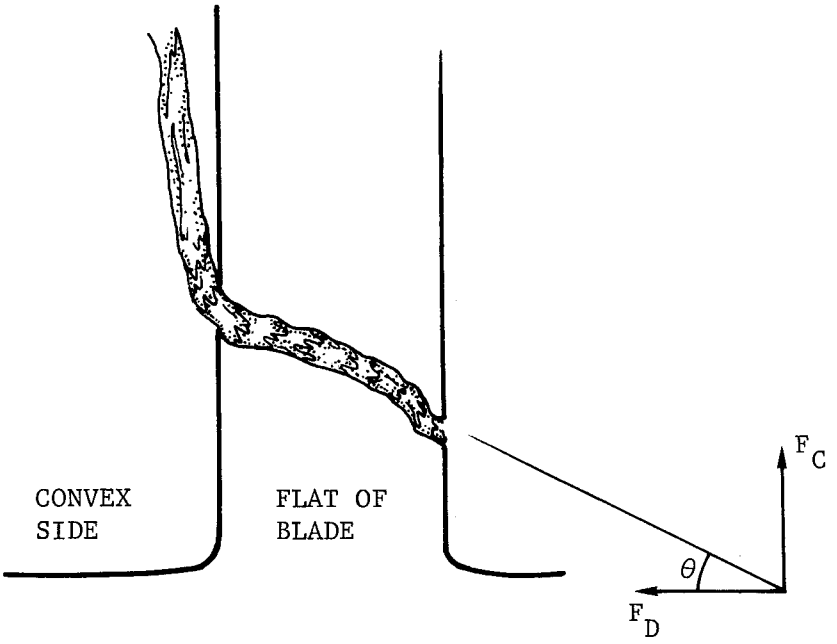

F09173U

FIGURE 7-19. EROSION GROOVE NEAR THE ROOT OF A TYPICAL BLADE (AXIAL VIEW)

or

$$d = \left[\frac{3\ C_D\ \sigma\ W_e\ D\ \tan\theta}{8\ \rho_\ell\ u^2}\right]^{1/2} \qquad 7.30$$

where

d = droplet diameter

D = diameter of wheel at erosion groove

ρ_ℓ = potassium liquid density

ρ_v = potassium vapor density

u = turbine tip speed

U_s = droplet slip velocity in vapor flow

C_D = droplet drag coefficient

σ = potassium liquid surface tension

W_e = Weber number = $\dfrac{\rho_v\ U_s^2\ d}{\sigma}$

Using a value of θ = 60 degrees, a Weber number of 20*, and appropriate values of the other variables in Equation 7.30, the calculated diameter of the drop is 100μ. The slip velocity of these large particles is:

$$U_s = \left[\frac{We\ \sigma}{\rho_v\ d}\right]^{1/2} \qquad 7.31$$

With appropriate values in the above equation, the slip velocity is 1200 ft/sec.

Other criteria used for critical droplet radius and velocities are:

$$\frac{We^2}{Re} = 1 \qquad 7.32$$

*Generally accepted as the Weber number above which droplets break up, e.g., Reference 26.

$$We\ Re = 4000 \text{ or } 2000 \qquad 7.33$$

where Re is the droplet Reynolds number.

The values of slip velocity calculated from these criteria vary from 900 ft/sec to 1100 ft/sec. The Weber number of 20 criteria gives a slip velocity sufficiently close to this range.

Assuming an impingement velocity of:

$$\vec{V}_o = \vec{C}_o - \vec{U}_s \qquad 7.34$$

where C_o is the spouting velocity of the nozzle and V_o is the velocity of the drop before encounter with the turbine buckets, the large drop normal impingement velocity is 400 ft/sec while the drops within the vapor have a before shock normal impingement velocity of 930 ft/sec.

The primary drops cause the mild erosion and the velocity calculated above is a limit to the minimum normal impingement velocity to cause damage. The large secondary drops also have the calculated velocity as the minimum to cause damage. In the presence of an oxygen level above 50 ppm, the potassium is known to be corrosive with the stainless steel. Therefore, the loss of material on the blades is a combined mechanical and chemical phenomena and caution should be used in generalizing the above results.

The results strongly indicate the collection of liquid potassium in a separated region within the nozzle. This is most graphically shown in Figure 7-18. The geometry of the resulting damage is shown in Figure 7-20. Although this damage resulted from corrosion rather than from dynamic erosion, it appears to be a significant problem, sufficiently related to the fluid mechanics, to warrant some discussion here. Turbine nozzles, particularly those having rather high angles with respect to turbine axis, tend to be overexpanded on the long surface of the nozzle; that is, the vapor pressure there may fall below the ambient value. Since the pressure is falling along the nozzle, however, this discharge into a region of relatively higher pressure does not cause flow separation from the nozzle wall, provided the overexpansion is moderate. The data indicate that the situation may be modified when liquid is present. The liquid apparently penetrates upstream along the wall of the overexpanded region, causing a shock boundary layer interaction type of separation. It is well known that rather severe recirculation of fluid occurs in such separated regions, and it is reasonable to expect that significant fluid recirculation would occur in the separated region on the nozzle. This condition provides the best conditions for corrosive action by supplying constantly new reactive material to the location. This conjecture seems to be borne out by the experimental observations.

In spite of the fact that the mechanism is not completely understood, it is well to avoid the possibility of such an occurrence by appropriate aerodynamic design. This may be accomplished by terminating the nozzle more nearly normal to the nozzle axis or by dropping the pressure at the nozzle outlet below a value that would permit separation.

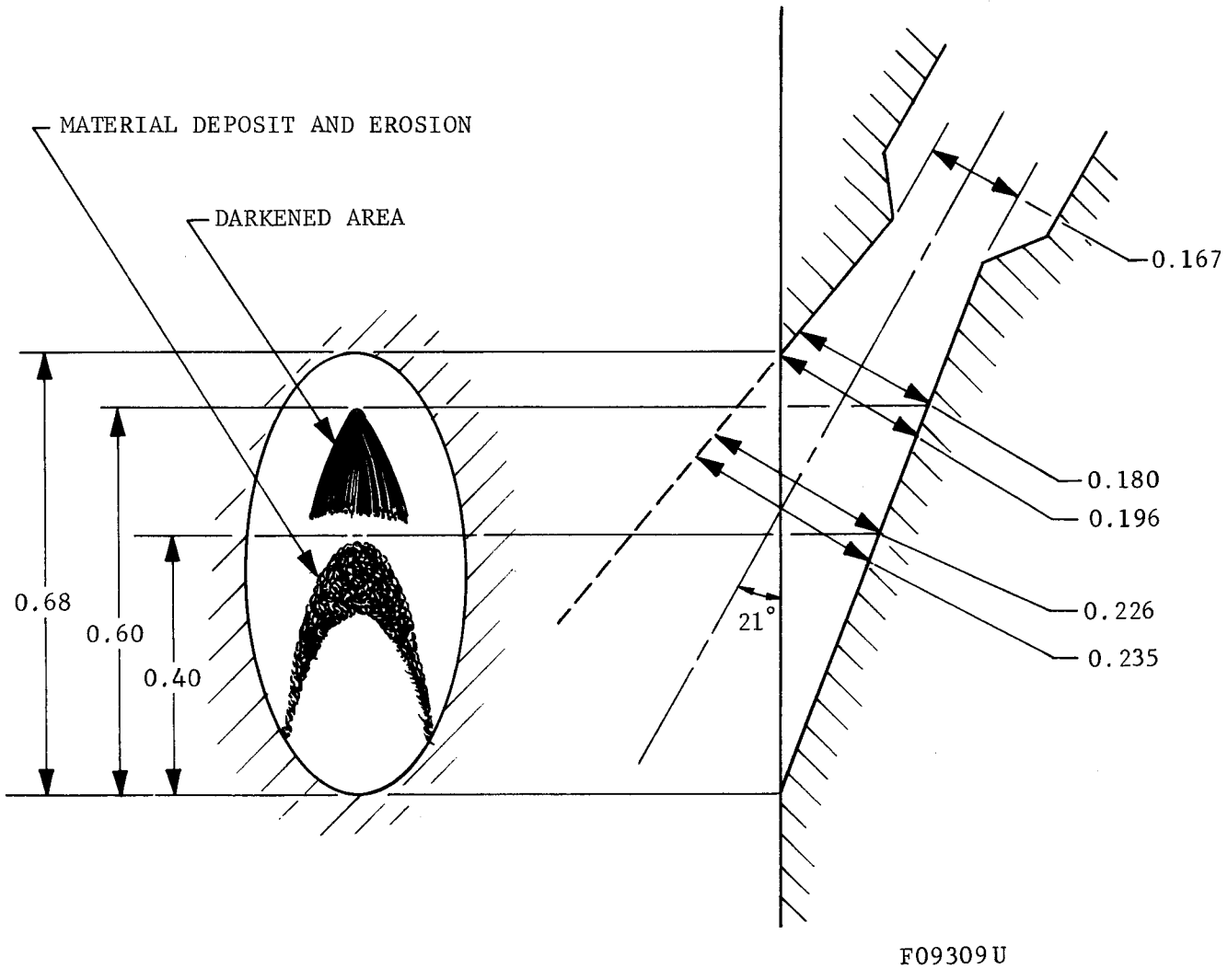

FIGURE 7-20. GEOMETRY OF MIDDLE NOZZLE OF NOZZLE BLOCK NO. 1 AFTER ENDURANCE TEST (DIMENSIONS IN INCHES)

7.5.2 ESTIMATED VELOCITY VECTORS

An estimate will be made of the magnitude and direction of the droplets which impinged upon the turbine blades. For this, it is necessary to know the nozzle and blade geometry as well as the turbine wheel rotational speed and the thermodynamic properties of the potassium vapor at the nozzle inlet. The terminology used in the following discussion corresponds to that previously presented in Figure 7-2.

As mentioned, the test turbine had eight sets of blades having four different blade angles β_1; 25, 30, 35, and 40 degrees; the nozzle geometry is shown in Figure 7-20. The polytropic exponent for potassium vapor was taken to be 1.40, Reference 27, and the average conditions prevailing during the test were:

Nozzle inlet stagnation pressure = 5.6 psia

Nozzle inlet stagnation temperature = 1250°F

The following equations, which are taken from Traupel (Reference 28), allow an estimate to be made of the deflection of the nozzle flow and the change in magnitude of the spouting velocity due to the premature separation of the flow from the nozzle under off-design expansion conditions. The geometry to which these equations apply is defined in Figure 7-21. The Mach number of the deflected flow is given by

$$M_1 = \left\{ \left(\frac{1}{M_1'} \right)^2 - \frac{n-1}{2} \left[1 - \left(\frac{M_a}{M_1'} \right)^2 \right] \right\}^{-1/2} \qquad 7.35$$

and the angle through which the flow turns by

$$\sin \alpha_1 = \left(\frac{p_a}{p_1} \right) \left(\frac{M_a}{M_1'} \right) \left[1 - \frac{n-1}{2} \left(M_1'^2 - M_a^2 \right) \right] \sin \alpha_a \qquad 7.36$$

where the parameter M_1' is defined by

$$M_1' = (1 - \zeta)^{1/2} \left\{ M_a^2 + \frac{2}{n-1} \left[1 - \left(\frac{p_1}{p_a} \right)^{\frac{n-1}{n}} \right] \right\}^{1/2} \qquad 7.37$$

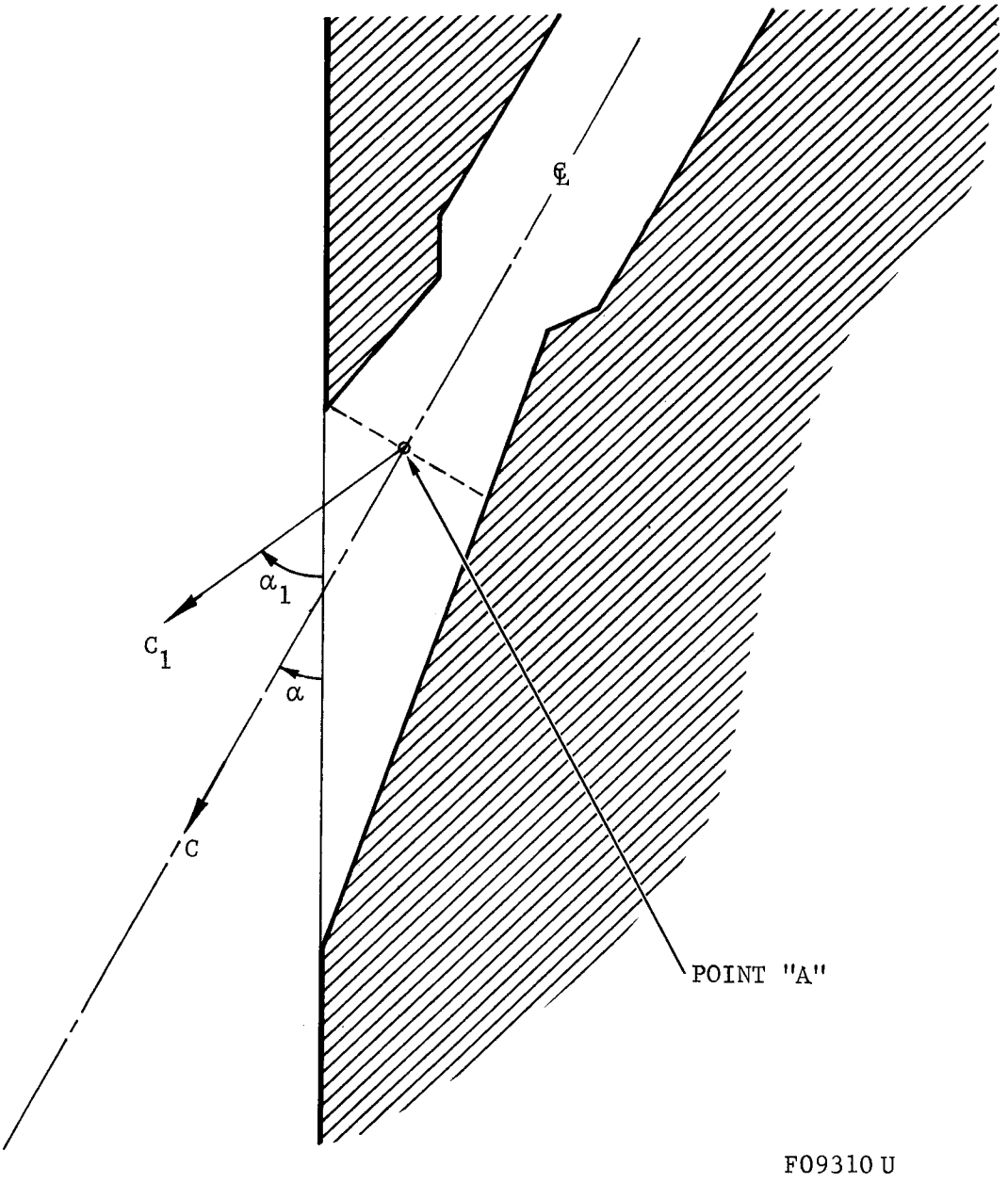

FIGURE 7-21. NOZZLE TERMINOLOGY

and ζ is a loss coefficient characterizing the irreversibility of the flow deflection.

Table VIII summarizes the characteristics of the deflected flow when point "a" is taken to be in the cross section of the nozzle lip. Using the appropriate Mach number shown, it is interesting to note that a Mach line from point "a" intersects the nozzle wall at approximately the position of the start of the material deposit and erosion.

TableVIII. Deflected Flow Characteristics

	Point "a"	Point 1 (exit)	
ζ, loss coefficient	0	0.01	0.10
p, pressure (psia)	1.08	0.81	0.81
M, Mach number	1.75	1.92	1.77
α, absolute flow angle (degrees)	21	25	28

Assuming the expanding vapor is a perfect gas, the speed of sound can be estimated by the following equation

$$a = \sqrt{n\,R\,T} \tag{7.38}$$

where

a = speed of sound, ft/sec

R = gas constant, ft/°R

T = static temperature of vapor, °R

n = polytropic exponent

Using the temperature obtained from the downstream stagnation conditions as measured in the test program, Equation (7.38) gives a speed of sound at the nozzle exit of 1130 ft/sec.

Table IX summarizes the velocity triangle parameters based on the exit Mach numbers of 1.92 and 1.77 for Traupel loss coefficients of ζ = 0.01 and 0.10, respectively. In accordance with the test results of Reference 3, the droplets formed in expansion through the nozzle are less than 1 micron in diameter and have essentially zero slip velocity.

Table IX. Gas Velocity of Small Droplet (< 1 μ) Velocity Triangle Parameters

ζ, loss coefficient	0.01	0.1
C, spouting velocity, ft/sec	2170	2000
u/C, tip speed ratio	0.169	0.183
W, relative velocity, ft/sec	1848	1688
α_1, absolute flow angle, degrees	25	28
β_2, relative flow angle, degrees	29.7	34.0
v_a, axial velocity, ft/sec	918	939

The slip velocity of the large liquid drops (100 μ approximately) is calculated in Paragraph7.5.2. as 1200 ft/sec. This slip velocity is subtracted from the Traupel spouting velocity to calculate the droplet velocities and, consequently, the velocity triangle of the large liquid drops. The results are summarized in Table X .

Table X . Large Droplet (100 μ) Velocity Triangle Parameters

ζ, loss coefficient	0.01	0.1
U_d, droplet absolute velocity, ft/sec	970	800
u/U_d, tip speed ratio	0.376	0.457
W_d, relative velocity, ft/sec	913	762
α_1, absolute flow angle, degrees	25	28
β_2, relative flow angle, degrees	40.0	51.0
v_a, axial velocity, ft/sec	410	375

Examination of the tables above shows that the large liquid droplets could feasibly impinge directly on the back side or convex side of the blades. The large liquid droplets have a relative blade flow angle of 40.0 to 51.0 degrees while the blade angles range from 25 to 40 degrees. If these drops do impinge on the convex side of the blade, then some of the observed erosion in this region can be due to this phenomenon.

The flow pattern on the blades is shown on Figure 7-22. Two prominent features are depicted on this diagram. The first is the appearance of a detached shock in front of the blade. The second and most important is the separated flow region which begins at the convex surface of the blade immediately after the flat portion of the blade. In this region, low flow velocities exist in a direction tangential to the blade. It is possible that the low pressure existing in this region may have resulted in some cavitation type damage. The groove on the convex surface of the blade falls within this region. It would be logical to say that the liquid potassium which is supposed running in the groove travels radially on the blade due to centrifugal forces and cannot proceed in a tangential direction because of low aerodynamic forces acting on the liquid layer.

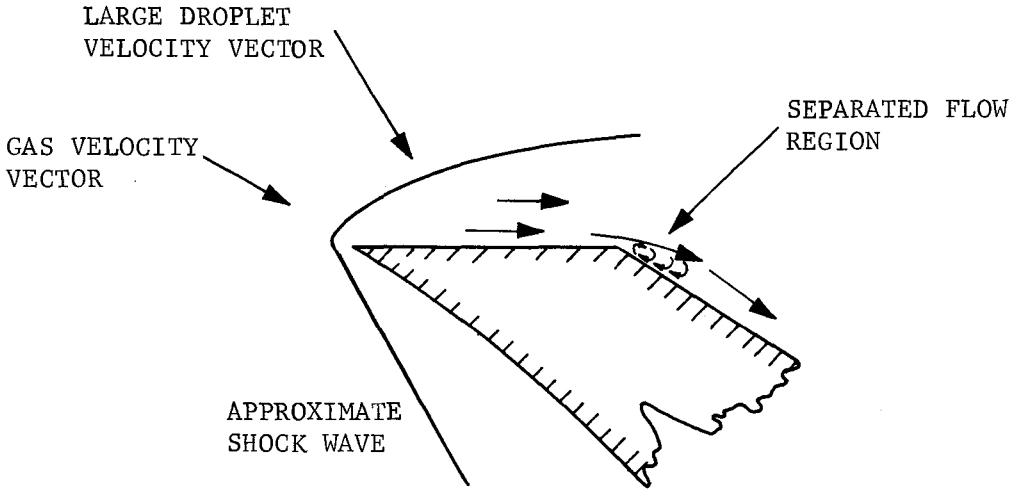

F09311 U

FIGURE 7-22. FLOW PATTERN ON LEADING EDGES OF BLADES

7.6 WET VAPOR POTASSIUM TURBINE PERFORMANCE TRENDS

The designer of conventional multistage, subsonic, potassium vapor turbines is constantly worried about knowing exactly the limiting turbine tip speed beyond which blade damage occurs in the low-pressure stages because of the impact of large droplets (shed from the stator vanes) on the leading edges of the turbine buckets. For these large droplets, the impact velocity is essentially the turbine tip speed, that is to say the droplets have nearly negligible velocity and cannot be accelerated or dispersed by the subsonic free gas stream. However, in case a single-stage, supersonic turbine is considered, the stream velocity is very large and agglomeration of large droplets may be eliminated. As a matter of act, the results have shown conclusively that the droplets leaving the tested supersonic nozzles are in the micron range and, therefore, move essentially with the free stream with negligible slip velocity. In this case, it is expected that turbine blade erosion cannot occur and the tip speed is not limited by two phase flow conditions, but rather by material strength and stress considerations. In other words, in a truly supersonic wet vapor turbine, operating even at qualities as low as 80 percent, there does not exist a vapor quality type of limiting tip speed barrier which allows high speed turbine operation with increased efficiency and high degree of reliability.

However, it is unfortunate that results of the potassium turbine experiment did not substantiate erosion-free supersonic turbine operation because of a separation and liquid corrosion problem experienced in one of the three turbine nozzles.

It is strongly recommended to redesign the turbine nozzles and to rerun the turbine experiment in a very accurately controlled, extremely oxygen-free potassium environment to prove erosion-free, supersonic, single-stage, axial turbine operation. However, even in absence of this postulated experiment, there is enough experimental and analytical evidence accumulated during the present program to point toward a very promising avenue of compact, highly efficient, erosion-free, supersonic turbine development.

In case multistage supersonic turbines are considered, there is less comfort in predicting the erosion trend of the second stage. In particular, one can only consider the technical arguments brought forward in the present report which lack experimental evidence derived from an actual multistage supersonic turbine. Nevertheless, the picture is not completely dark because experiment and analysis strongly support the argument that large droplets entering the second-stage supersonic nozzle block will be accelerated and torn to small droplets because of the highly supersonic free stream flow. For example, the Weber number/Reynolds number criterion shows that the stable droplet size diameter decreases inversely proportional to the third power of the free stream velocity. In view of these facts, it is certainly worthwhile to continue single and multistage supersonic alkali wet vapor turbine experiments, which seem to promise a reasonable and compact solution for the present alkali metal turbine development problem.

SECTION 8

SUMMARY AND RECOMMENDATIONS

The program results may be summarized as following:

1. All program objectives have been met.

2. A practical closed loop potassium test facility was developed, which provided a trouble free test bed for the critical droplet size measurements and the potassium turbine erosion experiment.

3. The unique supersonic nozzle-wedge erosion method of droplet size measurement worked and should be utilized for future more detailed two-phase flow investigations.

4. Consistent and reproducible droplet size measurements have been obtained for the specified temperature and quality range.

5. The droplet size is found to depend strongly on quality, while temperature and pressure influences appeared to be negligible for the given test runs.

6. The measured droplet sizes are larger than 0.1 micron and less than 0.70 micron.

7. The potassium test turbine, supported by tungsten carbide, hydrodynamic type of bearings with hydrostatic loading, was operated successfully with the closed potassium loop facility for a period of 96 hours.

8. Inspection of the test turbine indicated significant corrosion of one of the three turbine nozzles and unexpected surface erosion patterns on the rotor blades.

9. Analysis of the test results and fundamental consideration of the supersonic wet vapor fluid dynamics involved indicated that the particular turbine erosion patterns occurring during this program do not present a fundamental problem, since proper design of the nozzles and more stringent control of the oxygen level will certainly eliminate the turbine erosion peculiar with the particular test hardware.

Based on the novel analytical treatment of supersonic wet vapor fluid dynamics, including detailed consideration of the gas dynamic, relaxation, and equilibration zones, as well as the analytical exploration of fluid collection on blades and droplet shedding from liquid layers formed on stator blades, the following conclusions can be presented.

1. The single-stage, supersonic, wet vapor, alkali metal turbine has an excellent potential to operate erosion free without a wet vapor quality type of turbine tip-speed limitation.

2. Fundamental understanding of the wet vapor shock interaction and structure may be utilized for the control of liquid droplet sizes within the turbine rotor.

3. Erosion-free, single-stage, supersonic potassium turbine operation appears to be possible provided the nozzles are designed for elimination of any separation and, therefore, accumulation zones for liquid.

4. For the purpose of designing two-stage, erosion-free supersonic potassium turbines, the present analysis of fluid collection on blades and droplet shedding from liquid layers formed on stationary blade surfaces needs further experimental substantiation.

In view of all the facts presented, the following are recommended:

1. Rerun the Task II turbine experiment with correctly designed wet vapor supersonic nozzles for the purpose of demonstrating erosion-free turbine operation without a vapor quality type of tip-speed limitation.

2. Substantiate the wet vapor shock interaction processes by appropriate fundamental experiments.

3. Utilize the analysis of fluid collection on rotating blades and droplet shedding from stationary blade as a starting point for the investigation of a two-stage, supersonic, wet potassium vapor turbine.

4. Apply and verify the results of the present program when using other alkali metals of interest.

SYMBOLS
Not defined in text

a	Speed of sound in vapor or gas
A	Local cross sectional area of nozzle
c_p	Specific heat at constant pressure
c_v	Specific heat at constant volume
c_ℓ	Specific heat of liquid
C_d	Drag coefficient
C_f	Fluid shear coefficient
h	Thermodynamic enthalpy
h_ℓ	Latent heat of vaporization
m	Mass of single liquid droplet
M	Mach number
p, P	Local pressure of vapor or gas
R	Gas constant, also radius of curvature
R_t	Tip radius of turbine
t	Time
T	Temperature, absolute
u	Velocity component parallel to x axis, or in radial direction
v	Velocity component parallel to y axis, or in tangential direction
V	Gas or vapor velocity, general
u^*	Critical velocity of droplet or particle required to damage surface.
x, y	Cartesian coordinates

α	Wedge semi vertex angle
$\alpha_1(\mathrm{Re})$	Functions of Reynolds number occurring in particle drag and
$\alpha_2(\mathrm{Re})$	heat transfer.
γ	Ratio of specific heats, c_p/c_v
δ	Thickness of liquid layer on blades
η	Ratio of liquid mass to vapor mass per unit volume
σ	Local droplet radius
Σ	Ratio of surface area of liquid droplet to its original or reference area.
μ	Viscosity coefficient
ν	Kinematic viscosity of vapor
ρ	Density, mass per unit volume
θ	Turning angle of vapor passing through blades
ω	Angular velocity of turbine wheel
λ_v	Velocity equilibration length
λ_T	Temperature equilibration length

Subscripts

0,1,2,3	Reference locations along flow path
p	particle
ℓ	liquid
v	vapor

REFERENCES

1. Gyarmathy, G., Grundlagen einer Theorie der Nassdampfturbine, 1960 Juris-Verlag, Zuerich.

2. "Basic Investigation of Turbine Erosion," Contract NAS 7-390, Westinghouse Electric Corporation, 1966.

3. Degner, V., Investigation of Variables in Turbine Erosion, monthly progress reports, Contract NAS 7-391, North American Aviation, Rocketdyne Division, 1966.

4. Schnetzer, E., Two Stage Potassium Test Turbine, progress reports, Contract NAS 5-1143, General Electric Co., 1965.

5. Carrier, G. F., "Shock Waves in a Dusty Gas," J. Fluid Mech. 4, 376-382 (19

6. Marble, Frank E., "Dynamics of a Gas Containing Small Solid Particles," Proceedings 5th AGARD Colloquium on Combustion and Propulsion (Braunschweig), Pergamon Press (1963), pp. 175-213.

7. Rudinger, G., "Some Properties of Shock Relaxation in a Gas Carrying Small Particles," Physics of Fluids, Vol. 5, No. 7 (1964), pp. 658-663.

8. Panton, R. L., "Study of Non-Equilibrium Two-Phase Flow of a Gas Particle Mixture," Thesis, College of Engineering, University of California, Berkeley (1966).

9. Oswatitsch, K., "Kondensationerscheinungen in Uberschalldusen," Zeit. F. Angew. Math. u. Mech., Vol. 22, No. 1 (February 1942), pp. 1-14.

10. Wegener, P., Reed, S., Jr., Stollenwerk, E., and Lundquist, G., "Air Condensation in Hypersonic Flow," Journal of Applied Physics, Vol. 22, No. 8 (August 1951), pp. 1077-1083).

11. Weatherford, W. D., Jr., Tyler, J. C., and Ku, P. M., "Properties of Inorganic Energy-Conversion and Heat-Transfer Fluids for Space Application," WADD Technical Report 61-92, U. S. Air Force, Wright-Patterson Air Force Base (1961).

12. Rannie, W. D., "A Perturbation Analysis of One-Dimensional Heterogeneous Flow in Rocket Nozzles," Progress in Astronautics and Rocketry, Vol. 6 (1962), Academic Press, New York.

13. Goldman, L. J., and Nosek, S. M., Experimental Nozzle Expansion and Flow Characteristics of Potassium Vapor, NASA TN D-3209, Lewis Research Center, Cleveland, January 1966.

14. Schnetzer, E., Two Stage Potassium Test Turbine, QPR No. 10, November 8, 1963 for NASA Contract NAS 5-1143, Missile and Space Div., General Electric Co.

15. Ames Research Staff, Equations, Tables, and Charts for Compressible Flow, NACA Report 1135, 1953.

16. Gyarmathy, G., and Meyer, H., Spontane Kondensation, VDI-Forschungsheft 508, 1965.

17. Schnetzer, E., Two Stage Potassium Test Turbine, QPR No. 13, August 8, 1964 for NASA Contract NAS 5-1143, Missile and Space Div., General Electric Co.

18. Engel, O. G., "Pits in Metals Caused by Collision with Liquid Drops and Soft Metal Spheres," Journ. of Res. N.B.S., Vol. 62, No. 6, June 1959, Res. Paper 2958.

19. Engel, O. G., "Pits in Metals Caused by Collision with Liquid Drops and Rigid Steel Spheres," Journ. of Res. N.B.S., Vol. 64A, No. 1, Jan-Feb, 1960.

20. Whiffin, A. C., "The Use of Flat-Ended Projectiles for Determining Dynamic Yield Stress," Proc. of the Royal Society, 1948, pp 300-331.

21. Schlichting, H., "Grenzschicht-Theorie," Verlag G. Braun, Karlsruhe, 1954.

22. Gardner, G. C., "Events Leading to Erosion in the Steam Turbine," Proc. Ins. Mech. Engr., Vol. 178, Pt 1, No. 23, 1963-64.

23. Glassman, A. J., Analytical Study of the Expansion and Condensation Behavior of Alkali-Metal and Mercury Vapors Flowing Through Nozzles, Lewis Research Center NASA Tech. Note E-2482, 1966.

24. Marble, F. E., Particle Growth in Rocket Nozzles Resulting from Droplet Slip and Collision, Astronautica ACTA, 1967.

25. Stang, J. H., Simons, E. M., DeMastry, J. A., Genco, J. M., "Compatibility of Liquid and Vapor Alkali Metals with Construction Materials," Defense Metals Information Center, Batelle Memorial Institute, DMIC Report 227, April 15, 1966.

26. Hinze, J. O., "Critical Speeds and Sizes of Liquid Globules," App. Sci. Res., pp 273-288, 1949.

27. Schnetzer, E., "Two Stage Potassium Test Turbine," Quarterly Progress Report No. 10, Missile and Space Division, General Electric Co., Cincinnatti, Ohio, November 8, 1963.

28. Traupel, Walter, "Thermische Turbomaschinen," Springer-Verlag, Berlin, 1958, pp. 220-226.